



# **Neutral Atom Interactions at Surfaces, in Mixtures, and Bose-Condensates**

Forschungsarbeit in Physik

angefertigt im  
Institut für Angewandte Physik

vorgelegt der  
Mathematisch-Naturwissenschaftlichen Fakultät  
der  
Rheinischen Friedrich-Wilhelms-Universität Bonn

von  
Vanessa Leung

Bonn  
im Juli 2006

Angefertigt mit Genehmigung  
der Mathematisch-Naturwissenschaftlichen Fakultät  
der Rheinischen Friedrich-Wilhelms-Universität Bonn

1. Gutachter: Prof. Dr. Dieter Meschede
2. Gutachter: Dr. Ken Baldwin

Tag der Promotion: 08. Juli 2006



## Abstract

This thesis presents, through a series of experimental and numerical results, an investigation of the collisional interactions of neutral atoms for topics of technological and scientific interest, namely, atom-surface interactions for lithography, and atom-atom interactions in cold atomic mixtures and Bose-Einstein condensates.

In the first chapter I report on an experimental scheme to investigate the interaction of metastable helium atoms with molecular surface monolayers, which act as ultrathin resists for atom lithography. We seek to isolate the interaction between the metastable atom and the monolayer from other possible interactions, such as that of ultraviolet photons, which are also present in significant quantities. Using the characterized properties of a new liquid nitrogen-cooled discharge source, an experimental scheme was implemented which utilizes magnetic manipulation techniques for neutral atoms to create a lithography exposure involving metastable helium atoms alone.

In the second chapter, the development of an experiment for the study of ultracold interactions between rubidium and cesium atoms is documented. Starting with an experiment for the Bose-Einstein condensation of Rb-87, modifications were made which allowed the simultaneous confinement of rubidium and cesium atoms in magneto-optical, quadrupole, and Ioffe trapping configurations. By imprinting a temperature gradient between the overlapped atomic clouds through optical molasses, re-thermalization between magnetically trapped rubidium and cesium atoms through  $s$ - and  $p$ -wave collisions was observed. In order to create precise and variable temperature gradients in the binary mixture, a modular 6.83 GHz source was implemented for species-selective evaporative cooling at the hyperfine transition frequency of rubidium. Bose-Einstein condensates of rubidium was created and the lifetime-limiting losses due to three-body collisions investigated.

The third chapter puts forward the results of numerical simulations on the creation and propagation of bright soliton trains in Bose-condensates, based on the experimental observation of soliton trains by Strecker *et al.* [1]. Using a mean-field approach, numerical solutions of the Gross-Pitaevski equation were obtained which reproduce the key features of the experiment and offer insights into soliton collisions and the determination of soliton number.

## Zusammenfassung

Diese Arbeit präsentiert eine Untersuchung von Kollisionswechselwirkungen zwischen neutralen Atomen. Es werden experimentelle und numerische Ergebnisse vorgestellt, die für technologische und wissenschaftliche Ziele interessant sind: Atom-Oberflächen-Wechselwirkungen für Lithografie und

## II

Atom-Atom-Wechselwirkungen in kalten atomaren Mischungen und Bose-Einstein-Kondensaten.

Im ersten Kapitel berichte ich über ein Experiment, dass die Wechselwirkungen von metastabilen Heliumatomen mit oberflächenmonomolekularen Filmen untersucht, die als ultradünne Schutzschicht für Atomlithografie dienen. Wir versuchen die Wechselwirkung zwischen den metastabilen Atomen und dem monomolekularen Film von anderen möglichen Wechselwirkungen, wie die der ultravioletten Photonen, zu isolieren. Diese sind ebenfalls in bedeutenden Mengen anwesend. Mit den zuvor charakterisierten Eigenschaften einer neuen flüssigstickstoffgekühlten Entladungsquelle, wurden Experimente durchgeführt, die die magnetischen Manipulationstechniken neutraler Atome nutzen. Das erlaubt die alleinige Belichtung mit metastabilen Heliumatomen.

Im zweiten Kapitel wird die Entwicklung eines Experimentes für die Studie von ultrakalten Wechselwirkungen zwischen Rubidium- und Cäsiumatomen dokumentiert. Ein Experiment zur Erzeugung von Rb-87 Bose-Einstein-Kondensaten wurde derart modifiziert, dass Rubidium- und Cäsiumatome simultan in der magnetooptischen Falle, der Quadrupolfalle und der Ioffefalle gespeichert werden können. Durch das Einbringen eines Temperaturgradienten mittels optischer Melasse zwischen den sich überlappenden Wolken, konnte eine Rethermalisierung zwischen den magnetisch gefangenen Atomen aufgrund von s- und p-Wellen-Streuung beobachtet werden. Um den Temperaturgradienten in der binären Mischung präzise variieren zu können, wurde eine modulare 6,83 GHz-Quelle zum speziesselktiven Verdampfungskühlen aufgebaut, die Übergänge zwischen den Hyperfeinenniveaus der Rubidiumatome treibt. Hiermit wurden Rubidium Bose-Einstein-Kondensate erzeugt und die Lebensdauer begrenzenden Verluste aufgrund von Drei-Körper-Stößen untersucht.

Das dritte Kapitel zeigt die Ergebnisse numerischer Simulationen von der Erzeugung und Ausbreitung heller Solitonzüge in Bose-Einstein-Kondensaten. Diese Simulationen basieren auf den experimentellen Beobachtungen von Strecker et al. [1]. Mit einer Mean-Field-Annäherung wurden numerische Lösungen der Gross-Pitaevski-Gleichung bestimmt, die die Hauptmerkmale des Experiments reproduzieren. Außerdem gestatten sie Einblicke in Solitonen-Kollisionen sowie die Bestimmung der Anzahl der Solitonen.

## Publications

Parts of this thesis have been/will be published in the following journal articles:

1. V.Y.F. Leung, A.G. Truscott, and K.G.H. Baldwin, *Nonlinear atom*

*optics with bright matter-wave soliton trains*, Physical Review A **66**, 061602 (2002).

2. R.R. Chaustowski, V.Y.F. Leung, and K.G.H. Baldwin, *Magnetic hexapole lens focussing of a metastable helium atomic beam for UV-free lithography*, submitted to Applied Physics B.



# Contents

<b>Introduction</b>	<b>1</b>
<b>1 Metastable helium: magnetic manipulation and resist-based lithography</b>	<b>5</b>
1.1 Metastable helium experiments at the ANU . . . . .	6
1.2 Resist-based atom lithography . . . . .	7
1.3 Metastable helium: ‘nature’s nano-grenades’ . . . . .	9
1.4 Self-Assembled Monolayers . . . . .	11
1.4.1 Lithography Exposures . . . . .	12
1.4.2 Motivation for further beam characterization . . . . .	14
1.5 He* source characterization . . . . .	16
1.5.1 He* source vacuum system . . . . .	16
1.5.2 The He* discharge source . . . . .	17
1.5.3 Electron emission detectors . . . . .	20
1.5.4 Beam profile and time-of-flight measurements . . . . .	20
1.5.5 Quenching Experiments . . . . .	25
1.6 Magnetic manipulation of He* . . . . .	26
1.6.1 Hexapole magnetic lens . . . . .	26
1.6.2 Particle Optics Approach . . . . .	29
1.6.3 First evidence of magnetic manipulation . . . . .	32
1.7 Conclusion . . . . .	33
<b>2 Binary bosonic mixtures: re-thermalization and species-selective evaporative cooling</b>	<b>37</b>
2.1 Cold atom experiments at the University of Bonn . . . . .	38
2.2 Simultaneous magneto-optical trapping of Rb and Cs . . . . .	39
2.3 Production of ultracold rubidium . . . . .	40
2.3.1 Main vacuum system . . . . .	41
2.3.2 Laser system for Rb . . . . .	42
2.3.3 Absorption imaging system . . . . .	44
2.4 New additions for cooling and trapping cesium . . . . .	46
2.4.1 Laser system for Cs . . . . .	46
2.4.2 Specialized optics and optical layout . . . . .	48

2.5	Loading a mixed species MOT . . . . .	48
2.6	Interspecies re-thermalization in a conservative potential . . .	51
2.6.1	Magnetic traps for rubidium and cesium atoms . . . . .	52
2.6.2	Loading of atomic mixture into a magnetic trap . . . . .	53
2.6.3	Magnetic trap deformation . . . . .	54
2.6.4	Thermal contact in a magnetic trap . . . . .	55
2.6.5	Experimental realization of re-thermalization . . . . .	57
2.7	Species-selective temperature control . . . . .	60
2.7.1	RF evaporative cooling . . . . .	62
2.7.2	Hyperfine evaporation at microwave frequencies . . . . .	63
2.7.3	Implementation of a modular microwave source . . . . .	64
2.8	Quantum degeneracy and three-body collisions . . . . .	67
2.8.1	Bose-Einstein Condensation . . . . .	67
2.8.2	Trap loss through three-body recombination . . . . .	71
2.8.3	Perspectives for future experiments . . . . .	77
2.9	Conclusion . . . . .	78
<b>3</b>	<b>Bright soliton trains: creation and propagation</b>	<b>81</b>
3.1	Non-linear effects in Bose-Einstein condensates . . . . .	81
3.1.1	The mean-field description of condensate behavior . . .	81
3.2	Non-linear atom optics with bright matter wave soliton trains	84
3.2.1	Abstract . . . . .	84
3.2.2	Introduction . . . . .	84
3.2.3	Simulating a quasi-1D condensate . . . . .	85
3.2.4	Numerical results and analysis . . . . .	87
3.2.5	Conclusion . . . . .	91
3.2.6	Acknowledgments . . . . .	91
3.3	Factors determining soliton number . . . . .	91
<b>4</b>	<b>Conclusion and Outlook</b>	<b>95</b>
4.1	UV-free He* lithography . . . . .	95
4.1.1	Exposures with magnetically focussed atoms . . . . .	95
4.2	Ultracold collisional studies with Rb and Cs mixtures . . . . .	96
4.2.1	Determination of $a_{RbCs}$ and Feshbach resonances . . .	98
4.3	Matter-wave soliton trains . . . . .	99
<b>A</b>	<b>Atomic data</b>	<b>101</b>
<b>B</b>	<b>Cesium optical system</b>	<b>103</b>
<b>C</b>	<b>Further experiments with microwave-field dressed potentials</b>	<b>107</b>
	<b>Bibliography</b>	<b>109</b>

*CONTENTS*

VII

**Acknowledgements**

**119**



# Introduction

A large class of the possible interactions of a neutral atom with its environment is mediated by collisions. These collisions may take femtoseconds or hundreds of nanoseconds, be elastic or inelastic, occur in ultracold confinement or at room temperature. They may be visualized as the result of particles following classical mechanical trajectories, or can only be understood as a manifestation of the statistics and dynamics of quantum objects.

Out of the countless situations where the collisional behavior of a neutral atom leads to observed physical effects, this thesis will consider the following scenarios. One is presented because it is technologically intriguing, the others because they are of current scientific interest.

Through experiments with a class of atoms which contain high internal energy, the modification of molecular surfaces by neutral atom impact has been demonstrated for the transfer of spatial patterns on the micrometer scale. To bring about large-scale structural change to the target molecule, intermolecular binding energies must be overcome, requiring collision energies on the order of tens of electron volts. Furthermore, as the atoms are travelling at velocities of  $\sim 1000$  m/s, their de Broglie wavelength is much smaller than the wavelength of light, a necessity for the definition of precise edges in micro-structures.

In the first chapter I describe our development of an experiment to isolate and study in controlled conditions the interaction of these fast, energetic particles with a molecular monolayer. This is accomplished through magnetic focussing, the effects of which can be described with a classical ray optics approach due to the overwhelmingly particle-like nature of the atoms. To this end, I have characterized a new liquid-nitrogen discharge source of metastable helium for atom lithography, which allowed me to evaluate the feasibility of using magnetic manipulation for metastable helium atoms at high longitudinal velocities, and performed experiments on the magnetic focussing of metastable helium, the application of which is a key point of the UV-free lithography scheme.

The interactions described in Chapter 1 are some of the most energetic in neutral atom optics. At the other end of the continuum, there has been much recent interest in collisions which happen at much lower energies and slower time scales. The physical simplification brought by lowering the interaction

energy can be appreciated by considering that at energies near the ground-state collision energy, scattering processes can be decomposed into partial waves characterized by the angular symmetry of the collision. Furthermore, at temperatures of several micro-Kelvin, interactions between alkali neutral atoms are dominated by the spherically symmetric  $s$ -wave, the cross-section of which is almost completely describable by the two-body scattering length, a parameter on the order of a few nanometers.

Chapter 2 begins with the study of collisional interactions between atoms of different species, within a cold atomic mixture prepared using the experimental tools first developed for Bose-Einstein condensation. Early studies of cold mixtures were often mediated by resonant light due to the trapping of atoms in hybrid traps of laser and magnetic fields, which facilitated excited state processes and often lead to complex theoretical descriptions. The situation can be simplified by transferring atoms of both species into a dark conservative potential. Here elastic collisions can occur between particles and drive both clouds into thermal equilibrium. In Chapter 2 I describe our implementation of a two-species MOT system for the collection of atoms of Rb and Cs, and the simultaneous transfer of the two species into a magnetic trap, as well as the first observation of re-thermalization, which I analyze and present in detail.

Continued reduction of temperature at a given density eventually leads to the formation of a Bose-Einstein condensate, in which the wave-functions of individual particles share the same space and the atomic ensemble is dominated by the quantum statistical properties of bosons. To allow one species of a mixture to be cooled down into the ultracold or quantum degenerate regime in the presence of the other without the removal of atoms from both species, species-selective evaporative cooling must be implemented. To do this, I have assembled and tested a modular microwave system for our future experiments in sympathetic cooling and interspecies re-thermalization. Using this system, we have begun an investigation into three-body collisions in our experimental system, starting in the first instance with a single-species cloud of atomic Rb. In Chapter 2 I present a detailed analysis of this measurement and examine the possible effects of three-body loss processes for our Rb-Cs mixture.

In probing the effect of atom-atom interactions in Bose-condensates it is often advantageous to regard interactions not as solely occurring via scattering processes between individual particles but as a collective phenomenon described by a mean-field. In Chapter 3 I present numerical solutions to such a mean-field description of a BEC. Regardless of the change in perspective, however, the interaction of particles in this description remains parameterized by the scattering length, which mediates changes in the shape and size of the condensate, as well as non-linear effects such as the formation of self-stabilizing wavepackets, or solitons. Working close to the original experiment conditions which lead to the observation of multiple solitons, I

carried out numerical simulations which reproduce their creation and propagation in Bose-Einstein condensates, and investigated the effects of soliton collisions and the determination of soliton number.

The thesis is divided roughly equally between work performed at the Atom Manipulation group in the Australian National University (ANU), and the BEC group in the University of Bonn. The research areas reported in each chapter therefore reflect the different experimental directions of these groups, and some historical perspective on the evolution of the present joint dissertation might be appropriate at this point:

- As a doctoral candidate in Canberra, I began working with the manipulation of neutral atoms in the applied atom-optics field of atom lithography (Chapter 1). At that time, opportunities were not yet available to work on BEC experiments in our group.
- BEC experiments of a numerical nature, however, are much more readily procurable, and while in Canberra I reproduced numerically recent experimental observations of non-linear phenomena in Bose-Einstein condensates (Chapter 3).
- Shortly afterwards, I began a three-month research visit to the University of Bonn, where I had the opportunity to be involved experimentally in Bose-Einstein condensation. Since joining the BEC team in Bonn, the experiment has moved past Bose-condensation into cold atomic mixtures (Chapter 2).



## Chapter 1

# Metastable helium: magnetic manipulation and resist-based lithography

A major achievement of atom optics is the development of tools for manipulating atomic motion. Based on light and magnetic forces, these techniques allow the position and velocity of neutral atoms to be influenced with a greater degree of control than ever before.

Exploiting these techniques for pattern-making on the nanometer scale is the goal of atomic nanofabrication (ANF), a broad term that includes both direct atomic deposition, and lithographic techniques.

Patterned structures produced through ANF possess a resolution more than a factor of four superior to what is currently attained by optical lithography for silicon-based integrated-circuits [3]. The commercial value of such a factor of miniaturization can be gauged by considering Moore's Law, which states that the number of transistors on a semiconductor chip will double approximately once every two years.

One can argue that it does not harm a scientific endeavor to find its goals congruent with one of the most widely validated economic projections of our time. And although the possibility for mass production on a commercial scale with ANF has been significantly handicapped by the current speed limitations of the process, it remains one of the best developed applications of atom optics.

Today, thirteen years after the first atom deposition experiments by Timp *et al.*[2], atomic nanofabrication has developed sufficiently unique solutions to its many technical challenges for the field to be considered an experimental art in itself [3].

## 1.1 Metastable helium experiments at the ANU

The experiments described here were performed with metastable helium atoms ( $\text{He}^*$ ) - helium atoms which have been excited into a high energy state from which all optical decay channels to the ground state are forbidden. Metastable helium has several rather unique properties, and the exploitation of these properties for specific experimental purposes is a major theme of the present work.

The number of atom optics groups in the world which uses metastable helium is small – at the last count, approximately nine [4]. In two of these groups [5, 6], the Ecole Normale Supérieure (Paris) and the Institut d’Optique (Orsay), the pursuit and subsequent attainment of Bose-Einstein condensation of  $\text{He}^*$  is a noteworthy experimental achievement which pushed back the boundaries of ultracold manipulation techniques for this species. Recently, a  $\text{He}^*$  BEC has also been achieved in two additional laboratories [7, 8].

At the Australian National University (ANU), the Atom Manipulation Project is solely dedicated to experiments with metastable helium. Experiments range from guiding  $\text{He}^*$  atoms with hollow optical fibers [9], the determination of the total electron- $\text{He}^*$  scattering cross-section [10], to resist-based lithography [17] and Bose-condensation [8].

There are currently three experimental facilities in the laboratory, which range in sophistication from employing elaborate laser cooling and collimating systems [4], to no beam preparation at all. They thus differ strikingly in the degree of control available over the velocity distribution of the atomic beam. For the period of experimental work that I describe here, the apparatus immediately available for atom lithography is based around a thermal atomic source, with no subsequent laser cooling.

I have limited what I present in this chapter to an account of what was achieved in the eighteen months that I was solely responsible for developing the experiment i.e. (1) the characterisation of a new discharge source of metastable helium, (2) the development of the magnetic hexapole lens experiment for atom lithographic exposures with reduced ultraviolet (UV) photon flux, and (3) observation of the first evidence of magnetic manipulation. Naturally, previous and later work on the ANU atom lithography project exists, and detailed descriptions can be found in Refs. [15, 16, 40]. The rationale of treating this work as a self-contained unit arises simply from the relatively large time gaps, on the order of 1-2 years, which existed between those experiments and what is presented here.

## 1.2 Resist-based atom lithography

The use of atoms to produce planar and even holographic [11] images is that, in principle at least, the transfer of such patterns and images can be accomplished with nanometer resolution, far below the diffraction limit of visible and ultraviolet light.

This becomes apparent when one considers the de Broglie wavelength  $\lambda_{dB}$  of an atom due to the motion of its center of mass:

$$\lambda_{dB} = h/p \tag{1.1}$$

where  $p = mV$  is the momentum of the atom,  $m$  its mass,  $V$  its velocity, and  $h$  is Planck's constant. At room temperature, the de Broglie wavelength of a helium atom is  $\sim 0.05$  nm. For comparison, the wavelength of an UV-photon is on the order of 100 nm.

These comparisons certainly support the argument in favor of atom lithography as a technology for the fabrication of lateral structures in the micro- and nanometer regime. However, true realization of the physical advantage of using atoms requires that this advantage be preserved throughout the steps of the experimental protocol, without loss of resolution.

One such experimental protocol is resist-based lithography, a technique widely used in optical lithography. Its core steps, illustrated in Figure 1.1, are typical of all photoresist-based lithography – a sensitive surface is first prepared, then exposed, and finally developed to produce a permanent image:

(1) A substrate material, typically a gold-coated silicon wafer, is covered with a molecular layer or resist.

(2) During exposure a patterned mask above the substrate shields some areas and leaves others exposed to the atomic beam. The resist becomes structurally damaged in the exposed regions, and unable to protect the surface from hydrophilic solvents.

(3) Chemical reagents selectively attack the regions of damage and etch them into the substrate. The masked regions are left untouched, thus producing a permanent surface pattern.

From an atomic physics viewpoint, the exposure stage of the lithographic process offers a certain freedom to explore the use of different atomic species, with their wide variety of experimental characteristics due to variations in mass, internal structure, and magnetic moment. Out of this diversity, metastable rare gas atoms in general and metastable helium in particular has become one of the model systems due to recognition of their suitability for interacting with the molecular resist.

We seek to refine our investigation of the interaction between  $\text{He}^*$  atoms and the layer of molecules that comprises the resist, by developing a system which allows  $\text{He}^*$  atom lithography to be performed in a purer environment

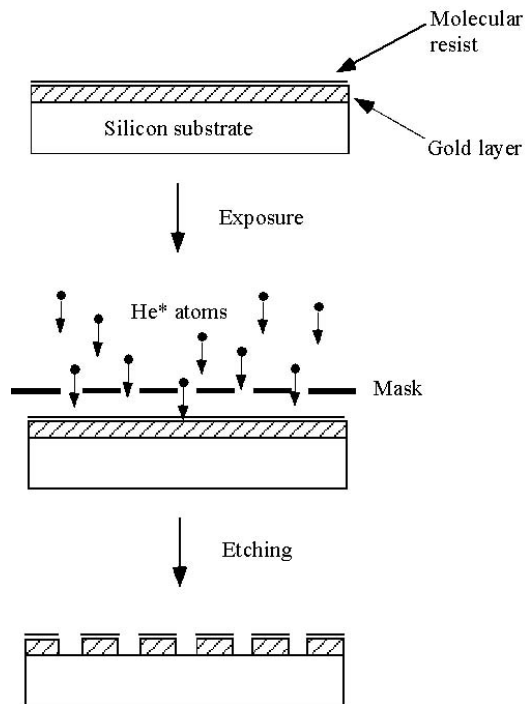


**Figure 1.1:** The core steps of resist-based atom lithography – sample preparation, exposure, and etching.

than has been available so far. To create this environment, we propose to make use of, among other attributes, the small mass and large magnetic moment of  $\text{He}^*$  compared to alkali atoms which allow even thermal  $\text{He}^*$  beams to be magnetically manipulated over feasible distances. To motivate the experimental proposal, in the next section the atomic properties of  $\text{He}^*$  will be introduced, and its conventional use in atom lithography demonstrated. Having established how atom lithography normally functions, we then move beyond the basic exposure process and concentrate on the isolation of the  $\text{He}^*$  component from other products of the atomic discharge. Through a scheme involving the use of magnetic manipulation we find that we can separate the effects of the highest energy particles, metastable helium and UV-photons, which usually are allowed to affect the exposure simultaneously. By thus significantly reducing the direct UV-flux, we hope to rule out the possible role of UV-light as a catalyst in the interaction between  $\text{He}^*$  and the molecular monolayer.

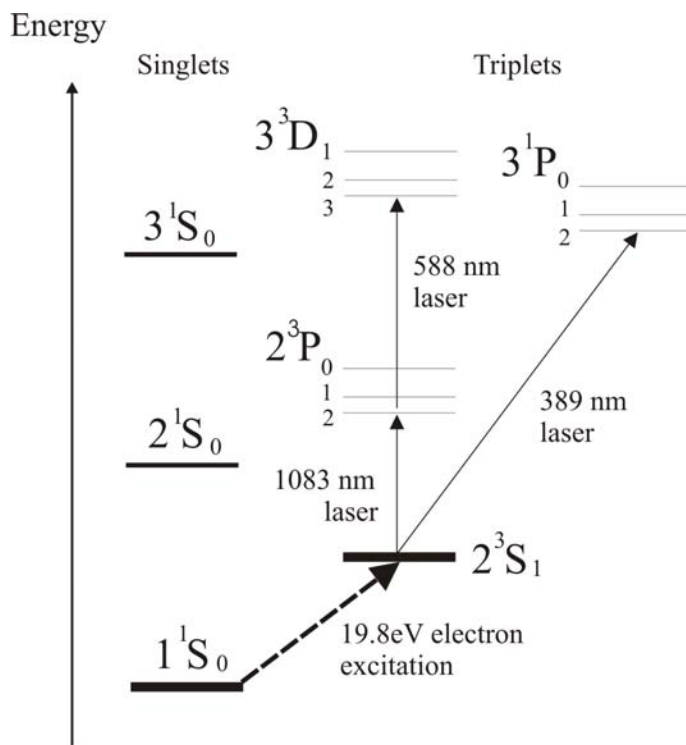


**Figure 1.2:** Helium energy level scheme, with principal laser transitions.

### 1.3 Metastable helium: ‘nature’s nano-grenades’

Metastable helium atoms have been nicknamed ‘nano-hand grenades’ [4] due to their ability to carry potential energy from place to place, and the ease with which they give up these large amounts of energy on contact with surfaces or other atoms.

Three major contributing factors play a role. First, the amount of energy in the  $2^3S_1$  metastable state, 19.82 eV, is the largest of any metastable atomic or molecular system. Second, the state is extremely long-lived, with a lifetime of  $>8000$  s, enabling the particle to travel far in its high-energy state; and third,  $\text{He}^*$  de-excites readily via collisional loss channels such as Penning and associative ionization into ground-state helium or helium ions, rapidly releasing all of its stored energy in the process.

In its ground-state, helium is an unreactive gas that has no known compounds found in nature. Consisting of a single electron pair in the  $S$  shell  $1^1S_0$ , the resulting closed-shell system is chemically inert, and, significant from an experimental point of view, ‘invisible’ to metastable helium detectors, which typically detect effects associated with a large release of energy (Sec. 1.5.3).

The first excited states of helium are the spin-opposed (singlet) and

spin-parallel (triplet)  $S$  states,  $2^1S_0$  and  $2^3S_1$  respectively (Fig. 1.2). As a result of angular momentum and spin selection rules, these are long-lived or metastable states.

In both the singlet and triplet  $S$  states, an electron is forbidden from decaying into the ground state via an optical transition due to the condition that  $\Delta L = \pm 1$ , where  $L$  is the orbital angular momentum quantum number, and  $L = 0$  for  $S$  states. As a result, the  $2^1S_0$  state has a lifetime of  $\sim 19$  ms, and its eventual decay is due mainly to two-photon processes [12].

In addition, the electron spins in the triplet state  $2^3S_1$  are furthermore forbidden from making the spin flip required to form the parallel-spin singlet  $1^1S_0$  ground-state. Thus *doubly* forbidden, the decay of  $2^3S_1$  is extremely rare, and the state has a predicted lifetime of  $\sim 8000$  s, decaying via a single-photon magnetic dipole transition [12, 13].

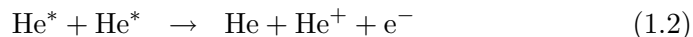
We use this metastable triplet state of helium in our experiments. Its lifetime is far longer than the duration of experimental measurements, and with an internal energy of 19.82 eV, it is detectable with close to unity efficiency, either with electron emission charged particle detectors, or via an atom lithographic resist.

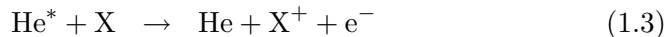
The nucleus of helium has zero spin, therefore its atomic spectra lack hyperfine structure. In an apparatus which utilizes laser cooling this is a valuable simplification - the lack of multiple ground-state hyperfine levels means that it is not necessary for  $\text{He}^*$  laser cooling systems to include a repumping laser. Two transitions are available for laser cooling - the  $2^3S_1 - 3^3P_{0,1,2}$  transition at 389 nm, and more commonly used, the  $2^3S_1 - 2^3P_{0,1,2}$  transition at 1083 nm. Atoms cooled with 1083 nm laser light are sometimes probed with a 588 nm laser at the  $2^3P - 3^3D$  transition, since fluorescence signals at 1083 nm, i.e. the far infra-red, are difficult to detect.

As the total spin of helium is purely electronic,  $J = 1$  for the spin-parallel  $2^3S_1$  state, which thus has a total magnetic moment  $\mu = 2\mu_B$ . This is twice that of the alkali atoms, for which  $\mu = \mu_B$ .

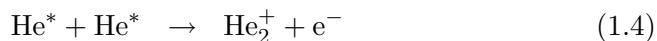
Of particular relevance to the motivation of the current experiment are the singlet transitions which emit photons in the extreme ultraviolet (XUV) regime. As the energies of these photons are in the range of 20-30 eV, they can damage a lithographic resist to a comparable degree as metastable atoms. The  $2^1P_1 - 1^1S_0$  transition at 58.4 nm, i.e. with an energy of  $\sim 21$  eV, is one of the strongest XUV-producing transitions, but  $nP - 1^1S_0$  and recombination transitions from the continuum ( $>25$ eV) also contribute to the XUV flux.

There are two major two-body collisional loss channels for  $\text{He}^*$ . *Penning ionization* can occur between two  $\text{He}^*$  atoms, or between a  $\text{He}^*$  atom and an atom of another gas species:





Alternatively, two  $\text{He}^*$  atoms may associate to form a molecular helium ion in a process known as *associative ionization*:



De-excitation of the metastable state through collisions is one of the particular experimental difficulties of working with this species. It is a limiting factor, for example, in the achievable density of a magneto-optical trap (MOT) [14], and therefore a  $\text{He}^*$  MOT has to be large and dilute, with densities of  $\sim 10^9 \text{ cm}^{-3}$ , compared to achievable densities of typically  $\sim 10^{10} \text{ cm}^{-3}$  for alkali atoms.

## 1.4 Self-Assembled Monolayers

For resist-based atom lithography to succeed, new technology was required to produce resists which could resolve and register impressions on the order of the de Broglie wavelength of neutral atoms. Furthermore, in addition to possessing high resolution, these resists must also be thin – it is estimated that metastable atoms are able to only interact with the molecular layer to a depth of  $\leq 0.5 \text{ nm}$  [29], limiting the possible thickness of a resist to no greater than  $\sim 3 \text{ nm}$ .

The solution was the engineering of molecules which spontaneously assemble on a surface, presenting a footprint on the order of nanometers in single layers no more than one molecular length deep. These so-called self-assembled monolayers (SAMs) consists of hydrocarbon chains which attach themselves by their reactive head groups to a surface. Dodecanethiolate (DDT), a twelve-carbon alkane capped by a sulfur head group, is often used.

The deposited SAM is 1-3 nm thick, with an average density of  $\sim 4.5 \times 10^{14} \text{ molecules/cm}^2$ . The packing of the molecules is close and highly ordered, akin to a 2D organic crystal on a surface. A resist-covered surface acquires a hydrophobic character which allows it to protect the substrate beneath from attack by water-based etchants. Resist molecules which have been damaged, however, loses this hydrophobicity. The degree of affinity for aqueous solution thus becomes the differentiating signature between damaged and undamaged regions of the monolayer.

As each molecule represents a target with a diameter of only  $\sim 0.3 \text{ nm}$ , the system is well-suited for achieving high overall resolution. In addition, measurements have shown that the monolayer is highly sensitive – it requires on average less than one metastable atom to damage a SAM molecule, due to secondary electron effects [30]. Therefore potential applications of SAMs are

not limited to use as an ultra-thin resist for atom lithography, but extends also to position-sensitive single atom detection, as suggested by Whitesides *et al.* [30].

### 1.4.1 Lithography Exposures

To demonstrate basic atom lithography we have performed exposures with alkanethiol-coated surfaces at a typical atomic flux density of approximately  $5 \times 10^{11}$  atoms/cm<sup>2</sup>/s. The experimental setup is described in detail in Section 1.5.2.

We employ as substrates silicon wafers coated with 3 nm of titanium as an adhesive agent, followed by a gold layer 30 nm thick. The wafers come in diameters of either 7.5 or 10 cm. Before immersion into the dodecanethiol (DDT) solution, a wafer is plasma-cleaned to remove impurities, in particular those of organic origin. It is then cleaved into 1 cm-by-1 cm squares. A 1 mM solution of DDT in ethanol is prepared and the substrate samples kept under immersion for more than 10 h. Longer immersion times are avoided to prevent the possibility of multiple stacked layers of DDT molecules forming on the surface.

Twelve substrate samples are mounted on a shielded rotating holder which allow the substrates to be exposed sequentially through a 1 cm diameter hole in the shielding. The He\* source was maintained at a pressure of 11 mbar and a discharge voltage of 1200 V (Sec. 1.5.2). Exposure times typically range from 15 min to 1 h, corresponding to a dosage of 1-4 He\*/molecule of SAM respectively. To expose a substrate, it is rotated into position and a physical mask lowered to within 1 mm of the surface by a linear motion feedthrough. The mask is a copper transmission electron microscope (TEM) grid, with a wire width of 9  $\mu$ m. Before and after exposures the atomic flux can be monitored via secondary electron emission by a built-in metal surface detector (Section 1.5.3).

The complete set of exposed substrates are kept *in vacuo* until the wet etch, which is performed in a laminar flow box. We use a standard gold-etching solution of ferricyanide [29], which is kept continuously circulating by a moderately strong nitrogen gas stream directed close to the surface of the solution. A test sample is used to determine the etching time, which is then used as a guide for the other samples.

Etched samples are examined in the first instance with a light microscope. For more detailed inspection scanning electron microscopy (SEM) is employed. Figure 1.3 shows SEM (Hitachi S4500) images of the wet chemically etched surface at magnifications of 1000 $\times$ , 6000 $\times$ , and 60000 $\times$  respectively. The recreation of the TEM mask pattern as a result of the spatially selective removal of the gold layer is clearly visible here.

In previous lithography experiments performed at the ANU it was found that the edge resolution is limited by the depth of the gold layer to typically

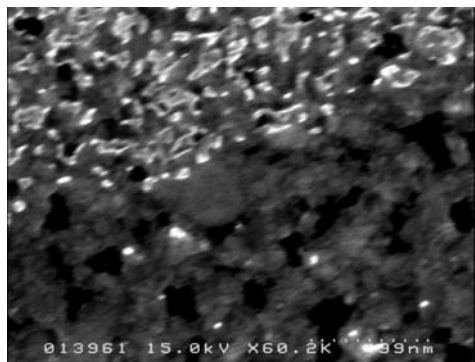
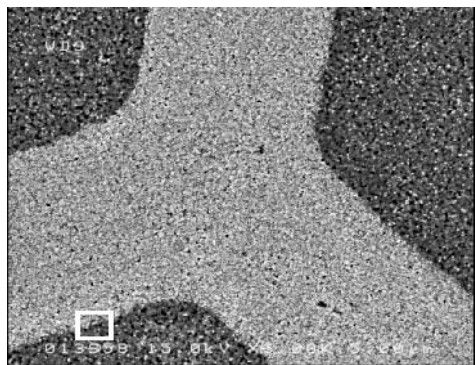
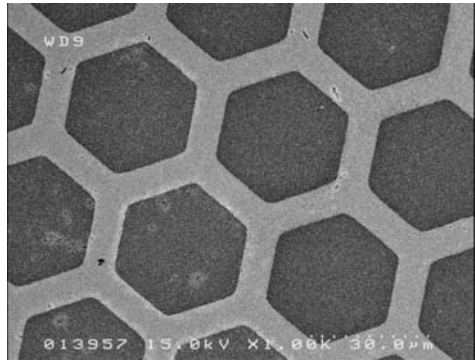


**Figure 1.3:** SEM images of a substrate exposed to a He\* beam at a source pressure of 11 mbar and a total discharge voltage of 1200 V, at 1000 $\times$ , 6000 $\times$ , and 60000 $\times$  magnification, respectively. In these images, gold appears as light and silicon as dark. The white perimeter in the second image denotes the region of interest for the last and highest level of magnification.

tens of nanometers [17]. The best resolution recorded so far is 30 nm, as measured by atomic force microscopy (AFM), with the isotropic nature of the wet chemical etching process cited as a limiting factor to greater resolution. In addition it was shown that once a structured gold-layer has been obtained, the pattern can be further transferred to the silicon substrate via reactive ion etching (RIE) techniques if desired [17].

### 1.4.2 Motivation for further beam characterization

So far I have demonstrated the ability of our experimental system to execute a standard atom lithographic procedure. In order to transform this system into one which allows detailed study of the atom lithographic process, we propose to add a stage of post-discharge particle selection which would eliminate XUV photons from the exposure process. The motivation for our proposal is as follows.

Until now, the exact mechanism which allows a  $\text{He}^*$  atom to modify the hydrophobicity of the alkanethiol monolayer has not been fully elucidated [30]. It is not understood, for example, why  $\text{He}^*$  is fifteen times more efficient at damaging a SAM surface as  $\text{Ar}^*$ , a ratio of effectiveness which is not in proportion with the relative internal energies or electron emission coefficients of the two metastable species [30].

Furthermore, basic lithography experiments such as the one previously described are in many ways ill-equipped for the unravelling of such mysteries. In Section 1.5, measurements are presented which will demonstrate that the output of a  $\text{He}^*$  discharge source typically consists of many components, including an UV-photon fraction. The presence of UV-photons somewhat hinders the possibility of performing ‘clean’ experiments which would allow an unambiguous understanding of the interaction between the  $\text{He}^*$  and the resist, as it is known that they themselves participate in several photooxidation processes of self-assembled monolayers. In an investigation of these processes, ultraviolet radiation has been shown to lead to the formation of ozone, which oxidizes the sulfur head group of the molecule, undermining its adhesion to the surface [32]. Other oxidation pathways involving direct photooxidation without the involvement of ozone have also been reported [33, 34].

Coupled with our sparse knowledge of how metastable atoms modify the hydrophobicity of the resist, the additional complication of having another highly reactive particle-class in the environment is problematic. As an illustrative example, in one recent publication [35], it was proposed that physical breaking of a C-H bond by metastable helium results in the creation of a radical in the hydrocarbon chain. One possible mechanism is for the radical to then react with oxygen from the background gas, forming an oxidized polar group which enhances the hydrophilicity of the molecule and makes it susceptible to etching. Alternatively, after the radical is formed it

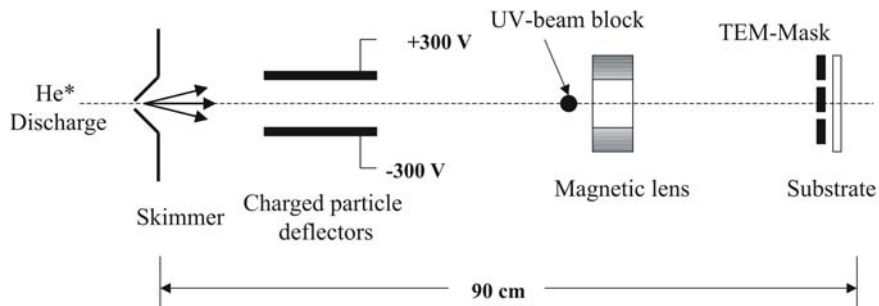


**Figure 1.4:** Conceptual schematic of an UV-free He\* lithography experiment.

may be transferred along the chain, weakening the C-S bond and result in fragmentation within the head-group itself. We note that both these proposed processes include mechanisms of oxidation and C-S bond weakening which may in some cases involve the same reaction sites as UV-mediated processes. Therefore it can be argued that even when the number of UV-photons present in the exposure is in itself insufficient to expose the substrate, it may nonetheless act as a catalyst for reaction pathways between the metastable atom and the monolayer which might otherwise not occur.

This being the case, it has been previously noted [31], that there exists a need to establish for metastable atom lithography a system which utilizes to as large extent as possible a pure He\* beam and act as a control experiment for the exposure process. As all He\* discharges produce large amounts of UV-photons however, it is not usually possible to produce a beam of UV-free metastable helium without some deliberate post-discharge manipulation of the beam.

Following the characterisation of our new He\* source, described next, my task was to begin the development of such an UV-free He\* atomic beam for atom lithography. The conceptual proposal towards this goal is schematically depicted in Figure 1.4. On emerging from the skimmer, all charged particles are removed from the atomic beam by a deflecting electric field. An UV-beam block obstructs the line-of-sight trajectory from the source to the resist-coated substrate. Thus, assuming low levels of scattered light, the exposure is ‘UV-photon free’. Meanwhile the He\* beam is focussed into the exposure region by a permanently magnetic hexapole lens. The different trajectories followed by the two particle classes is illustrated in Figure 1.5. This scheme relies heavily on the feasibility of magnetically manipulating He\* atoms travelling at longitudinal velocities of 900–1200 m/s, something I shall discuss in Section 1.6.

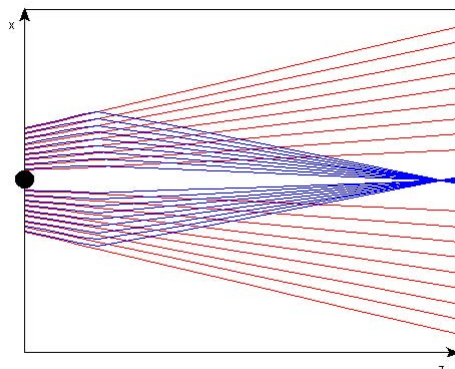


**Figure 1.5:** Schematic of proposed trajectories of  $\text{He}^*$  atoms (blue) and photons (red) in the UV-free experiment, in which the direct line-of-sight from the source to the exposure region is deliberately blocked. The lithographic exposure will take place at the position where the atomic beam is focussed into the shadow of the UV-radiation.

## 1.5 $\text{He}^*$ source characterization

In the following our standard design for a liquid-nitrogen cooled, stainless steel metastable helium source is described. As such a source for atom lithography was installed and tested for the first time during my period of work in the laboratory, it was first necessary to characterize its atomic beam properties, for which we will use a selection of the detection methods described in Section 1.5.3. This section culminates in a series of standard measurements which allows the determination of several important quantitative parameters concerning the atomic beam: the angular beam spread, the average longitudinal velocity, and the relative magnitude of the UV-photon component. We will use this information about the atomic beam for the design and simulation of our proposed UV-free system.

### 1.5.1 $\text{He}^*$ source vacuum system

The  $\text{He}^*$  discharge source forms part of a vacuum system which is partitioned into two independently sealable sections by a 25 cm diameter gate valve (Fig. 1.6). The first section is a vertical 20 cm diameter cross-piece that contains the source and the skimmer (Sec. 1.5.2). Its pressure is maintained by a oil diffusion pump at  $\sim 5 \times 10^{-5}$  torr. To prevent pump oil vapor from contaminating the vacuum, and conversely, condensable gases from entering the diffusion pump, in between the vacuum chamber and the pump is a liquid nitrogen cryogenic trap.

On the other side of the gate valve are a connected series of 20 cm- and 25 cm- vacuum sections, where apparatus for beam characterization and

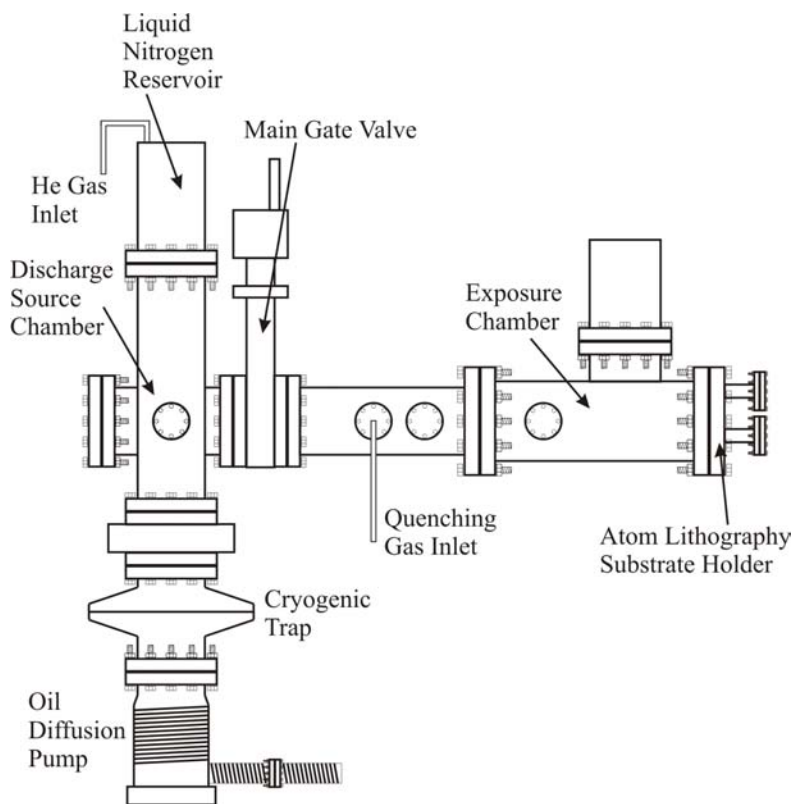


**Figure 1.6:** He\* source and vacuum system for atom lithography.

atom lithography can be installed. The length of this part of the beamline is extensible from 0.5 m to 1 m, with a pressure that is maintained at  $\sim 5 \times 10^{-6} - 1 \times 10^{-5}$  torr by a turbomolecular pump (Turbovac 150) with a pumping speed of 150 l/s.

### 1.5.2 The He\* discharge source

The production of metastable helium atoms is universally acknowledged to be an inefficient process. In even the best gas discharges, only a tiny fraction ( $10^{-5} - 10^{-4}$ ) of the atomic gas flow will gain sufficient impact from an electron collision to be excited into the metastable state [14].

In addition, metastable atoms for atom optics need to be slow enough to be effectively manipulated by light and magnetic forces within feasible distances. For example, the capture of liquid-nitrogen cooled He\* atoms with an average velocity of  $v_{av} \approx 1000$  m/s into a MOT requires further cooling by a Zeeman slower  $\sim 2$  m long [4, 14, 20]. Lowering the source temperature will allow the required length of the apparatus to be reduced in direct proportion.

Unfortunately the simultaneous pursuit of intensity and low velocity are

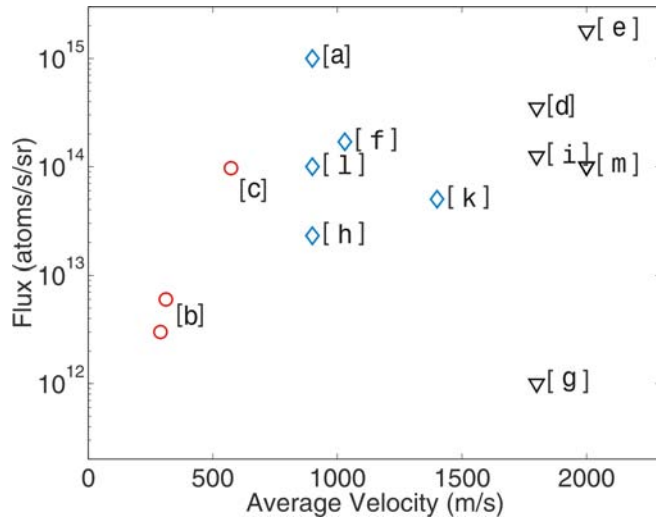


**Figure 1.7:** Comparison of the ANU liquid nitrogen-cooled He\* source (denoted as (a)) with other existing He\* sources. Triangles denote sources operated at room temperature (300 K), diamonds denote sources operated at liquid nitrogen temperature (77 K), and circles denote the new generation of He\* sources, operated at liquid helium temperatures (5 K). The labels (a)-(m) corresponds to References ([18]-[28]) respectively.

in some ways experimental contradictions. To maintain an intense discharge requires high source pressures and currents; however, a discharge with a high current running through it will undoubtedly produce very hot atoms. The need for compromise explains why many source designs continue to be refined again and again over several generations of trial-and-error [20].

The liquid nitrogen-cooled source developed at the ANU [18] represents a part of this tradition of pushing towards ever more efficient transfer of helium atoms into the metastable state at ever lower temperatures, the latest example of which is liquid-helium cooling [20]. Comparisons of the ANU design with the published parameters of other liquid nitrogen-cooled sources (Fig. 1.7) indicates that it is one of the most successful of its generation, achieving a high yield of atoms,  $\sim 10^{14} \text{ sr}^{-1}\text{s}^{-1}$ , at a relatively low average velocity ( $< 900 \text{ m/s}$ ).

The source configuration is schematically illustrated in Figure 1.8. Its mechanical components can be divided into three functional groups, which are responsible for: (i) maintenance of a dc discharge, (ii) cooling of the helium gas flow, and (iii), maintenance of a differential vacuum environment.

To excite ground-state helium into the metastable state, an electric discharge is often used. In steady-state operation, a discharge current  $\sim 6\text{-}8 \text{ mA}$  is maintained between a tungsten needle cathode, kept at  $-600 \text{ V}$  with respect to ground, and a tungsten ring anode, at  $+600 \text{ V}$ , giving a total discharge voltage of  $1200 \text{ V}$ . To start the discharge, an additional voltage pulse

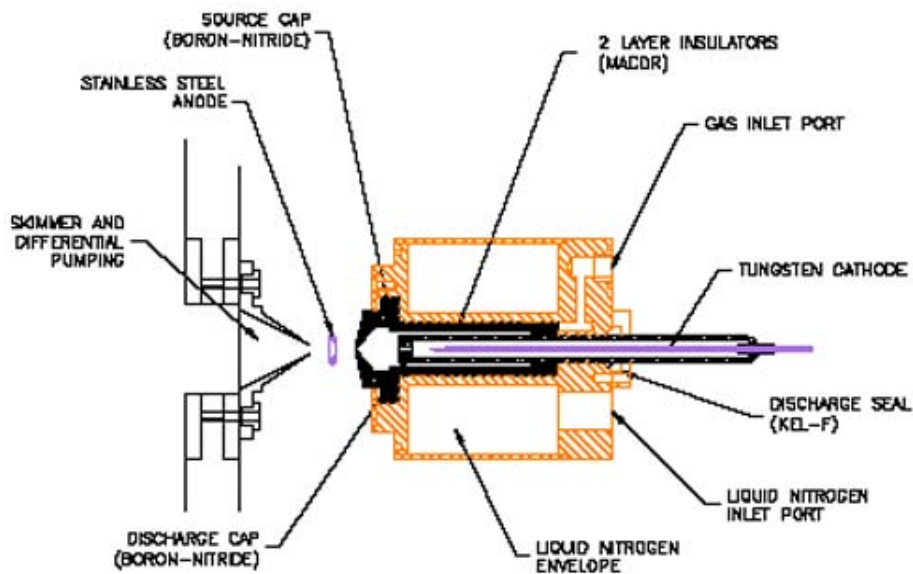


**Figure 1.8:** Schematic diagram of the liquid-nitrogen cooled He\* discharge source.

of typically  $-3$  kV is applied to the cathode for a duration of  $\sim 1$  second.

Around the cathode is a glass cylinder filled continuously with helium gas from the gas inlet port, via a channel between two tight-fitting layers of electrical insulator material (Macor). A reverse discharge from the cathode backwards to the grounded helium gas line is prevented by machining this channel in the shape of a long spiral, thus significantly increasing the electrical path length.

The double layer of Macor cladding also prevents electrical breakdown to the stainless steel liquid nitrogen envelope. Liquid nitrogen is gravity fed into this cooling envelope from an external Dewar above the source. The envelope is in thermal contact with much of the gas reservoir, and most importantly, with the source cap, into which is drilled an expansion nozzle  $210 \mu\text{m}$  in diameter. Typically the nozzle is the last point of contact between the atoms and the source, hence additional care needs to be made to keep it as well-cooled as possible. For this reason the nozzle is manufactured from boron nitride, an electrically insulating but thermally conducting ceramic. Located  $7$  mm from the nozzle of the source is the skimmer, which has a diameter of  $1$  mm.

When a metastable atom is de-excited, for example by collision with background gas, the atom is said to be ‘quenched’. The possibility of quenching occurring within the discharge is highly undesirable, and for this reason the anode is placed on the high vacuum side of the nozzle, outside the source body. In this way the afterglow of the discharge, where excitation can

take place, is drawn into a collision-free region, and the loss of metastable atoms through quenching with the reservoir gas is reduced. This solution is not without its drawbacks, as the distance between the two electrodes now becomes many times the diameter of the nozzle, requiring higher breakdown voltages and higher source pressures to maintain, typically 20-25 mbar. Overall, this tends to increase the temperature of the discharge.

### 1.5.3 Electron emission detectors

It may not be surprising that the dominant class of detectors for metastable atoms are those which utilize the large release of energy when these particles de-excite.

For some types of surfaces the energy released is greater than the work function of the surface, resulting in a measurable current of ejected electrons which is proportional to the metastable atomic flux. If the secondary electron ejection coefficient  $\gamma$  of the surface is known, the incident  $\text{He}^*$  flux may be determined absolutely.

In the case of helium in the  $2^3S_1$  state impinging on a surface of stainless steel, the secondary electron coefficient has been estimated by a combination of various methods to be  $\gamma = 0.69(3)$  [37]. In our experiment stainless steel targets are often used in combination with a positive voltage grid to remove the ejected electrons. Ultimately, atomic flux measurements obtained this way can only be considered good estimates, as the value of  $\gamma$  varies to some degree from surface to surface, and depends on surface cleanliness [38]. Therefore, to truly use this method accurately, the  $\gamma$  of a specified surface must first be independently calibrated with methods such as those employed *et al.* [37].

Secondary electron emission is also the basis of more sophisticated methods of detection. Two devices which are used frequently in our laboratory are channeltron electron multipliers and microchannel plates (MCP). In both devices, an electron ejected by an incident  $\text{He}^*$  atom triggers off an amplification cascade of electrons which are accelerated to the back of the channel by a high external voltage. A channeltron consists of one such channel wound into a spiral. A micro-channel plate is an array of such channels set in a glass substrate, which allows it to give spatial as well as dynamic information concerning the incident atomic beam.

### 1.5.4 Beam profile and time-of-flight measurements

The transverse velocity distribution determines the angular spread of the atomic beam and can be characterized by a measurement of the transverse beam profile. A self-contained measurement unit consisting of a stainless steel target and a positive voltage grid is moved across the atomic beam with a linear motion feedthrough, and the secondary electron emission current is

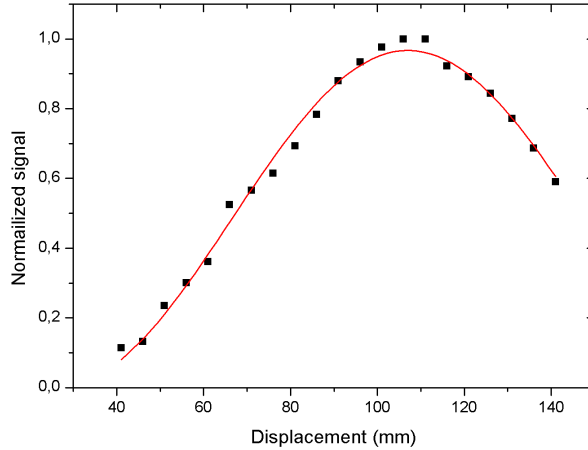


**Figure 1.9:** The transverse beam profile of the atomic beam as measured at a distance of 45 cm from the skimmer, at a source pressure of 15 mbar and a discharge voltage of 1200 V. Employing a cosine-squared fitting function, an angular beam spread of  $90 \pm 2$  mrad was obtained.

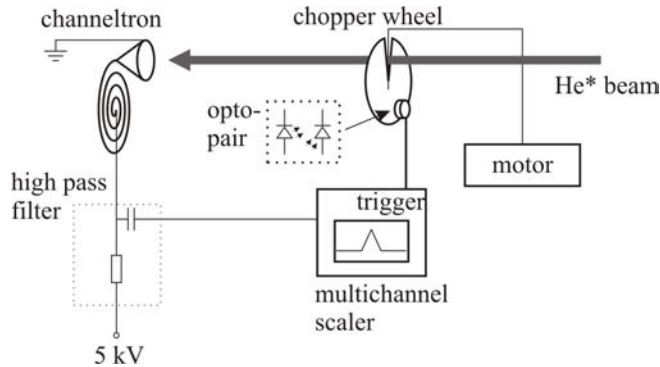
measured at each point of displacement.

Figure 1.9 shows a typical, normalized transverse profile of an atomic beam emerging from a skimmer of diameter 0.5 cm, after expanding for a longitudinal flight length of 45 cm. For this measurement the source was operated at a pressure of 15 mbar, and a discharge voltage of 1200 V. The profile can be fitted by assuming a cosine-squared distribution [39], from which it is possible to estimate that the angular beam spread has a value of  $90 \pm 2$  mrad.

The longitudinal velocity distribution can be characterized by a time-of-flight (TOF) measurement, in which the velocity of a particle is inferred from the time it requires to traverse a defined distance within the apparatus.

The atomic beam is first chopped to create a pulse of particles, consisting of a mixture of UV-photons and atoms (Figure 1.10). Our mechanical chopper has a diameter of 100 mm, with a 3 mrad slit, and rotates at  $\sim 60$  Hz. The combination of the chopper slit and a 1 mm pinhole at the front of the detector ensures that the signal comes only from a collimated beam and reduces extraneous signal from stray reflections.

After a flight path of length  $L = 620$  mm, the arrival of particles is detected by a channeltron detector. Typically two signals are observed, one from the arrival of UV-photons, and a second from the later arrival of metastable helium atoms. In the context of this measurement the photon signal can be considered instantaneous, and thus serves as the reference point for the start of the flight time  $t_0$ .



**Figure 1.10:** Experimental set-up for time-of-flight measurement.

The channeltron signal is received by a multi-channel scaler, a device which is triggered every time a hole in the chopper wheel sweeps across an opto-reflective switch. This is followed by computer acquisition and analysis where, by using the transformation  $v = L/(t - t_0)$ , a velocity distribution of the atomic beam can be obtained.

It is known that the form of this velocity distribution will vary depending on whether the gas flow out of the expansion nozzle is effusive or supersonic. An effusive atomic beam results when a trapped gas, in thermal equilibrium with itself, is released such that mean free path of the atoms  $\lambda_0$  in the gas is equal to or greater than the diameter of the hole  $D$ , i.e. no collisions occur during the expansion process.

As the probability that a particle will escape through the hole is proportional to its velocity, it has been found that the velocity distribution of the beam from a thermal source is not solely a Maxwell-Boltzmann distribution but such a distribution weighed by  $v$  [39], giving:

$$P(v)dv = \frac{2}{\alpha^4} v^3 \exp\left(-\frac{v^2}{\alpha^2}\right) dv \quad (1.5)$$

where  $\alpha = \sqrt{2k_B T/m}$ ,  $T$  the absolute gas temperature in the source,  $m$  is the mass of the atoms, and  $k_B$  is Boltzmann's constant.

At high source pressures,  $D \gg \lambda_0$ , particles in the gas suffer many collisions as they escape. The collision of fast particles into the slower particles in front of them effectively narrows the velocity distribution around a mean velocity  $v_0$  that is greater than the average velocity of particles within the source itself. Hence the velocity distribution of a supersonic beam has the form of a displaced standard Gaussian:

$$P(v)dv = C v^3 \exp\left(-\frac{(v - v_0)^2}{\Delta v^2}\right) dv \quad (1.6)$$

where  $C$  is a normalization constant, and  $\Delta v$  is the width of the distribution.

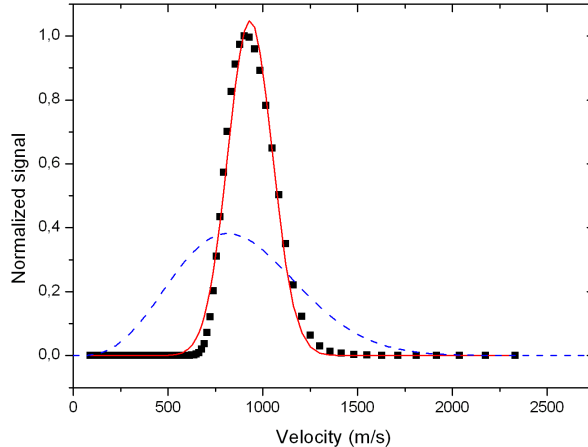


**Figure 1.11:** Velocity distribution of the He\* atomic beam for a source pressure of 11 mbar, normalized to a peak value of unity and fitted with a supersonic (solid line), and effusive (dashed line) velocity distribution, respectively.

As an example, Figure 1.11 shows the velocity distribution obtained with the time-of-flight method for a source pressure of 11 mbar and a discharge voltage of 1200 V. Fitting this particular dataset with Equation 1.6, we can extract values for the average longitudinal velocity and the velocity spread  $v_0 \pm \Delta v = 885 \pm 170$  m/s. To illustrate that the gas flow in this case is indeed best described as supersonic, the velocity distribution of an effusive beam source with the same average velocity is included for comparison.

The operational conditions of the discharge is very much dependent on the source pressure, as illustrated by the sequence of plots in Figure 1.12. We find firstly that the current through the discharge increases with source pressure (plot 1), and that, despite continuous cooling, the expansion nozzle heats up by at least several degrees, as measured by a thermocouple on the boron nitride surface close to the nozzle opening (plot 2).

Lastly, an increase in the He gas flow can be correlated to an increase in the average velocity of the atomic beam (plot 3), giving a velocity range from 900 - 1200 m/s as a function of the source pressure. Such a longitudinal velocity range is comparable to what was measured for the original liquid-nitrogen cooled source, whose working parameters are given in Ref. [18], and is to be expected given that both sources are of the same design. For the numerical simulations that follow, we will assume intermediate source pressures and take the longitudinal velocity of the atomic beam to be 1000 m/s.

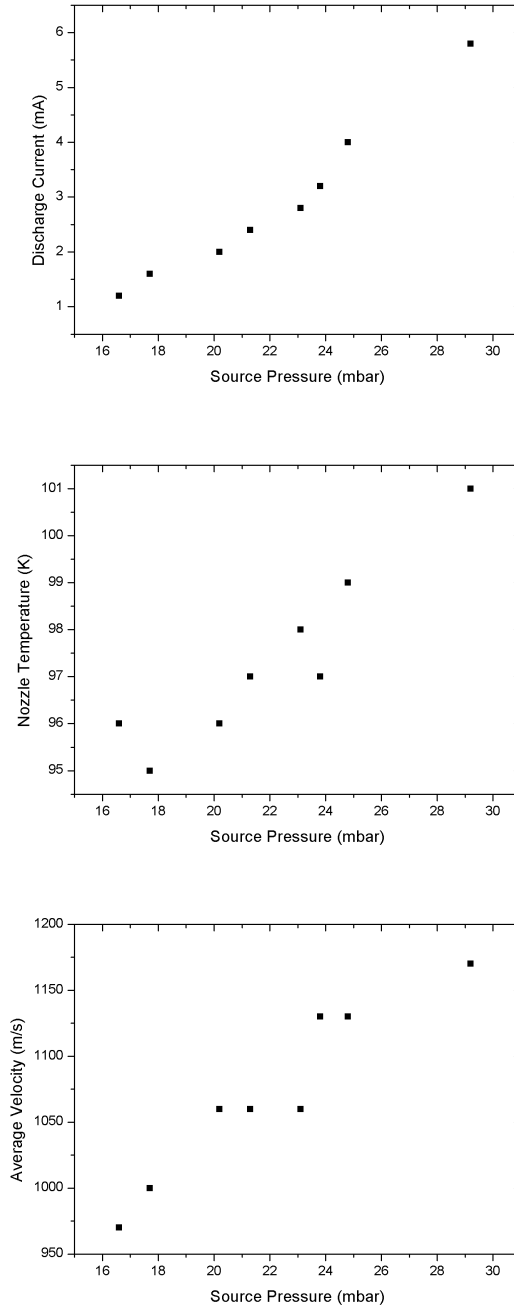


**Figure 1.12:** The dependence of discharge current, nozzle temperature, and average atom velocity respectively on the source pressure.

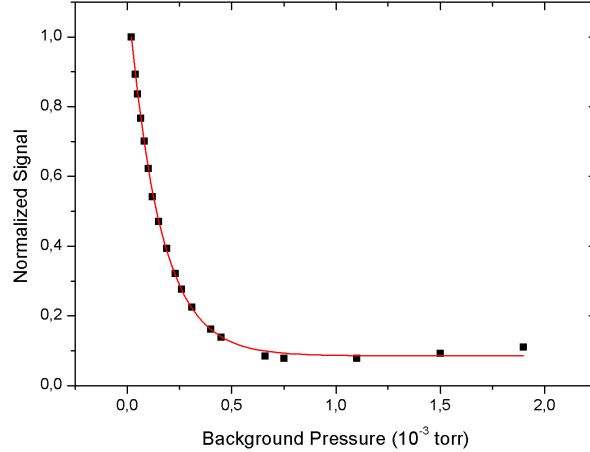


**Figure 1.13:** Determination of UV-photon contribution by quenching with argon gas, with an exponential decay fit, at a source pressure of 10 mbar and a discharge voltage of 1200 V. The residual signal at a background pressure of  $> 1 \times 10^{-3}$  torr is approximately 8 % of the total.

### 1.5.5 Quenching Experiments

As the output of the discharge contains many constituents, independent measurements dedicated to separating and quantifying these components are required. This is particularly the case for the separation of UV-photons and metastable helium atoms - both discharge products are energetic and neutral, making them, in normal circumstances, difficult to detect in isolation.

The typical signal detected by an electron emission detector placed in the atomic beam is proportional to the sum of the metastable atomic and the UV-photon flux. Therefore elimination of one or the other component allows the relative proportions of the two particle classes to be deduced. Experimentally, it is far easier to eliminate metastable helium atoms from the atomic beam by, for example, the deliberate application of  $\text{He}^*$  quenching. In a quenching experiment, argon or nitrogen gas is gradually introduced into the vacuum system, resulting in the systematic de-excitation and loss of the metastable helium population through background gas collisions. The residue secondary electron current at steady-state can then be attributed to the remaining photon fraction.

Quantitative measurement of the residual current using the technique described above is shown in Figure 1.13, for the  $\text{He}^*$  source operated at a pressure of 10 mbar and a discharge voltage of 1200 V. From the fitting parameters it is possible to determine that UV-photons make up  $8.2 \pm 0.6$  % of the total secondary electron emission signal. We note that in general, the

UV flux varies by less than a factor of 2 with source conditions, and that subsequent measurements of the UV flux of this source have yielded similar results as this one [40]. Furthermore, after subtracting this percentage from the total signal we can infer that the He\* output of the discharge source ranges from  $3 \times 10^{14}$ – $1 \times 10^{15}$  sr<sup>-1</sup> s<sup>-1</sup>, depending on source conditions.

## 1.6 Magnetic manipulation of He\*

The sequence of characterization measurements outlined above is essential for our development of a system for eliminating ultraviolet radiation from the exposure. As we have seen our experimental plan proposes to designate different trajectories for atoms and photons through magnetic manipulation. That being the case, prior knowledge of the spatial and velocity characteristics of the atoms will allow us to determine what kind of magnetic manipulation is required for a practicable solution.

### 1.6.1 Hexapole magnetic lens

Magnetic fields have been used to manipulate thermal atomic beams since the earliest experiments with atoms [39]. The advantage of the magnetic manipulation experiment of today is that, with the advent of new types of ceramic rare-earth permanently magnetic materials, it has become feasible to focus even thermal atomic beams within distances of tens of centimeters.

Since such a manipulation is based on the magnetic dipole force, it can be applied to any particle with a non-zero magnetic moment. This versatility offers several practical advantages, such as the possibility of using the same magnetic component for vastly different atomic beams. The hexapole lens described in the following has been used to manipulate cesium [44], metastable helium, and most recently, metastable neon [40].

An atom with magnetic moment  $\mu$  will interact with a magnetic field of magnitude  $B$  with a potential energy

$$V = -\vec{\mu} \cdot \vec{B} \quad (1.7)$$

such that the force on the atom with a constant magnetic moment can be written as

$$\vec{F} = \nabla(\vec{\mu} \cdot \vec{B}) = (\vec{\mu} \cdot \nabla) \vec{B} \quad (1.8)$$

where we have assumed the magnetic moment is independent of the field gradient. We see that if  $V$  approaches a simple harmonic oscillator potential, the force on the atom is proportional to its displacement from the central axis of the potential, thereby acting to bring all particles to a single point of focus along the axis. For atomic focussing the magnetic substate of interest

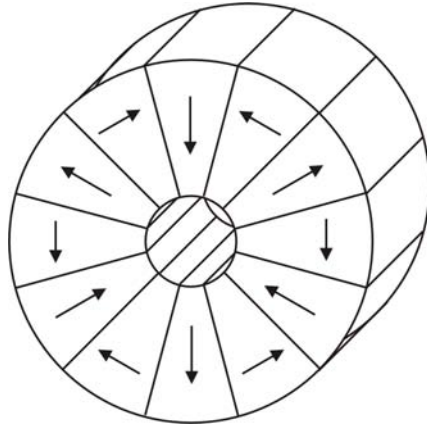


**Figure 1.14:** Schematic diagram of the magnetic hexapole lens, including the orientation of the magnetization of individual segments.

is the low-field seeking state, i.e., when the magnetic moment  $J$  is antiparallel to the external magnetic field, and  $\vec{\mu} \cdot \vec{B} = -\mu B$ . Atoms in the  $J = -1$  and  $J = 0$  states are respectively either defocussed or unaffected by the magnetic lens. Therefore, as there is no way to state-prepare the atoms in our experiment, we can expect that only one-third of the atomic population will be focussed by the magnetic lens.

Such a magnetic component acts as a magnetic analog of an optical lens, and can be constructed with a six- or hexapole magnetic field configuration. It can be shown, that the cylindrical arrangement of three pairs of magnetic poles with alternating surface magnetic potentials gives a field [44]

$$B(r, \theta) = B_0 \left( \frac{r}{r_0} \right)^2 \left[ 1 - 2 \left( \frac{r}{r_0} \right)^6 \cos 6\theta + \mathcal{O} \left( \frac{r}{r_0} \right)^{12} \right]^{1/2} \quad (1.9)$$

For our proposed experiment, in which we will not be primarily interested in the detailed imaging properties of the lens, we will consider only the dominant term, which is quadratic as desired.

Attempts to construct hexapole magnetic lenses for atoms have used either current-carrying wires [19], or permanent magnetic material [41]. A permanent magnet system has the advantage of significantly steeper field gradients. To give an experimentally realistic example, it has been reported by Woestenenk *et al.* that, for the purpose of flux enhancement, their group can achieve a magnetic flux curvature of  $\partial_r^2 B_0 = 0.6 \text{ T/cm}^2$  by running a current of 20 A through their current-based hexapole lens, but continuous currents higher than 20 A could not be sustained without cooling [19]. This can be compared to a typical curvature of  $2.3 \text{ T/cm}^2$  for a permanent magnetic lens in the hexapole configuration [42].

Therefore, structures from permanent magnets bypasses the technical difficulty of adequately dissipating the heat generated by conducting large

currents *in vacuo*, and as such are our method of choice. To construct a permanently magnetic hexapole lens, the continuous rotation of magnetization required is approximated by segments of magnetic material, each with a stepwise rotated magnetization with respect to the neighboring segment, as shown in Figure 1.14. This results in a potential that can be approximated by the following expression:

$$U(r, z) = \mu \partial_r^2 B_0 r^2 S(z) \quad (1.10)$$

where  $\mu = 2\mu_B$  is the magnetic moment,  $\partial_r^2 B_0$  the magnetic flux density curvature, and the envelope function  $S(z)$  describes the spatial dependence of the potential in  $z$ .

An expression for the density curvature  $\partial_r^2 B_0$  can be obtained by first considering the case of an ideal magnetic hexapole, created by continuously rotating the direction of magnetization around a ring of inner radius  $r_1$ , outer radius  $r_2$ , and infinite length. It can be shown [43, 44] that this cylindrically symmetric potential can be decomposed into Fourier components, such that

$$\partial_r^2 B_{0,ideal} = \frac{3B_R K}{r_1^2}, \quad (1.11)$$

where

$$K = \frac{1}{2} \left( 1 - \frac{r_1^2}{r_2^2} \right) \quad (1.12)$$

is the Fourier coefficient for a hexapole, and  $B_R$  is the magnetic remanence of the lens material. In our case,  $B_R = 1.12\text{T}$ .

When the rotation of the magnetization is not continuous but segmented into twelve discrete components, Eq. 1.11 can be modified by a correction term  $G$ , such that  $\partial_r^2 B_0 = G \partial_r^2 B_{0,ideal}$ , where

$$G = \frac{\sin(n+1)\pi/S}{(n+1)\pi/S} \quad (1.13)$$

with the order of the multipole  $n = 3$  and the number of segments  $S = 12$  for the hexapole lens depicted in Fig. 1.14.

Finally, the finite length of the lens leads to a gradual decay of field strength which can be approximated by Glaser's bell-shaped curve:

$$S(z) = \frac{1}{(1 + \frac{z^2}{d^2})^2}, \quad (1.14)$$

where the fitting parameter is the characteristic length  $d$ . Following actual experimental parameters, in which we will use a hexapole lens of dimensions  $r_1 = 7.5$  mm,  $r_2 = 15$  mm, and length  $L = 25$  mm, the resulting equipotential surface is shown in Figure 1.15.

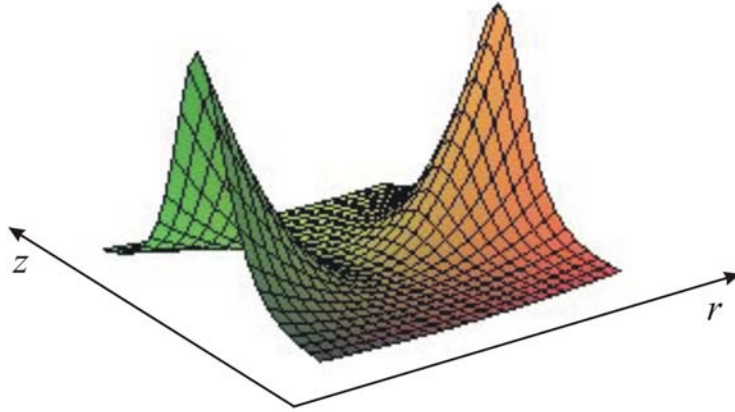


**Figure 1.15:** Equipotential surface of the hexapole magnetic lens for low-field-seeking atoms (Eq. 1.10). Due to the finite length of the lens the radially harmonic potential decays at both edges, which is here described by Eq. 1.14.

In the first instance it is useful to derive for the magnetic hexapole lens an equivalent of the thin lens equation. Taking the paraxial approximation, it can be shown that the focal length  $f$  is given by:

$$f = \frac{mv^2/2}{\mu_B \partial_r^2 B_0 L} \quad (1.15)$$

where  $m$  is the mass of the atom,  $v$  its velocity, and  $L$  is the length of the lens.

We find that for a beam of  $\text{He}^*$  with an average longitudinal velocity in the range that we have previously measured, i.e. 900–1200 m/s,  $f \sim 25$ –45 cm. These are lengths which can be readily accommodated within the experimental setup. The relatively high longitudinal velocities of a thermal atomic beam can thus be compensated for by the use of high-gradient magnetic components. However, the remaining effects caused by the large beam spread of such beams are much more difficult to control. This can be very clearly demonstrated through a numerical simulation, as follows.

## 1.6.2 Particle Optics Approach

A particle- or ray-optics approach is a simple method for analyzing atom optics experiments where the velocity of the atoms is high and wave-like effects such as diffraction is negligible. The atomic beam is described as consisting of individual particles each of which follow trajectories determinable by classical mechanics.

A numerical simulation can be implemented which calculates the trajectories of each particle given its initial position and velocity. The radial equation of motion of atoms in our system exhibits cylindrical symmetry and can be expressed as:

$$\ddot{r} + \frac{1}{m} \frac{\partial U(r, z)}{\partial r} = 0 \quad (1.16)$$

where  $r$  is the radial, and  $z$  the longitudinal spatial coordinate.

Following the analytical approach of McClelland *et al.* [45, 46], first developed for describing the focussing of atoms in a laser beam standing wave, Equation 1.16 can be parameterized in terms of the longitudinal displacement  $z$  as:

$$\begin{aligned} \frac{d}{dz} \left[ \left( 1 - \frac{U(r, z)}{E_0} \right)^{1/2} (1 + r'^2)^{-1/2} r' \right] \\ + \frac{1}{2E_0} \left[ 1 - \frac{U(r, z)}{E_0} \right]^{-1/2} (1 + r'^2)^{1/2} \frac{\partial U(r, z)}{\partial r} = 0 \end{aligned} \quad (1.17)$$

where  $E_0$  is the incident kinetic energy of the atom and  $r'$  is the differentiation of  $r$  with respect to  $z$ .

Two distortive phenomena which we will almost immediately disregard for this application are ‘spherical aberrations’ and diffraction limiting effects. It has been experimentally demonstrated [42] that the anharmonicity of the potential makes only a minor contribution to the distortion of the image, and furthermore the deviation of the hexapole lens potential from an ideal harmonic potential is less than 10% for more than 60% of the aperture area [14]. Likewise the de Broglie wavelength is in our case on the order of 50 pm, which, assuming a clear aperture of about 10 mm, gives a negligible wave diffraction limit of approximately 5 nm.

Although compared to the output of an effusive source a supersonic atomic beam has a relatively narrow velocity spread, there will remain nonetheless a variability in the time that the alternately faster and slower atoms spend in the focussing potential. To estimate the extent of the resulting chromatic aberration, the numerical model above was used to stimulate a atomic population with an average velocity of 1000 m/s and a longitudinal velocity spread of 200 m/s, the values previously determined by time-of-flight. The resulting trajectories and beam profile at  $z = f$ , where  $f$  is the focal length as calculated with the thin lens equation, are shown at the bottom of Figure 1.16. We find the longitudinal velocity spread broadens the bottom of the profile into a pedestal but the width of the profile at half maximum is still less than 1 mm, making chromatic aberration a tolerable effect for our purposes.

In principle we can investigate a whole series of particle optic effects in the manner just illustrated. However, it has been suggested [3] that the

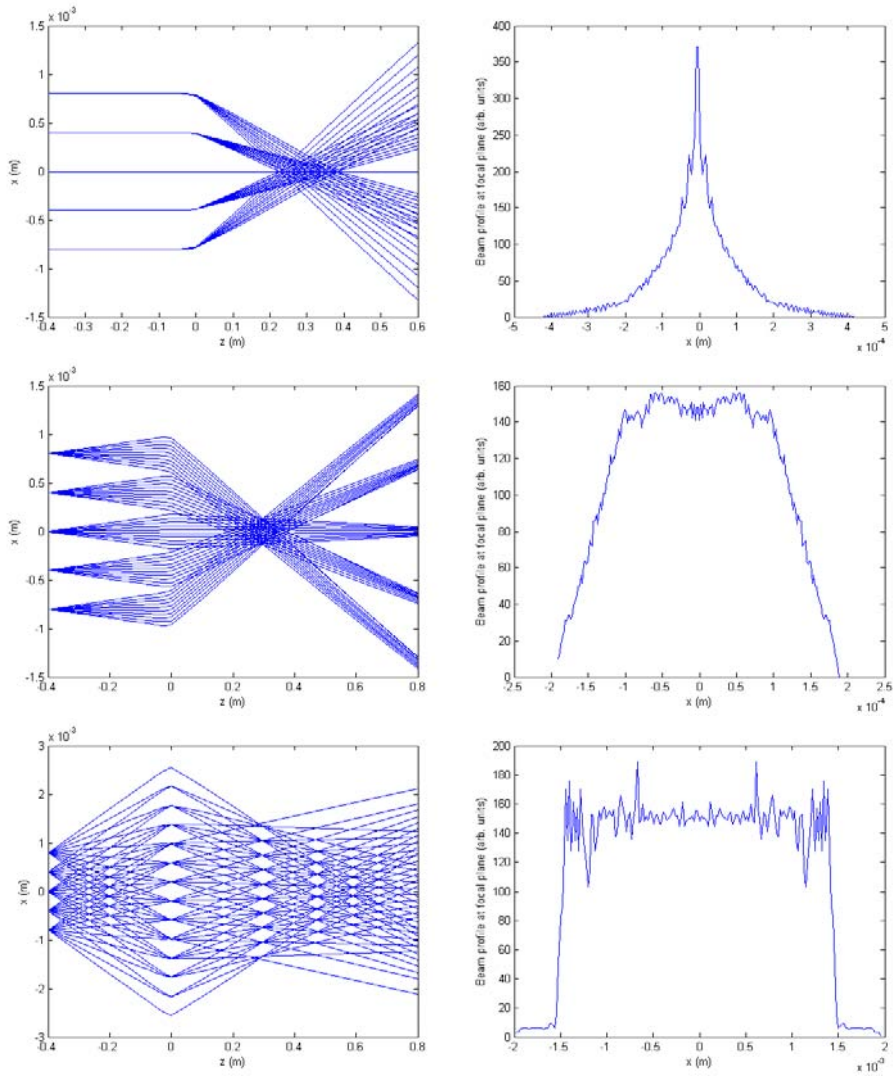


**Figure 1.16:** Numerical simulations of aberration effects. In the top row, the effect of chromatic aberration is demonstrated. The left-hand side show the simulated particle trajectories, the right-hand side the beam profile at the focal point as determined by the thin-lens equation. In the bottom two rows the effect of low- (0.5 mrad) and high- (5 mrad) initial angular spread on magnetic focussing is shown.

angular beam spread of the incident beam has by far the largest impact on the quality of the focussing achieved. In the case of a thermal beam the effect is arguably large enough to mask all other, more subtle contributions, and therefore we will now consider this effect principally and in isolation.

Solving Equation 1.17 for varying initial atomic beam spread allows the influence of a large angular beam spread to be simulated. Two examples will be given, one for an atomic beam whose angular spread has been reduced by transverse laser-cooling to  $\theta = 0.5$  mrad, the other for a thermal atomic beam, which we assume is physically collimated to  $\theta = 5$  mrad. This approximation is close to the actual experimental parameters, since the aperture of the hexapole lens limits the acceptance angle to  $\sim 5$  mrad. We will also assume that the longitudinal velocity is constant at  $v_0 = 1000$  m/s.

In Figure 1.16 the trajectories and beam profile at  $z = f$  are shown. It can be seen that sending an atomic beam with properties such as those we expect to find in our experiment through a hexapole lens will produce a significantly widened focal spot approximately 3 mm in diameter, which is also in agreement with an estimate made from the thin lens relation  $\Delta r = f\theta$  [3]. Also, we find that instead of an identifiable focus the narrowest part of the beam is found anywhere between  $z = 30$ – $50$  cm. This is the case even though we have already neglected to consider chromatic aberration by assuming that the longitudinal velocities of the atoms are identical.

In summary, the results presented in Figure 1.16 demonstrate that chromatic aberrations affect the focussing of the beam significantly less than the angular beam spread of the atomic beam. This strongly suggests that, should the opportunity arise for making an improvement of the experiment in the future, the strongest imperative for this project is to establish a transverse laser-cooling system of the atomic beam. Furthermore, these results serve to emphasize our prognosis that, for a thermal beam, the use of magnetic manipulation techniques is unsuitable for pursuing imaging applications, but can be used for enhancing the beam flux and moderate deflection of the beam.

### 1.6.3 First evidence of magnetic manipulation

The first attempts at magnetic manipulation utilized the experimental setup shown in Figure 1.17. As indicated, aligned on a longitudinal rail system are a pair of electric field deflectors, kept at  $+300$  V and  $-300$  V respectively, an externally-controlled motorized needle to act as the UV-beam block, and the magnetic lens, which was positioned 40 cm downstream of the skimmer. The  $\text{He}^*$  atomic beam was operated at a source pressure of 10 mbar and a discharge voltage of 1200 V.

To observe magnetic focussing, a MCP detector is placed under an external accelerating voltage of 5 kV, 40 cm from the magnetic lens at the end of the experimental chamber. A phosphor plate behind the MCP emits a

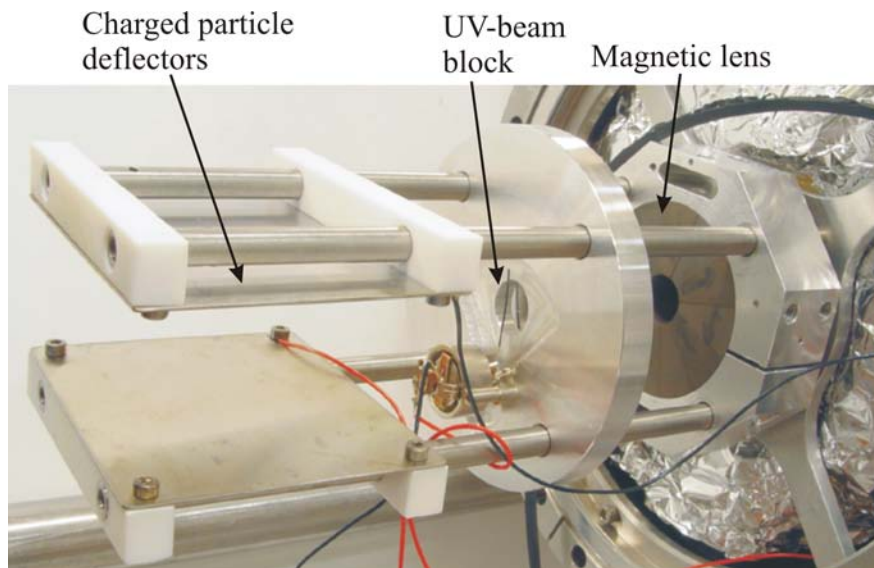


**Figure 1.17:** Experimental setup for UV-free He\* atom lithography.

fluorescent signal on receiving an electron pulse. These fluorescent images are captured through a port window by a CCD camera outside the vacuum chamber.

Cross-sections from these first images show that, after the background has been subtracted, the signal from metastable atoms focussed into the shadow of the needle is on the order of  $\sim 30\text{-}50\%$  of the maximum signal (Figure 1.18). In an atom lithography experiment, the resist within this area should be exposed to a greatly reduced UV-photon level. The level of UV-photons remaining will need to be independently determined with the techniques of Section 1.5.

The images also show segmentation patterns due to the corresponding segmentation of the hexapole lens. The imperfections caused by approximating what is ideally a continuously changing magnetic field with twelve segments become apparent when the size of the atomic beam fills the aperture of the lens. In Figure 1.19 the image contrast has been lowered so that this effect can be more clearly seen. Such segmentation patterns were also observed in the first experiments with this type of magnetic lens [44] with a thermal cesium atomic beam.

## 1.7 Conclusion

In this chapter I have documented the full cycle of development of an atom lithography experiment, from the installation and characterization of a liquid nitrogen cooled discharge source, to the execution of plans to further isolate the metastable atomic beam from other constituents so as to perform atom

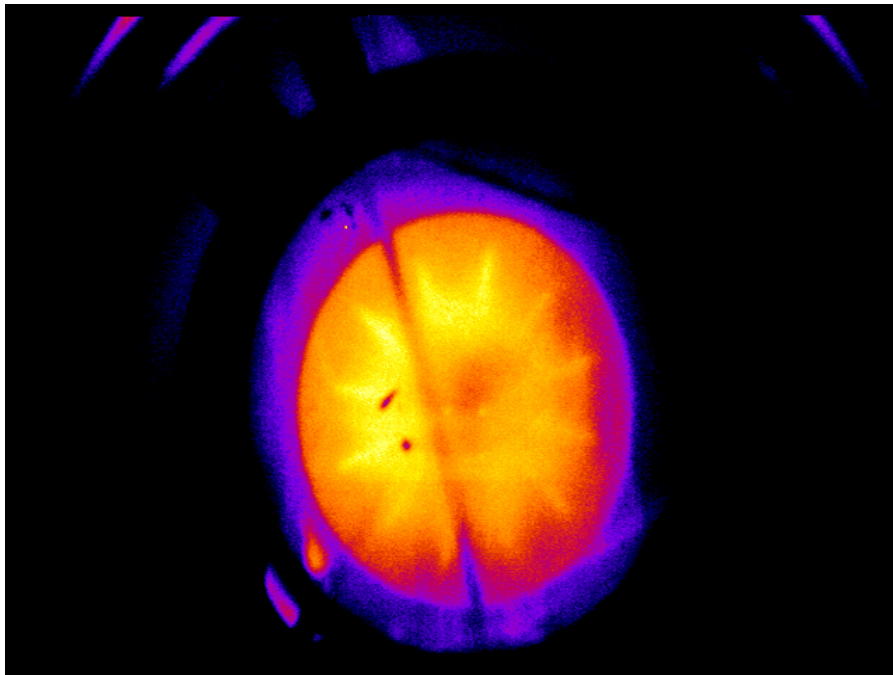


**Figure 1.18:** Atomic beam image after magnetic manipulation – the shadow of the UV-beam block runs diagonally across the center of the image. The scale is approximately 1:1.5.

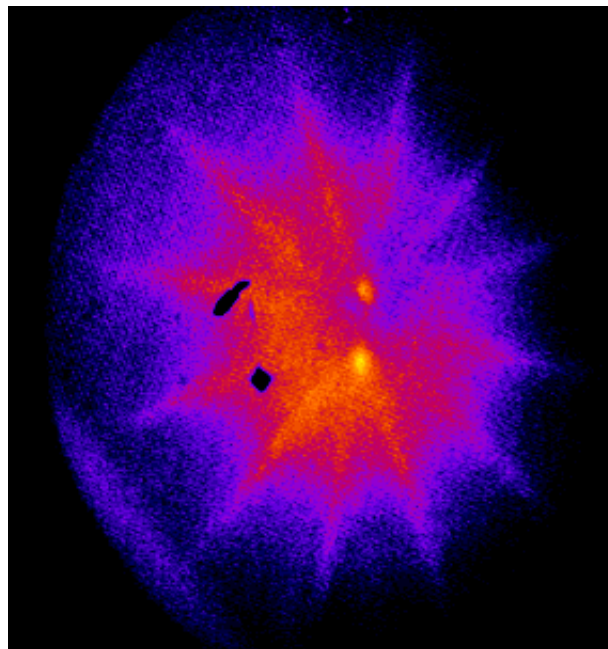


**Figure 1.19:** Atomic beam image after magnetic manipulation, with lowered contrast. Note: the needle has been moved out of the atomic beam and is not visible in this image.

lithography in increasingly well-defined conditions. In addition, I explained how the experimental route proposed here is motivated by the need to fully explain the interaction between metastable rare gas atoms and the self-assembled monolayer, many aspects of which so far remains uncertain.

Through time-of-flight measurements, it can be determined that the output of the discharge source is a supersonic beam with a mean longitudinal velocity range of 900-1200 m/s and a spread of  $\pm 170$  m/s. This velocity distribution produces a population of atoms which are moving sufficiently slowly for us to contemplate implementing magnetic focussing techniques. The feasibility of magnetic manipulation is furthermore enhanced by the development of permanent magnetic components for atom optics, which allow the application of strong field gradients over a small spatial extent.

Hence, our experiment is not immediately limited by the average longitudinal velocity of the atoms, and focussing can be achieved within a mean focal length of  $\sim 35$  cm. It can be shown numerically however, that as a result of the large angular spread of the atomic beam, only coarse manipulation of the atomic trajectories can be realistically expected. We have therefore aimed towards the use of magnetic focussing as a means for overall flux enhancement, and designed an experiment for which the ability to deflect the atomic beam by a small amount allows us to perform atom lithography in an UV-free environment. Using the setup described here, such lithography experiments have subsequently been carried out at the ANU [40].



## Chapter 2

# Binary bosonic mixtures: re-thermalization and species-selective evaporative cooling

To observe the interaction of any two arbitrary objects it is necessary, in the first instance, that both those objects are confined to a common location for a sufficient period of time. In the study of heteronuclear interactions between atoms, we would furthermore prefer that the kinetic energy of the atoms be small, as their repertoire of interactions are then quantum mechanically restricted to selected collisional processes, and the subsequent analysis simplifies substantially.

Over and above a scientific triumph in itself, the way towards Bose-Einstein Condensation (BEC) provided a highly evolved technical blueprint for the preparation of cold and ultracold atomic gases. The creation of a condensate intrinsically satisfies the requirements for spatial confinement and efficient temperature reduction, and its techniques extend readily to a range of atomic species.

Therefore as the relative ease with which a BEC is produced worldwide increases, it is somewhat natural that for many groups the next level of complexity manifests itself in experiments which involve taking heteronuclear collections of atoms into the ultracold regime. By applying the tools of Bose-condensation to more than one atomic species simultaneously, they seek to form ultracold mixtures of atomic gases and molecular quantum gases whose interactions can be manipulated with unprecedented control, just as a Bose-Einstein condensate is itself an embodiment of large-scale experimental control over the external and internal degrees of freedom of a many-particle system.

## 2.1 Cold atom experiments at the University of Bonn

Building on previous work on the physics of single particles [52], the ultracold mixture experiment at the University of Bonn ultimately seeks to address topics directed at the boundary between single- and many-particle physics. This boundary can be visualized by imagining particles being continuously added to a system initially populated by a single particle. From condensed matter physics we expect that the growing system must at some point start to exhibit many-particle behavior, characterized by the existence of quantum correlations between the members of the ensemble.

Experimentally, an equivalent model system can be realized by immersing a small number of atoms in a quantum degenerate buffer gas. Such an experiment in addition offers the potential to (i), establish a high degree of control over the motional state of the single dopant particles, and (ii) investigate correlated pairs of particles. Consequently the possible directions for research can be conceptually summarized as:

- the exhibition of many-particle concepts in small samples of atoms,
- use of a quantum degenerate gas to control the properties of a small number of dopant or impurity atoms, and,
- deterministic creation of single molecules.

We propose to immerse an atomic sample of between 1 and 100 dopant cesium atoms in a condensate of rubidium. Cesium atoms are in this case the dopant of choice due to the significant amount of knowledge already accumulated on the behavior and control of single atoms of cesium at Bonn (see, for example, References [47]-[54]). The combination of these single particles with a quantum gas buffer allows this knowledge to be extended into the ultracold, and perhaps also molecular, regimes.

To develop a mixed species system in which one species is designated to play the role to a large thermal reservoir, we require that the mechanism of heat exchange between the reservoir and the sample be well-understood. Experimentally this amounts to understanding the efficiency of sympathetic cooling of cesium by rubidium, or in other words, the elastic collisional behavior of these two atomic species. Concurrently, inelastic collisions must also be considered in order to take into account the expected losses to atom number at certain stages of the experimental protocol.

The steps which have been made towards the experimental goals outlined above, and are described in this chapter, are:

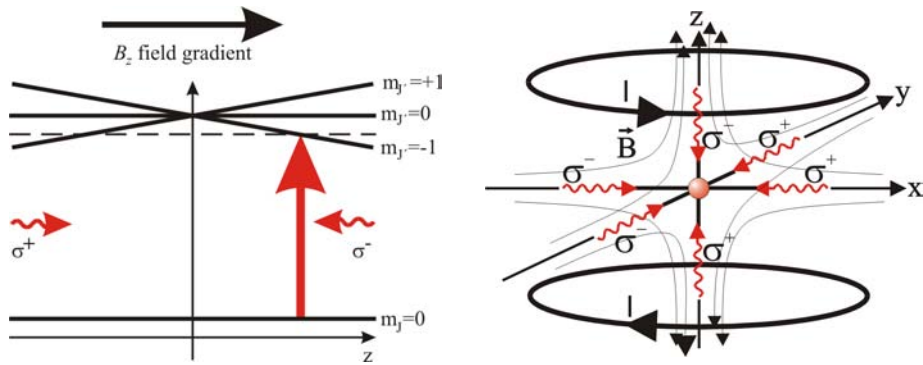


**Figure 2.1:** Magneto-optical trap (MOT). In the one dimensional picture (left), a magnetic field gradient lifts the degeneracy of the excited Zeeman sublevels. Therefore an atom travelling away from the magnetic minimum will move into resonance with a laser beam which applies a restoring force to the trap center. To apply this principle in three-dimensions (right), a pair of current-carrying coils in the anti-Helmholtz configuration provides the required linear field gradient.

**Magneto-optical trapping of Cs and Rb.** (i) Frequency stabilized laser systems were implemented for the cooling and trapping of cesium, and the original Rb Bose-condensation experiment was modified to support laser beams for cooling and trapping at 780 and 852 nm simultaneously. (ii) Simultaneous magneto-optical trapping of Rb and Cs was achieved, followed by observation of inter-species light-mediated interactions.

**Simultaneous transfer to a magnetic trap and re-thermalization.**

(i) Atomic clouds of both species were loaded into a quadrupole and an Ioffe magnetic potential respectively. (ii) The first observation of inter-species re-thermalization in the quadrupole potential was made.

**Bose-condensation through species-selective evaporative cooling.**

(i) Hyperfine evaporative cooling for species-selective temperature control was implemented, and used to bring the Rb atomic cloud to quantum degeneracy. (ii) Three-body losses in a Rb Bose-condensate were characterized, and the consequences for an ultracold Cs-Rb mixture at high densities explored.

## 2.2 Simultaneous magneto-optical trapping of Rb and Cs

Quantitative evidence that clouds of cesium and rubidium atoms overlapped in space interact with each other at an appreciable rate can already be found in the very first stages of the cooling and trapping process, when both species

are simultaneously confined in a magneto-optical trap (MOT) [14]. Flooded with resonant light from all directions which drive excited state processes, the MOT by no means represent an ideal environment for collisional studies. Nonetheless it is here that the behavior of the atomic clouds can be first observed to differ phenomenologically as a result of their proximity.

Furthermore, functionally the MOT is the source of atoms for confinement and investigation of the atomic mixture in a magnetic trap. The number, density, and temperature of the atomic cloud in the MOT therefore dictates many characteristics of the binary mixture in the magnetic trap experiments which follow from Section 2.6 onwards.

A detailed description of the MOT can be found at [14]. We will first note that a cloud of atoms in a resonant laser beam of photons will gain momentum in the direction of the beam, as well as suffer from random momentum kicks due to spontaneous emission of the absorbed photons. When the frequency of the beams are set below the frequency of the selected atomic resonance, the scattering force becomes velocity dependent due to the Doppler effect, investing it with the characteristics of a damping force.

In a MOT, such motional damping is combined with the use of circular polarization and a linear magnetic field to confer trapping characteristics. As the magnetic field increases radially from the center of the trap, it lifts the degeneracy of the excited Zeeman sublevels, causing atoms to preferentially absorb light of one polarization (figure 2.1, left). The dissipative force now acquires a directionality and position dependence, which, for atoms illuminated by counter-propagating beams in all three dimensions, induces spatial confinement (figure 2.1, right). Taken all together, for typical laser beam intensities at or close to saturation, atoms in a MOT can be visualized as exhibiting a highly over-damped, harmonic oscillator motion.

In a system where atomic clouds of two different species are in this way confined and overlapped in space, we expect the diffusive motion of the individual atoms to sometimes result in intraspecies collisions. These collisions are often accompanied by the loss of one or both atoms, an effect we will encounter in Section 2.5 which serves to (i) further motivate the benefits of collisional studies in a conservative potential, and (ii) account for a unavoidable loss in atom number in the magnetic trap. Construction of the two-species MOT involved an experimental setup which we will describe for the respective species in the next two sections.

## 2.3 Production of ultracold rubidium

The creation of a Bose-condensate imposes a set of relatively stringent experimental criteria, therefore when a BEC experiment is used as the starting point for an excursion into cold atomic mixtures, it brings with it operational standards which satisfy many of the requirements for its new role.

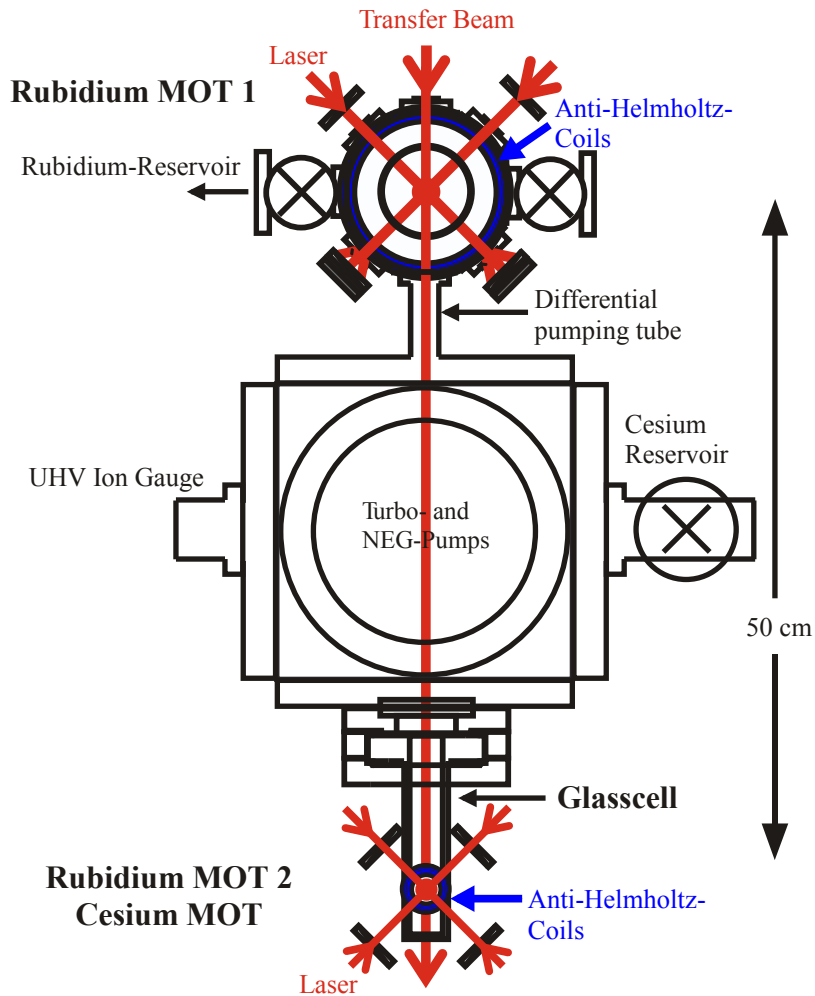


**Figure 2.2:** Sideview of the vacuum system. Labelled are the locations of the two Rb MOTs, MOT 1 and MOT 2, and the Cs MOT. Laser beams are depicted in red, coils in blue.

In this section a brief description of the rubidium system is provided, for the purpose of introducing the core experimental structure which acts as the platform for the modifications introduced later.

### 2.3.1 Main vacuum system

The series of vacuum chambers within which the atomic clouds are collected and stored are schematically depicted in Figure 2.2. Located in the upper vacuum chamber is a magneto-optical trap (MOT 1), which operates in the vicinity of the rubidium reservoir and acts as the first point of collection of cold rubidium atoms, to be supplied to a second magneto-optical trap in

the differentially pumped experimental region in the square glass cell below (MOT 2).

The upper MOT captures Rb atoms from background vapor with a partial pressure (Rb) of  $\sim 10^{-9}$  mbar. It is built in an octagonal steel vacuum chamber with seven port windows providing optical access for three retro-reflected MOT beams, and the vertically oriented transfer beam, respectively. The three MOT beams are  $\sim 2$ cm in diameter, with a power of approximately 30mW in each beam at the cooling transition. In one direction is a repumper beam (Sec. 2.3.2) superposed, with a power of  $\sim 3$ mW. Two anti-Helmholtz configured coils surround the chamber, producing a quadrupole field gradient of  $\sim 12$  Gauss/cm along the symmetry axis. The number of Rb atoms collected here is typically on the order of  $1-2 \times 10^9$ .

From this sector of the vacuum system, a tube 8mm long and 3mm in inner diameter leads to the the differentially pumped main section, typically maintained at  $\sim 10^{-11}$  mbar. The ultra-high vacuum is maintained by a combination of a turbopump based on magnetic bearings (Model TCM180, manufactured by Pfeiffer) with a pumping speed of 180 l/s, and a non-evaporable getter pump (manufactured by SAES) based on the getter alloy Zr-V-Fe. The pre-vacuum of the turbopump is maintained by a second small turbopump, and a membrane pump. Installed close to the pump region is a hot cathode ionization based sensor (Model Ionivac IE 514, manufactured by Leybold), specified to be reliable down to  $1 \times 10^{-12}$  mbar.

The collected atoms are transported through the differential pumping tube to the UHV MOT, by the divergent transfer beam, whose frequency is kept in near resonance to the cooling transition. This second MOT (MOT 2) is located in a 30 mm  $\times$  30 mm  $\times$  120 mm glass cell (manufactured by Hellma) with walls 5 mm thick, and anti-reflection coated outer surfaces. Sandwiching it on either side are two coils in the anti-Helmholtz configuration, and a third coil which adds a dipole potential for the Ioffe trap configuration. All coils are water-cooled.

From this point on the experimental setup for Rb and Cs begins to diverge, and shall be described separately in the next sections. Other sources of information on parts of the following experimental details can be found in References [55] and [56].

### 2.3.2 Laser system for Rb

For the cooling and trapping of Rb atoms we require a total of four laser sources at 780 nm:

**MOT cooling laser.** The cooling laser is operated at approximately  $2.5 \Gamma$  below the  $F = 2 \rightarrow F' = 3$  cycling transition, where  $\Gamma$  is the natural linewidth (figure 2.3).

**MOT repumping laser.** As part of maintaining atoms in the  $F = 2 \rightarrow$

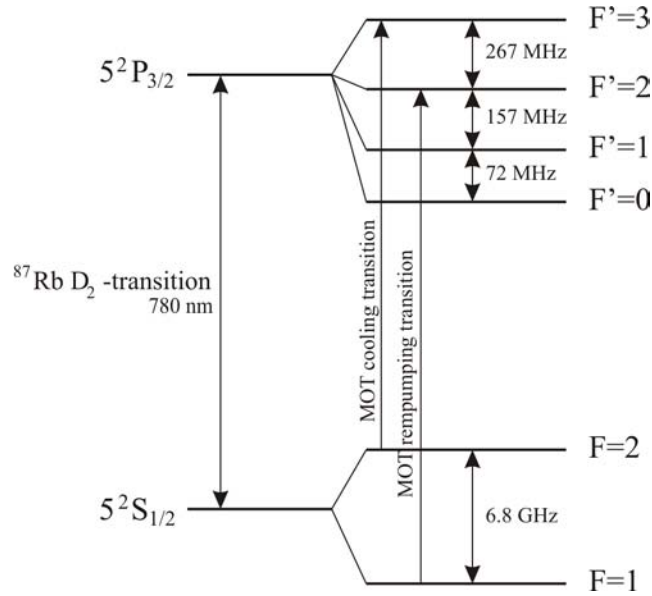


**Figure 2.3:** Level scheme of the rubidium D<sub>2</sub>-line. Indicated are the transitions used for cooling and repumping in the MOT.

$F' = 3$  cycling transition, it is necessary to take into account the non-negligible probability that an atom is off-resonantly excited to the  $F' = 2$  level, from which it is possible to spontaneously decay into the  $F = 1$  ground state (Fig. 2.3). Subsequent re-entry into the cooling cycle is then not achievable with the cooling laser alone, due to the large hyperfine splitting between  $F = 1$  and  $F = 2$ . This suggests the use of a repumping laser to the  $F = 1 \rightarrow F' = 2$  transition, from which atoms can return to the  $F = 2$  ground-state.

**Probe laser.** For absorption imaging (Section 2.3.3), we require a probe laser, at the  $F = 2 \rightarrow F' = 3$  transition.

**Reference laser.** Finally, for heterodyne referencing of the cooling laser we have a fourth laser, also resonant to the  $F = 2 \rightarrow F' = 3$  transition.

Although we require additional laser frequencies  $F = 2 \rightarrow F' = 2$  and  $F = 1 \rightarrow F' = 2$  for optical pumping (Section 2.6.2), they can be drawn from the cooling and repumping laser beams respectively, and in the case of the cooling laser light, down-shifted to the right frequency with an acoustic-optical modulator (AOM).

All the above experimental requirements for laser light are supplied by external grating stabilized diode lasers based in the Littrow-design. Each laser is independently held to a predetermined frequency with a precision of better than 2 MHz by active stabilization locking schemes. In the case of

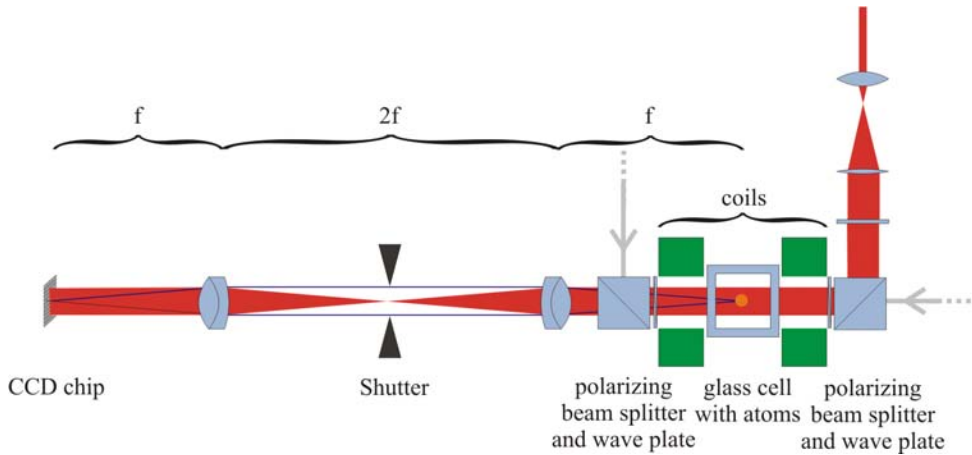


**Figure 2.4:** Schematic diagram of the optical setup for absorption imaging. The imaging beam is expanded by a double lens system and directed into the glass cell through the use of a half-waveplate followed by a polarizing beamsplitter cube. As the light traverses the vacuum cell parts of it are absorbed by the atomic cloud, resulting in a shadow which is imaged onto a CCD chip by a one-to-one imaging system. The shutter prevents leaked MOT laser light, the direction of which is indicated by light-colored arrows, from damaging the CCD chip.

the system of lasers at 780 nm the DAVLL (Dichroic Atomic Vapor Laser Lock) [57] locking scheme is used exclusively.

In addition the frequency of all lasers is referenced absolutely by saturation spectroscopy. Where the detuning of the laser from resonance must be known with greater accuracy, the frequency is further monitored by creating a heterodyne beat signal to the designated reference laser.

In general the diode lasers have a power output in the range of 10-15 mW. A notable exception is the laser maintained close to the cooling transition, i.e.  $F = 2 \rightarrow F' = 3$ , of rubidium. Due to the heavy requirement for power at this frequency, this laser is coupled to a tapered amplifier chip, giving it the capacity to supply an output power of approximately 0.5 W.

The laser light is guided to the experiment by single-mode polarization preserving optical fibers with a coupling efficiency from 30 to 50%.

### 2.3.3 Absorption imaging system

To detect the atomic cloud, the trapping forces are removed and the expanding cloud imaged with absorption imaging techniques onto a CCD chip. Almost all quantitative data pertaining to the ultracold atomic cloud is extracted from absorption images of the cloud in various stages of expansion.

Our imaging system is set up as follows (figure 2.4). A probe laser is maintained at resonance to the  $F = 2 \rightarrow F' = 3$  or  $F = 4 \rightarrow F' = 5$

transition, for Rb and Cs respectively. Emerging collimated from the fiber coupler, the beam size is expanded by a telescope before it is overlapped with a MOT beam at a polarizing beam splitter cube. The beam then transverses the glass cell containing the atomic cloud before being detected by the CCD chip (Model FT18, manufactured by Philips) through a pair of lenses arranged to form a  $4f$ -imaging system, where  $f = 12$  cm. This allows the cloud to be imaged in one-to-one proportion to the object itself. For rapid switching on and off of the probe beam during exposure we employ an acoustic optical modulator (AOM) as a fast switch.

An image processing protocol utilizing three images is employed. The first image is taken of the atomic cloud after the designated expansion time. A second image is taken without the presence of atoms, and a third in the absence of both atoms and probe light. These images are then processed according to the relation

$$T(x, y) = \frac{I_A(x, y) - I_D(x, y)}{I_B(x, y) - I_D(x, y)} \quad (2.1)$$

where

$$I_A(x, y) = P(x, y)e^{-D(x, y)} + N(x, y) \quad (2.2)$$

$$I_B(x, y) = P(x, y) + N(x, y) \quad (2.3)$$

$$I_D(x, y) = N(x, y) \quad (2.4)$$

are the absorption, bright-field, and dark-field image respectively.  $P(x, y)$  is the profile of the probe beam,  $D(x, y)$  is the optical density of the cloud, and  $N(x, y)$  is the contribution other than the probe light, such as background light and stray counts.

Having obtained the transmission image  $T(x, y)$ , the optical density of the cloud  $D(x, y)$  can be found from the relation:

$$T(x, y) = e^{-D(x, y)} \quad (2.5)$$

where,

$$D(x, y) = \sigma n_c(x, y). \quad (2.6)$$

Here  $\sigma$  is the absorption cross section, and  $n_c(x, y)$  is the integrated column density of the atomic cloud.

For  $I \ll I_{sat}$ , where  $I_{sat}$  is the saturation intensity, the on-resonance absorption cross section is given by

$$\sigma = \frac{\hbar\omega\gamma}{2I_{sat}} \quad (2.7)$$

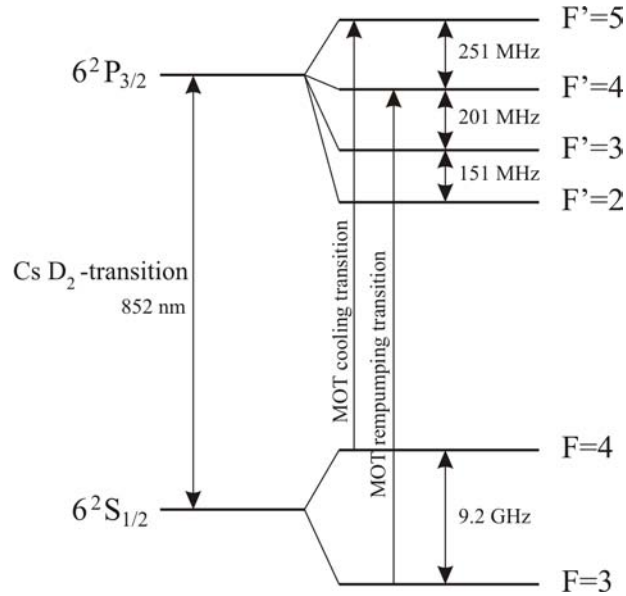


**Figure 2.5:** Level scheme of the cesium D2-line. The transitions used for cooling and repumping in the MOT are indicated.

where  $\omega$  is the frequency of the light,  $\gamma$  is the photon scattering rate, and  $\Gamma$  is the natural linewidth.

The  $D(x, y)$  so obtained can then be fitted by a two-dimensional Gaussian for further analysis. Furthermore, the total atom number  $N$  can then be deduced from the optical density and absorption cross-section with the help of the relation

$$N = \sum_{i,j=1..n} \frac{AD(x_i, y_j)}{\sigma} \quad (2.8)$$

for a CCD chip consisting of  $n \times n$  pixels, each of area  $A$ .

## 2.4 New additions for cooling and trapping cesium

As each change to the existing experiment brings about other perturbations, we strived to make the additions necessary to the cooling and trapping of atomic cesium with the minimal amount of disturbance to the Bose-condensation experiment already described. Our approach is documented in the following section.

### 2.4.1 Laser system for Cs

We required the implementation of a new system of lasers at 852 nm with roles analogous to the lasers in our established rubidium system. The system

comprises of three laser sources in total, all in the vicinity of the cesium D2-transition at 852 nm (figure 2.5). As for the other laser system we employ diode lasers in a Littrow configuration, in this case in conjugation with home-built current and temperature controllers. These lasers and the optics for their frequency stabilization and monitoring are located on a separate optical table from the main experiment. Further experimental details of the 852 nm optical systems, including schematic diagrams, can be found in Appendix B.

### **The MOT cooling laser**

The MOT cooling laser is locked to the  $F = 4 \rightarrow F' = 5$  cycling transition, with a detuning below resonance of  $\sim 1.9 \Gamma$ . Like its 780 nm counterpart the cooling laser is frequency stabilized by a DAVLL locking scheme. Saturation spectroscopy and a reference heterodyne signal are used to monitor the frequency of the laser.

### **The MOT repump laser**

In direct analogy to the laser cooling scheme of rubidium (Sec. 2.3.2), the continuous cooling of cesium atoms require repumping laser light. The repumping laser returns atoms which have been off-resonantly pumped by the cooling laser to the  $F = 3$  ground state into the cooling cycle, and is resonant to the  $F = 3 \rightarrow F' = 4$  transition.

In our experiment this laser is frequency stabilized by polarization spectroscopy of cesium vapor cells. Frequency monitoring is accomplished through saturation spectroscopy.

### **The reference and probe laser**

The output of one laser diode serves both as the reference beam for the formation of a heterodyne signal with the MOT cooling laser and as a probe beam for absorption imaging of the cesium atomic cloud.

To facilitate this dual usage, the laser source is locked to the  $F = 4 \rightarrow F' = 4/5$  crossover, 125.5 MHz below the cooling transition. The beam is then divided into two beams. One is heterodyned with the cooling laser to produce a beat signal for referencing that laser with respect to the cooling transition.

The other beam is designated for use in the resonant illumination of the atomic cloud for imaging. The requirement for rapid switching suggests the use of an AOM. We use an AOM with variable frequency modulation (Model 3110-120, manufactured by Crystal Technology), such that on a single pass the light beam is up-shifted by exactly 125 MHz. Thus by locking the laser emission to the  $F = 4 \rightarrow F' = 4/5$  crossover we are able to simultaneously

provide a known frequency reference for the heterodyne signal of the cooling laser and make use of AOM-controlled switching for the probe beam.

### 2.4.2 Specialized optics and optical layout

Apart from the reference lasers, all the laser sources described so far eventually feed into optical fibers that terminate around the vicinity of the vacuum system. To create a mixed species MOT, cooling and repumping laser beams at both 780 and 852 nm must be overlapped and directed into the glass cell.

As much as possible, we have maintained the original system of optics. The use of dichroic mirrors which transmit at 852 nm but reflect at 780 nm allowed light for the cesium MOT to be inserted into strategic points of the existing optical system for the Rb MOT (Appendix B). Wherever necessary, dielectric mirrors and other optical components for 780 nm were replaced with substitutes which are anti-reflection coated for both wavelengths.

We have also recently acquired custom dual-wavelength waveplates (manufactured by Lens Optics). These are multiple order optical components with a thickness such that they operate as  $\lambda/2$ -plates for one wavelength and  $\lambda$ -plates for the other. Thus the power distribution in each MOT beam, which is divided through a combination of  $\lambda/2$ -plates and polarization beamsplitter cubes, can be adjusted for each wavelength independently. The first set of waveplates were specified to have a retardation of  $17 \cdot \lambda - \lambda/75$  at 780 nm and  $(15 + 1/2) \cdot \lambda + \lambda/75$  at 852 nm. For the purpose of independent power distribution, measurements with a test setup indicate that these waveplates will allow us to vary the intensity of the laser beam at 852 nm from 10 to 100% of its maximum transmitted intensity while maintaining <2% variation in the intensity of a superposed laser beam at 780 nm.

All MOT beams for both Rb and Cs have a beam diameter of  $\sim 1.5$  cm. The MOT trapping beams at the cooling transition has a power density of  $1.3 \text{ mW/cm}^2 \approx I_S$  for Cs, and  $2 \text{ mW/cm}^2 \approx 1.2 I_S$  for Rb, respectively. Both MOTs were operated at a magnetic field gradient of  $\zeta_x = \zeta_y = 6 \text{ Gauss/cm}$  and  $\zeta_z = -12 \text{ Gauss/cm}$ , where  $z$  is the symmetry axis of the coils. To observe the loading of the Cs and Rb MOTS, photodiodes equipped with interference filters allow us to separate and monitor independently their fluorescence signals.

## 2.5 Loading a mixed species MOT

The fluorescence signals in figure 2.6 depict the loading of Rb in the presence of loaded Cs, and Cs in the presence of loaded Rb, respectively. The marked decrease in cesium atom number decreases in response to the loading of Rb is clearly visible. In contrast, the Rb atom number is not measurably affected by the presence of trapped Cs.

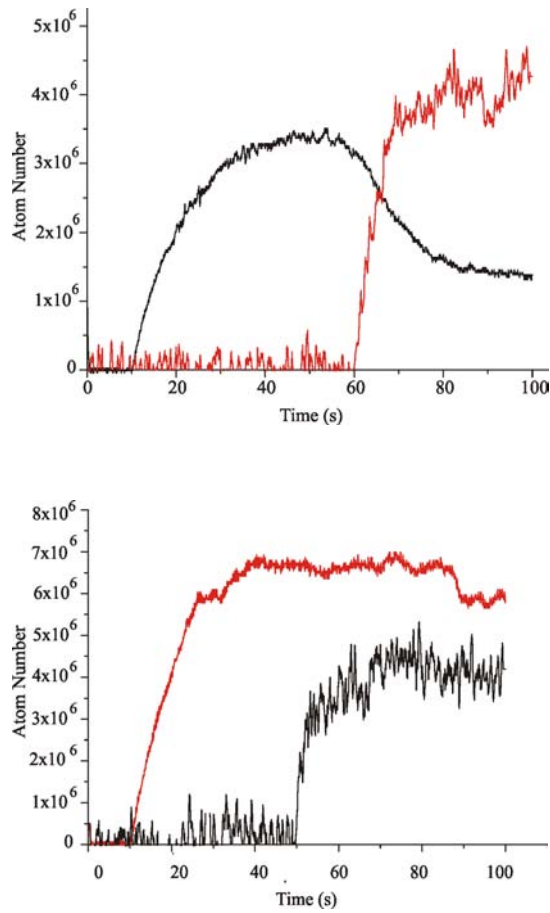


**Figure 2.6:** Sequential loading of the mixed species rubidium-cesium MOT. The top plot shows the fluorescence signal of cesium atoms loading (black line) followed by rubidium (red line). The bottom plot shows the results of performing the opposite loading sequence; here rubidium (red) is loaded first, followed by cesium (black). The two fluorescence signals are measured by separate calibrated photodiodes, from which atom numbers are deduced based on the solid angle of fluorescence collected by the photodetector, and the estimated photon scattering rates  $\gamma_{Rb}$  and  $\gamma_{Cs}$  for Rb and Cs atoms, respectively.

This significant loss of Cs atoms due to the presence of Rb can be attributed to a combination of hyperfine-changing ground-state and light-mediated heteronuclear collisions between trapped atoms. The net effect of intra- and inter-species collisions on the cesium atom number can be summarized in a rate equation as

$$\frac{dN_{Cs}}{dt} = L_{Cs} - \gamma_{Cs}N_{Cs} - \beta_{Cs} \int n_{Cs}^2 dV - \beta_{Cs,Rb} \int n_{Cs}n_{Rb} dV \quad (2.9)$$

where  $L_{Cs}$  is the loading rate of cesium,  $\gamma_{Cs}$  is the coefficient for losses due to collisions with the background gas,  $\beta_{Cs}$  is the coefficient for collisions between two trapped cesium atoms,  $\beta_{Cs,Rb}$  is the corresponding coefficient for collisions between a trapped rubidium and a trapped cesium atom, and  $n_{Cs}$  and  $n_{Rb}$  is the density of the cesium and rubidium MOT respectively.

Knowing that the number of trapped cesium atoms is small compared to trapped rubidium, we firstly expect that only a small proportion of the total atom loss will be due to Cs-Cs collisions. Furthermore, numerical analysis of the fluorescence signal of the MOTs indicate that  $\beta_{Cs}$  is at least three times smaller than  $\beta_{Cs,Rb}$  [55]. Neglecting therefore losses due to intraspecies collisions, we find that the interspecies loss coefficient  $\beta_{Cs,Rb} = (2.25 \pm 0.24) \cdot 10^{-10} \text{ cm}^3\text{s}^{-1}$  [56].

Comparisons with the loss rates reported by other groups for various combinations of magneto-optically trapped alkali mixtures indicate that the loss rate observed by us is relatively large [61, 62]. In general the presence of a strong radiation field modifies the collision dynamics in ways which are often not very well described by simple phenomenological approaches. In this instance at least, it would appear that the trapping parameters of our system are in favor of a strong coupling between the two species.

For the purely practical purpose of loading both species into a magnetic trap simultaneously (Section 2.6.1), it is worth noting that the effect just illustrated represents at steady-state a drop in trapped cesium to  $\sim 60\%$  of what is achievable when this MOT is operated in isolation. This is a significant and unforeseeable cost in atom number to take into account.

### Effect of additional source on vacuum conditions

As noted previously, the major advantage of a double MOT system is the ability to maintain a ultra-high vacuum — there are two orders of magnitude difference between the background pressure surrounding the reservoir and UHV MOT (MOT1 and MOT2, respectively). However, one consequence of loading the Cs MOT directly from the background gas in the differentially pumped region is that a certain amount of degradation to the vacuum conditions there is to be expected. Here in brief is how we propose to maintain optimal vacuum conditions now and in the future.

Currently we work with moderate numbers of trapped Cs, and the previous measurements, for example, were obtained at a background pressure of  $1 \times 10^{-9}$  mbar. Working in our favor is the rapid rate at which the quality of the vacuum recovers; on closing the Cs reservoir we can return to pressures on the order of  $5 \times 10^{-11}$  mbar after pumping out the chamber for 12-15 hours.

In addition we note that, in its more advanced stages, the number of Cs atoms required for the experiment is relatively small, on the order of several tens to hundreds, and as a consequence the partial pressure of Cs in the UHV region could eventually be substantially decreased. In contrast, there will always be a demand for a large thermal reservoir of ultracold Rb atoms, and it would be extremely difficult to maintain ultra-high vacuum conditions and concurrently collect a sufficiently large Rb atomic cloud without implementing a more sophisticated scheme, such as a double-MOT system.

Finally, we have also had recent success with ultraviolet light-induced atom desorption [59], and would utilize this effect to a greater extent in the future.

## 2.6 Interspecies re-thermalization in a conservative potential

Although it is certainly possible to extract some insight into the collisional properties of two atomic species from their interactions in a magneto-optical trap, such an approach requires taking into account the atom trap parameters and the presence of excited states of both species, concerns which become superfluous for a population of ground-state atoms stored in a dark, conservative potential.

The physical overlap of two clouds of spin-polarized atoms in a magnetic trap allows both species to predominantly interact in the absence of losses from binary collisions. If the thermal energies of the atomic ensembles are initially unequal, the rate of interspecies scattering can be deduced from the rate of approach towards a thermodynamic equilibrium between the two ensembles. Apart from being a useful parameter in itself, the inter-species scattering rate or collisional cross-section so obtained also determines the efficiency of sympathetic cooling.

In this section, the simultaneous transfer of rubidium and cesium from the overlapped magneto-optical traps into a magnetic trapping potential is described. This is followed by an analysis of our experimental observation of interspecies re-thermalization in the quadrupole magnetic trap, the results of which motivates the next section on the development of species-selective temperature control.

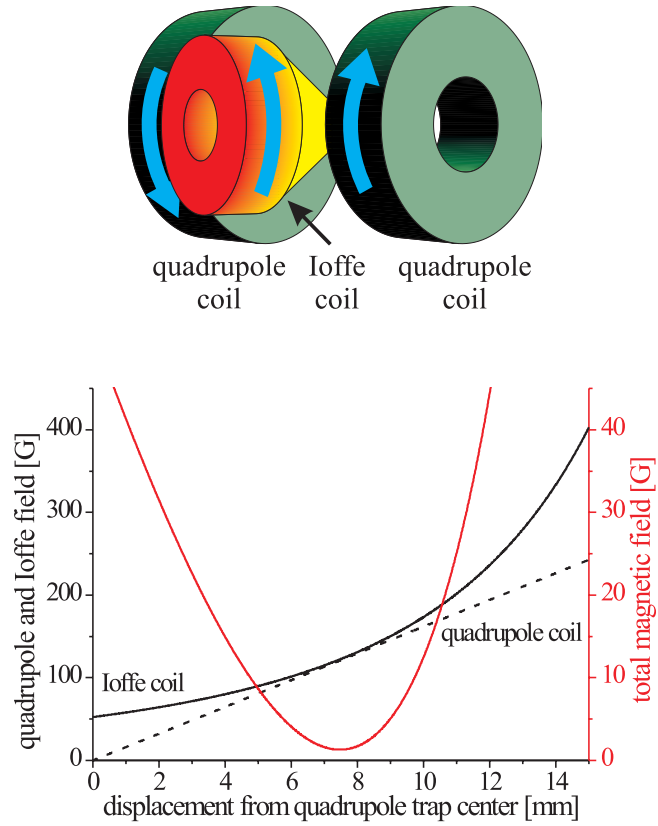


**Figure 2.7:** The QUIC trap configuration is composed of two quadrupole coils and an Ioffe coil (top). The direction of the current flow is depicted by the arrows. The magnitude of the magnetic fields along the symmetry axis of the Ioffe coil, as a function of displacement from the quadrupole trap is shown in the bottom part of the figure. The two quadrupole coils contribute a linear field (dotted line), while the Ioffe coil produces a dipole field (solid line). These fields have opposite signs and therefore partially cancel to produce a net magnetic field (red line) with a non-zero minimum.

### 2.6.1 Magnetic traps for rubidium and cesium atoms

In the experiments that follow we are assuming that the magnetic moment of the atom follows the direction of the external field  $\vec{B}$  adiabatically, such that the condition

$$\omega_L \gg |dB/dt|/B, \quad (2.10)$$

is satisfied, where  $\omega_L \mu B/\hbar$  is the Larmor frequency, and  $\mu$  is the magnetic dipole moment of the atom.

The effective potential is then a function of the modulus of the field, and the projection of the total angular momentum on the field axis:

$$V(\vec{r}) = -\vec{\mu} \cdot \vec{B}(\vec{r}) = g_F m_F \mu_B B(\vec{r}) \quad (2.11)$$

where  $g_F$  is the Landé factor and  $\mu_B$  the Bohr magneton.

Simultaneous transfer of the two species into an effective potential has been performed for two trap configurations (figure 2.7):

For a magnetic trap in the anti-Helmholtz coil configuration, a quadrupole field results whose magnitude increases linearly from the center in all directions

$$\vec{B}(\vec{r}) = \zeta \begin{pmatrix} x \\ y \\ -2z \end{pmatrix} \quad (2.12)$$

where  $\zeta$ , the magnetic field gradient, is constant. In our experiment,  $\zeta/I_{coil} = (6.27 \pm 0.02) \text{ G cm}^{-1} \text{ A}^{-1}$  [60], where  $I_{coil}$  is the current through the coil system. Eq. 2.12 gives rise to a linear trapping potential  $V_{Quad}$ , which can be written as

$$V_{Quad}(\rho, z) = \mu\zeta\sqrt{\rho^2 + 4z^2}. \quad (2.13)$$

In the Ioffe trap configuration, the potential  $V_{quad}$  at  $I_{coil} = 25.6 \text{ A}$  is modified by the superposition of a dipole field, resulting in an anisotropic harmonic potential:

$$V_{Ioffe}(\rho, z) = \frac{1}{2}m(\omega_\rho^2\rho^2 + \omega_z^2z^2) + \mu B_0 \quad (2.14)$$

where  $m$  is the mass of the atom,  $\omega_\rho$  and  $\omega_z$  are the trap frequencies in the radial and axial directions respectively, and  $B_0$  is the magnetic offset field. In comparison to the magneto-optical trap, here we have a potential where the atoms move in pure harmonic motion with no damping. Experimentally we have found that for rubidium atoms, the frequency of oscillation  $\omega_\rho = 2\pi \cdot (271 \pm 2) \text{ Hz}$ ,  $\omega_z = 2\pi \cdot (21.47 \pm 0.06) \text{ Hz}$ , and  $B_0 = (1.300 \pm 0.014) \text{ G}$  [55].

With three coils configured as shown schematically in figure 2.7 it is experimentally possible to gradually deform the magnetic potential from one configuration to the other through moderation of the current flow in the Ioffe coil (Sec. 2.6.3).

## 2.6.2 Loading of atomic mixture into a magnetic trap

The transfer of the atoms from the overlapped MOTs to a quadrupole magnetic potential required the following experimental steps to be carried out for both species simultaneously:

1. MOT compression.
2. Optical molasses
3. Optical pumping

For efficient transfer that as far as possible preserves atom number, temperature, and density, we first decrease the physical size of the MOT so that it is more compatible to the initial magnetic potential. This is accomplished with a two-fold approach. The magnetic gradient is ramped from 6 G/cm to 18 G/cm, and the cooling laser is further detuned from 15 MHz to 20 MHz below resonance.

This is followed by a cooling stage in an optical molasses. The magnetic fields are switched off, and the cooling lasers are still further detuned, to 90 MHz, utilizing the full width of the extended locking range afforded by the DAVLL locking scheme. Although it is not required, in general we employ the same detuning from resonance for both species for the MOT compression and the optical molasses.

For maximum transfer efficiency, atoms are optically pumped into the spin state for the strongest degree of confinement in the magnetic trap. This is the  $|F = 2, m_F = 2\rangle$  state for rubidium and  $|F = 4, m_F = 4\rangle$  for cesium. Typical laser power for optical pumping of cesium are  $\sim 140 \mu\text{W}$  at the  $F = 4 \rightarrow F' = 4$  transition and  $\sim 50 \mu\text{W}$  at the repumping transition ( $F = 34 \rightarrow F' = 4$ ). For rubidium, the corresponding values are  $\sim 130 \mu\text{W}$  at  $F = 2 \rightarrow F' = 2$  and  $\sim 30 \mu\text{W}$  at  $F = 1 \rightarrow F' = 2$  respectively. With these parameters, the transfer efficiency for both species is on the order of 70%.

### 2.6.3 Magnetic trap deformation

In general the spherical quadrupole trap is an intermediate point in the route towards ultracold atomic clouds. Favored as the first recipient of the atomic cloud collected by the MOT because of the spatial similarities between the two potentials, it is nonetheless too prone to losses due to Majorana spin flips, which occur at the magnetic minimum of the quadrupole trap, a region where the adiabatic condition (Eq. 2.10) is not fulfilled.

Therefore a pure quadrupolar potential, although experimentally convenient, constitutes a leaky container at temperatures in the micro-Kelvin regime. We have adopted the solution of a QUIC trap configuration of magnetic coils [58], which allows an initially quadrupolar potential to be adiabatically deformed into an Ioffe potential, which is harmonic in form and everywhere non-zero.

The transition from one trap configuration to another is mediated by the current in the Ioffe coil (figure 2.7), which gradually deforms the potential as illustrated in figure 2.8. The atomic cloud is moved by  $\sim 7.5$  mm in the process, and evolves into an elongated form.

All of the measurements presented here involving atomic mixtures were performed with our group's first magnetic coil system. This system, although functional in essential aspects, produced an Ioffe potential which placed the atomic cloud, at 3.1 mm, undesirably close to the glass wall. As a

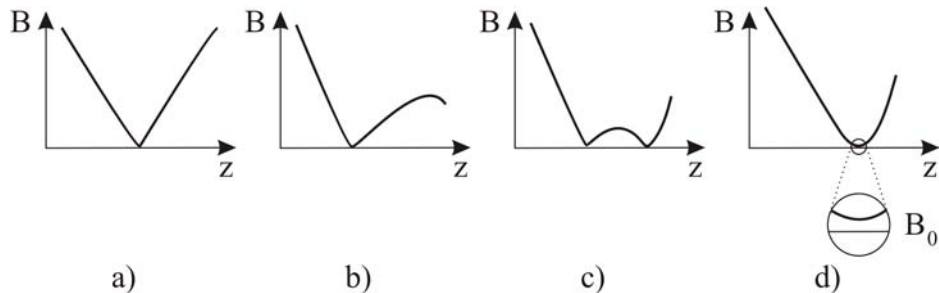


**Figure 2.8:** Schematic diagram of the evolution from the quadrupole (a) to the Ioffe (d) potential as the current through the Ioffe coil is increased. The operation of the Ioffe coil introduces a dipole field with the opposite sign to the quadrupole field (Fig. 2.7), leading to the creation of two minima in the effective potential (b)-(c). Plot (d) depicts the final effective potential, which has a non-zero minima at some offset field  $B_0$  (inset). This minima is  $\sim 7.5$  mm displaced from the minima of the initial quadrupole potential (a).

result, strong atom losses are experienced on transport from the quadrupole to the Ioffe potential. For cesium, we obtain a transfer efficiency of  $\sim 30\%$  into the Ioffe trap. For rubidium, the transfer efficiency was on the order of 20%.

#### 2.6.4 Thermal contact in a magnetic trap

In working with magnetically trapped atomic mixtures, good thermal contact is perhaps the first prerequisite for bringing the mixture into the ultra-cold regime, through the process of *sympathetic cooling*. Here the temperature of one atomic species is deliberately lowered leading to the indirect cooling of another through the collisional transfer of kinetic energy. Unless prevented on energetic grounds or by selection rules, most species collide with each other at a rate which readily leads to efficient cooling and therefore sympathetic cooling can be achieved simply by bringing the atomic clouds into thermal contact, and storing them long enough together for the temperature difference between them to be brought to equilibrium.

The degree of thermal contact between the two clouds in a magnetic trap can be estimated with a sympathetic cooling model from Delannoy *et al.* [63]. Considering only *s*-wave scattering between the target gas (Cs) and its buffer (Rb), the rate of energy exchange can be formulated as  $W = k_B(T_{Cs} - T_{Rb}) \Gamma$ . This rate is characterized by the number of interspecies collisions per unit time,  $\Gamma$ , described as

$$\Gamma = \frac{N_{Cs}N_{Rb}}{\pi^2\rho_x\rho_y\rho_z}\sigma_{Rb,Cs}V \exp\left(-\frac{\Delta^2}{2\rho_z^2}\right) \quad (2.15)$$

where  $N_{Cs}$  and  $N_{Rb}$  are the number of cesium and rubidium atoms respectively,  $\Delta$  is the gravitational sag,  $\sigma_{Rb,Cs}$  is the Rb-Cs elastic cross-section,

$$V = \sqrt{k_B(T_{Cs}/m_{Cs} + T_{Rb}/m_{Rb})} \quad (2.16)$$

is the rms sum of thermal velocities for Cs and Rb, and

$$\rho_i = \sqrt{k_B(T_{Cs}/m_{Cs}\omega_{i,Cs}^2 + T_{Rb}/m_{Rb}\omega_{i,Rb}^2)} \quad (2.17)$$

is the rms sum of the size of the Cs and Rb cloud in the direction  $i = x, y, z$ . The mass of the atom for cesium and rubidium is denoted by  $m_{Cs}$  and  $m_{Rb}$  respectively.

Inspection of Eq. 2.15 indicates that the rate of sympathetic cooling will fall off exponentially with the physical separation of the two clouds due to gravity. As the magnetic moment-to-mass ratio of Rb and Cs, in the  $|F = 2, m_F = 2\rangle$  and  $|F = 4, m_F = 4\rangle$  states respectively differ by 42%, it follows that the magnetic trap cannot support the two clouds equally in the vertical direction. In a harmonic potential, the relative gravitational sag between them is given by

$$\Delta = \frac{g}{\omega_{\rho,Cs}^2} - \frac{g}{\omega_{\rho,Rb}^2} \quad (2.18)$$

where  $g$  is the gravitational constant, and  $\omega_{\rho,Cs}$  and  $\omega_{\rho,Rb}$  are the vertical trap frequencies for cesium and rubidium respectively.

We find that for our trap parameters,  $\Delta \sim 2 \mu\text{m}$ . To calculate  $\Gamma$  explicitly we require the Rb-Cs elastic cross-section, the exact value of which remains not well-known, and whose further determination is a current experimental goal. Regardless of this, for the purpose of discussing gravitational sag it can be seen that  $\Gamma$  decreases as the factor,  $\exp(\Delta^2/(2\rho_z^2))$ . Supposing now for the sake of argument that the two clouds are close to condensation, i.e.  $T_{Cs} = T_{Rb} = 300 \text{ nK}$ , and using the measured values of the trap parameters  $\zeta$  and  $B_0$  (Sec. 2.6.1), we find that for a sag of  $\Delta = 2 \mu\text{m}$ ,  $\Gamma(\Delta = 2\mu\text{m}) = 0.9 \cdot \Gamma(\Delta = 0\mu\text{m})$ .

It has been pointed out [64] that for Cs  $|F = 3, m_F = 3\rangle$  and Rb  $|F = 1, m_F = -1\rangle$  states,  $\mu/m$  would differ by only 2%, thus resulting in almost complete overlap between the atomic clouds even in the ultracold regime. However as we have demonstrated, unless the magnetic trap is relatively weak it should be equally feasible to sympathetically cool the cesium cloud to degeneracy via the maximally stretched states, since the collision rate between the buffer and the target will be reduced by only 10% as a result of incomplete overlap.

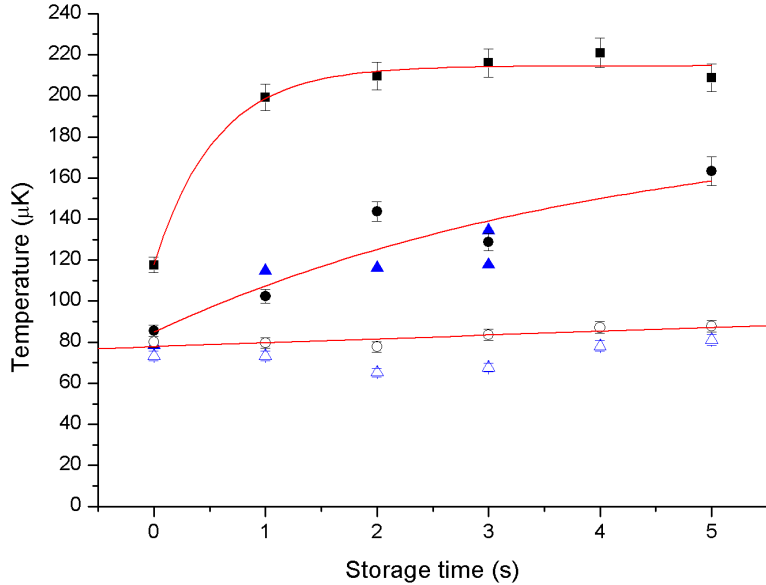


**Figure 2.9:** The temperature of clouds of Rb and Cs simultaneously loaded into a quadrupole magnetic trap, as a function of storage time. The temperature of the Rb cloud is denoted by filled squares. Circles and triangles refer to the temperature of the Cs cloud obtained from time-of-flight expansion in the  $x$ - and  $y$ - directions, respectively. Filled symbols refer to Cs trapped with Rb, open symbols to Cs trapped alone without Rb. Information concerning the fitting functions can be found in the text.

### 2.6.5 Experimental realization of re-thermalization

In the following experiment, we seek to observe re-thermalization of cesium and rubidium in a magnetic trap, by deliberately impressing a temperature gradient between the two gases through optical molasses (Sec. 2.6.2).

To accomplish this, we propose to shift the frequency of the optical molasses for the rubidium cloud from 90 MHz to 30 MHz below resonance during its transfer into the magnetic trap. The loading of cesium atoms occurs simultaneously and remains unchanged. As a result the two clouds are brought together into the quadrupole potential with different initial temperatures. To maximize the density and hence the rate of re-thermalization we perform the measurements at the highest possible magnetic field gradient of 150 G/cm, obtained when with a current of 25A through the quadrupole coils.

Clouds of  $4 \times 10^7$  Rb and  $1 \times 10^7$  Cs atoms were loaded into the magnetic trap. Their temperature evolution over 5 s is shown in Figure 2.9. We find that the rubidium atoms experience some initial increase in temperature,

reaching a steady-state value of  $T_{Rb} \sim 200 \mu\text{K}$  in 1 s. In the first instance we will take  $200 \mu\text{K}$  as the lower bound of  $T_{Rb}$ , for reasons examined in greater detail below (Sec. 2.6.5). In the presence of the rubidium buffer, the temperature of the cesium atoms increased asymptotically as

$$T_{Cs}(t) = T_0 + Ae^{-t/\tau} \quad (2.19)$$

where  $T_0 = 190 \pm 30 \mu\text{K}$  and  $\tau = 4.1 \pm 1.9$  s. This can be compared to the temperature evolution of the cesium gas without rubidium, which experiences no change in temperature apart from a comparatively slow heating of  $1.9 \pm 0.6 \mu\text{K/s}$ , as derived from a linear fit.

The temperature range of study accessible with this method is experimentally limited to  $100 - 200 \mu\text{K}$  for rubidium and  $\sim 80 \mu\text{K}$  for cesium. This puts the re-thermalization process in the regime where the collisions are not limited to purely  $s$ -wave contributions. To estimate what other partial waves will also be contributing to the thermalization time in this measurement, we note that in general a partial wave  $l$  only starts to make a significant contribution if the energy of the collision is greater than the energy of its centrifugal barrier,  $E_{threshold}(l)$  [65]

$$E_{threshold}(l) = \frac{\hbar^2 l(l+1)}{2Mb^2} - \frac{C_6}{b^6} \quad (2.20)$$

where

$$b^2 = \left( \frac{6C_6 m}{\hbar^2 l(l+1)} \right), \quad (2.21)$$

$M = (m_{Cs} + m_{Rb})/(m_{Cs}m_{Rb})$  is the reduced mass, and  $C_6$  is the van der Waals coefficient for the Rb-Cs molecular potential. The most recent theoretical calculation of  $C_6$  can be obtained from Ref. [66]. Alternatively, a comparable value has also been experimentally obtained from fluorescence spectroscopy data [67].

Unlike a gas of pure bosons or fermions, for which some partial waves contributions are prohibited, for two distinguishable bosons all partial wave contributions are present. We find a threshold energy of  $E_{threshold}(l=1) = 50 \mu\text{K}$  and  $E_{threshold}(l=2) = 290 \mu\text{K}$  for  $p$ -wave and  $d$ -wave collisions respectively. As below the threshold energy of the centrifugal barrier the probability for a collision partial wave is highly suppressed, we can assume that our measurement would be dominated by  $s$ - and  $p$ -wave collisions.

### Sloshing and other heating effects

As we have demonstrated, the parameters of the laser radiation employed for optical molasses allows us coarse control over the initial temperature gradient between the atomic clouds, and is one point in the experimental

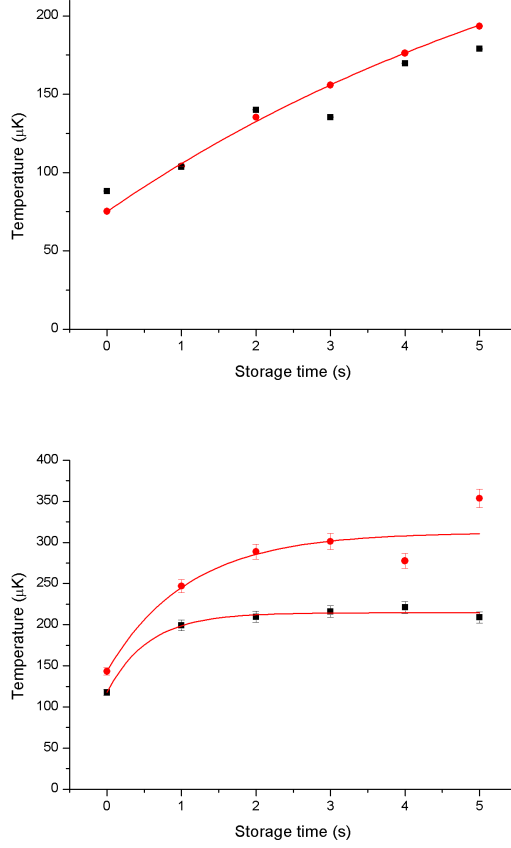


**Figure 2.10:** The temperature of the Rb cloud in the quadrupole trap as a function of time, for an optical molasses prior to loading at 90 MHz (top) and 30 MHz (bottom) below resonance. Black squares and red circles refer to the temperature obtained from time-of-flight expansion in the  $x$ - and  $y$ - directions respectively.

protocol during which the subsequent temperature of the two species in the magnetic potential can be manipulated independently.

However arbitrary adjustment of the optical molasses produces a variation not only in the temperature of the atomic ensemble, but also of its density, which in a conservative potential leads to a change in the coupling parameters and thus possibly to center-of-mass motion of the atomic cloud.

This is illustrated by the set of data in figure 2.10, which shows the temperature evolution of a Rb cloud treated with an optical molasses at the optimized detuning of  $\Delta = 90$  MHz, and, as in the above measurement, at a detuning of  $\Delta = 30$  MHz. The temperature of the cloud in the  $x$ - and  $y$ - direction of expansion are in good agreement in the first case but differ significantly when the detuning of the molasses is reduced. Furthermore this

temperature difference is preserved during the time of observation, indicating that very little thermalization occurs between the vertical and horizontal degrees of freedom of the magnetic potential.

We also note that in both cases the cloud experiences heating, a stubborn effect for which we have no conclusive explanation, although many efforts have been made towards its removal, and a discussion can be found at Ref. [55]. Incidentally our manipulation of the optical molasses also increased the heating rate of the Rb cloud, from a time constant of  $\sim 10$  s to  $\sim 1 - 2$  s.

Therefore to conclude this section, we acknowledge that although it is certainly possible to find evidence for re-thermalization by the technique described, and we have done so, the method is strongly lacking in control. We have shown that, (i), the available temperature range is such that we will have to take into account both  $s$ - and  $p$ -wave contributions, and (ii) by tinkering with the optical molasses to obtain a temperature gradient it becomes no longer possible to optimally couple the atomic cloud from the MOT into the magnetic trap with minimum center-of-mass sloshing.

Clearly we are in need of a more sophisticated method of influencing the temperatures of the atomic clouds independently. This is the topic of the next section.

## 2.7 Species-selective temperature control

The well-known physical tendency of the energies of an ensemble of atoms towards a Boltzmann distribution at equilibrium can be exploited for cooling. When the most energetic atoms of an ensemble are forcibly removed from the population, the remaining atoms will through collisions naturally reassume a distribution of energies with a lower average temperature.

Experimentally, the isotropic and conservative nature of a magnetic trap ensures that atoms with higher energies have a higher probability to be found further from the center of the potential than colder atoms. Therefore, systematically reducing the potential depth modifies the atomic population such that the average temperature of the ensemble is gradually and deliberately lowered.

The design of an evaporative cooling scheme can be conceptually visualized as optimizing the temporal evolution of  $\eta$ , the relation between the chosen trap depth, and the temperature of the atomic ensemble:

$$\eta = E_{trap}/k_B T \quad (2.22)$$

where  $E_{trap}$  is the potential depth, and  $T$  is the temperature of the ensemble. We seek to find a path for  $\eta$  which would remove the largest amount of kinetic energy from the system, at the expense of the smallest number of lost atoms. In any real system atoms will be lost not only as a direct result of

the evaporative process itself, but also due to inelastic background collisions. Taking all loss processes into account, the net efficiency at each evaporative step is given by

$$\alpha = \frac{\ln(T'/T)}{\ln(N'/N)} \quad (2.23)$$

where  $T' = T + \Delta T$  and  $N' = N + \Delta N$ , where  $\Delta T$  and  $\Delta N$  are the stepwise change in the temperature and atom number, respectively. Maximizing the value of  $\alpha$  at each discrete time step of the experiment is equivalent to finding the highest efficiency obtainable within a determined period of time.

As evaporative cooling proceeds, two further parameters can be used to gauge its progress. The phase space density,

$$D = n\lambda_{dB}^3 = n\sqrt{\frac{2\pi\hbar^2}{mk_B T}} \quad (2.24)$$

where  $n = N/V$  is the particle density, is the quantity which most closely reflects the status of the atomic sample with respect to Bose-condensation (Sec. 2.8.1).

Secondly, a sustained increase in the elastic collision rate,

$$\gamma_{elastic} = n\bar{v}\sigma \quad (2.25)$$

where  $\bar{v} \propto \sqrt{T}$  is the average velocity, indicates that the cooling process is entering the runaway evaporation regime. Although not strictly required for the achievement of Bose-condensation, this is nonetheless often the target of an evaporative cooling scheme, as it signifies that the elastic collision rate is not only maintained despite continuous atom losses but increased.

Successful evaporative cooling of one species is also required for sympathetic cooling. Although evaporative cooling can be very efficient, cooling sympathetically is a complementary approach which is widely favored when one of the atomic species should not, or could not, be cooled directly. Some of the most likely scenarios where this would be the case are: (a) when the intra-species collisional cross section of the atomic element in question is small (e.g. lithium-7) or forbidden in the first order (e.g. fermions); (b) when it is advantageous to deliberately use one species as a buffer gas or refrigerant, because, for example, it is technically possible to collect with relative ease a large number of atoms of one species relative to the other.

Evaporative cooling is commonly implemented through radiative evaporation, a general technique using a radiative field to transfer atoms from a trapped to an untrapped state in an energy selective way. It involves no modification of the static magnetic trapping fields as the escape rate is independently controlled by the amplitude and frequency of the applied radiation. A brief coverage of conventional RF-radiative evaporation follows,

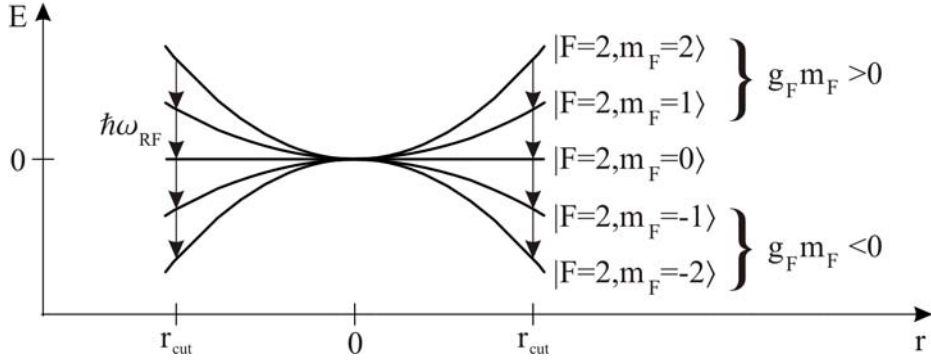


**Figure 2.11:** RF-evaporative cooling of Rb atoms in a harmonic potential.

which provides the necessary background to introduce the concepts of hyperfine evaporative cooling, which, unlike its more familiar counterpart, is species-selective.

### 2.7.1 RF evaporative cooling

In the limit of a weak magnetic field, the Zeeman shift is linear and radio-frequency induced evaporation between  $|F, m_F\rangle$  and  $|F, m_F - 1\rangle$  states induces spin flips of atoms with a potential energy difference of

$$g_F(m_F - (m_F - 1))\mu_B B(\vec{x}) = \hbar\omega_{rf} \quad (2.26)$$

where  $B(\vec{x})$  is the modulus of the instantaneous local magnetic field,  $\mu_B$  is Bohr's magneton and  $g_F$  is the Lande  $g$ -factor. For harmonically trapped Rb atoms in the hyperfine state  $|F = 2, m_F = 2\rangle$ , these resonances allow the trapped atom to enter an anti-trapping state with  $m_F = 0, -1, -2$ , as depicted in Fig. 2.11. Such atoms are expelled from the trap.

Systematically decreasing the RF-frequency  $\omega_{rf}$  decreases in proportion the radius of the surface where the resonance condition is fulfilled, in effect lowering the trap depth  $E_{trap}$  such that the hottest atoms are allowed to escape.

The position of the RF-knife depends on the atomic Zeeman-sublevel spacing of different species. For example, for a mixture of Rb and Cs atoms the different Lande  $g$ -factors of the hyperfine states,  $g_f=1/2$  and  $g_f=1/4$  respectively. Therefore for the same resonance condition  $\hbar\omega_{rf}$ , the resonant shell for Cs will be at twice the magnetic field magnitude  $B(\vec{x})$  as for Rb. In other words in a Rb-Cs mixture, the RF-evaporative cooling of Rb has no direct effect on the Cs temperature, or conversely, high energy Cs atoms cannot be removed without the simultaneous and often undesired removal of a significantly colder fraction of the Rb population.

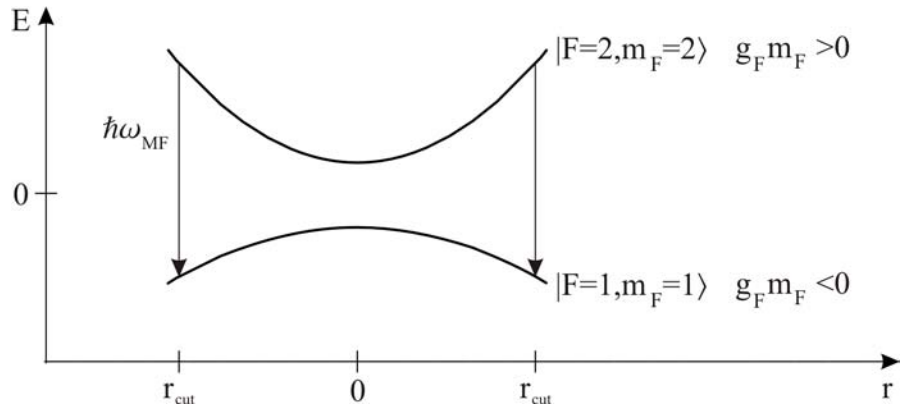


**Figure 2.12:** Hyperfine evaporative cooling of Rb atoms in a harmonic potential.

### 2.7.2 Hyperfine evaporation at microwave frequencies

Microwave evaporation uses transitions between Zeeman sublevels belonging to different hyperfine levels of the ground states. For the case of a Rb atom, depicted in Fig. 2.12, where the transition occurs between states  $|F, m_F\rangle$  and  $|F - 1, m_F - 1\rangle$ , we have

$$\hbar\omega_0 + g_F(F \cdot m_F - (F - 1) \cdot (m_F - 1))\mu_B B(\vec{x}) = \hbar\omega_{microwave} \quad (2.27)$$

where  $\omega_0$  is the hyperfine splitting ( $\sim 2\pi \times 9.2$  GHz for Cs and  $\sim 2\pi \times 6.8$  GHz for Rb). The large difference in these frequencies makes hyperfine evaporation a species-selective process.

Comparing the schemes depicted in figures 2.11 and 2.12, it becomes clear that in RF-evaporation, resonant radiation addresses all of the trapped  $m_F$  states for a particular hyperfine state  $F$ , whereas microwave-evaporation addresses only one Zeeman trapping state. Therefore, unlike RF-evaporation, hyperfine evaporation does not empty all Zeeman sublevels of hot atoms. When there has been incomplete optical pumping or processes which otherwise populate the trapped states not directly addressed by the microwave field, a population of trapped atoms in another  $m_F$  level results which can only be cooled indirectly by sympathetic cooling, thus lowering the overall efficiency of the evaporative process.

#### Microwave-field dressed potentials

We note here that as a result of the specified output power of the microwave field (Sec. 2.7.3), the experiments that follow are performed in the strong coupling regime. This produces a dressed trapping potential which has the following properties.

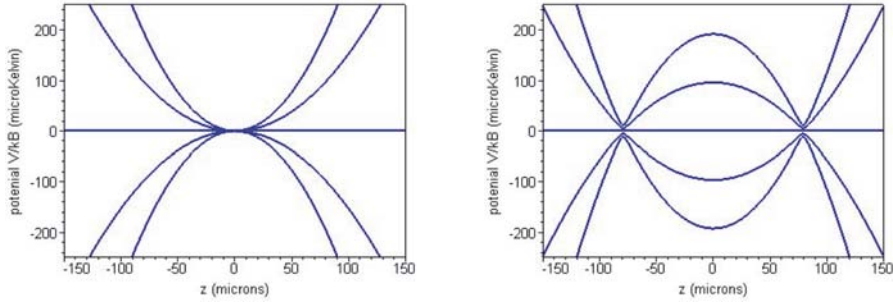


**Figure 2.13:** Calculated bare (left) and dressed (right) state potentials along the  $z$ -axis for the Ioffe trap configuration. In the bare potential picture the upper to lower curves depict the eigenstates for  $m_F = 2, 1, 0, -1, -2$  respectively. In the dressed potential picture the lowermost potential is used for evaporative cooling. The microwave field parameters used are  $\Delta/2\pi = 1$  MHz and  $\Omega/2\pi = 60$  kHz. Further details are given in the text.

The dressing of the bare potential  $V_{trap}$  by the electromagnetic field  $B_{rf} \cos(\omega_{rf}t)$  can be described by

$$V(\vec{r}) = m_F \sqrt{[V_{trap}(\vec{r}) - \hbar\Delta]^2 + [\hbar\Omega]^2} \quad (2.28)$$

where  $\Delta$  is the rf detuning,

$$\Omega = g_F \mu_B B_{rf} / 2\hbar \quad (2.29)$$

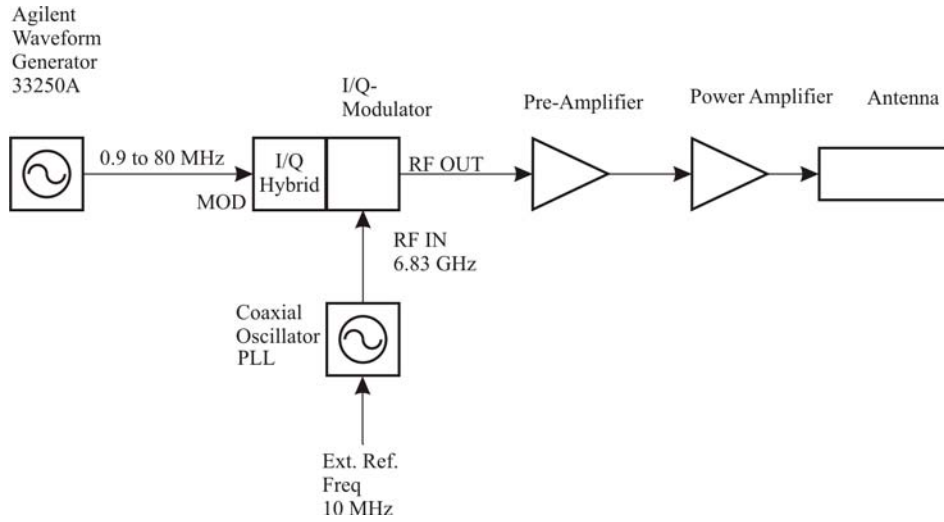
is the Rabi frequency,  $g_F = 1/2$  for rubidium atoms in the  $F=2$  state, and  $\mu_B$  is the Bohr magneton.

Figure 2.13 illustrates the modification of bare magnetic Zeeman eigenstates by the microwave field. The trapping potential  $V_{trap}(\vec{r})$  is in this case an Ioffe potential, given by equation 2.14. We will assume for simplicity that the microwave antenna behaves as a dipole emitter, with an estimated output power of 9 W and located 2-3 cm from the atomic cloud. Then we find that  $\Omega = 40 - 60$  kHz. In this picture, radiative evaporative cooling can then be understood as a gradual shifting of the resonance in the lowest dressed potential in figure 2.13 towards the center of the trap, thus making the trapping potential increasingly shallow.

Further experiments with microwave-field dressed states are described in Appendix C.

### 2.7.3 Implementation of a modular microwave source

In this section the technical details of a microwave system with a sweepable frequency range near 6.83 GHz for hyperfine evaporative cooling of rubidium is described. We require a system which can be ramped over a range of



**Figure 2.14:** Schematic diagram of microwave system at 6.83 GHz for hyperfine evaporative cooling.

6.830 GHz $\pm$ 1 – 80 MHz in a time period of  $\sim$  100s. Instead of installing a commercial microwave generator, we have chosen a modular approach which up-converts the existing radio-frequency knife by 6.83 GHz. This allows us to retain all the equipment dedicated to RF evaporative cooling in our new system. In addition this also ensured that our microwave system has the same resolution and sweepable range as our RF system.

Figure 2.14 is a schematic diagram of our solution. On the far left, a modulation frequency of 1-80 MHz is generated by the identical frequency generator (Model 33250A, manufactured by Agilent) used for RF evaporative cooling. It is frequency modulated by a second device (Agilent 33120A, not shown), to which the evaporative cooling ramp can be transmitted as a waveform via a GPIB (General Purpose Interface Bus) connection from the computer by the master experimental control program. Thus pre-programmed, the stored waveform can be digitally triggered with a standard experimental sequence command.

The local oscillator frequency is generated by a high-Q phase-locked loop coaxial resonator (Model BCO-010-06830-05, manufactured by Miteq) operating at a fixed frequency of 6.830 GHz at +13 dBm. It is stabilized by a phase-locked loop to an external reference frequency of 10 MHz at +10 dBm, provided in our case by a rubidium frequency standard (Model PRS10, manufactured by Stanford Research Systems).

The two input frequencies are brought together at a custom-made single sideband (SSB) up-converter (Model SM0408G21P, manufactured by Miteq). This device separates the incoming signals into in-phase and quadrature ( $0^\circ$  and  $90^\circ$ ) components, then sums components of one phase while rejecting the other to produce an asymmetric output. In our case this results

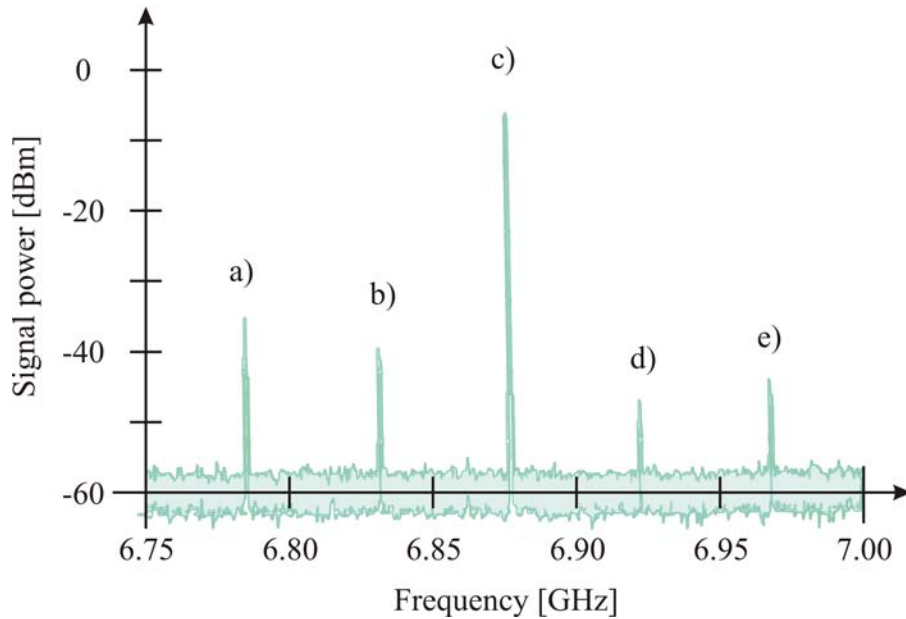


**Figure 2.15:** Spectral output of the microwave system for hyperfine evaporative cooling. Peaks (a)-(d) refer to the lower sideband, the carrier, the upper sideband, and the first and second harmonics respectively.

in most of the power being carried by the upper sideband, with the lower sideband strongly suppressed to similar levels as the carrier itself. For the purpose of evaporative cooling this means that most of the output of the system is of the desired frequency, which would not be the case if a standard 1 : 1 mixer is employed.

In addition the digital mixer is configured in a carrier-driven mode, meaning that the carrier frequency is used to switch on the semiconductors within the device. Using the carrier frequency instead of the modulation or IF frequency to drive the mixer allows an improved suppression of harmonics of the modulation signal. For our purposes this is preferable as harmonics of 0-80 MHz is considerably more disturbing to the physical system than harmonics of 6.83 GHz.

From the specifications of the device we estimate that, for an initial carrier frequency at a power of +10 dBm and a modulation/IF frequency at 0 dBm, the upper sideband will experience an insertion loss of 7 dB, while the carrier and lower sideband will be suppressed by -27 dB and -25 dB respectively with respect to the upper sideband.

The output of the mixer is amplified by a series of two amplifiers. A pre-amplifier (Model AMF-3B-040080-25-25P, manufactured by Miteq) takes the signal power to 10 dBm (10 mW), and is followed by a power amplifier (Model KU684XL, manufactured by Kuhne), which brings the typical output power to 39 dBm (8 W typical, 10 W maximum).

As the atoms will be in the near-field of the antenna, it is difficult to find the most effective type of antenna through calculation. However from experiences with microwave addressing of single atoms it appears that one of the most effective microwave antenna is a straight rectangular waveguide with a coaxial adapter, and this is what is used here [68].

Figure 2.15 shows the spectral output of the entire system, obtained with a pick-up coil close to the opening of the waveguide. We find that relative to the upper sideband, the carrier and lower sideband are suppressed by -33 dB and -29 dB, respectively. Second- and higher-order harmonics are suppressed to the  $\sim -40$  dB level. The noise floor is at about -50 dB in relation to the desired signal.

These characteristics are sufficiently close to our estimated specifications for us to expect the system to function as designed. Therefore after preliminary demonstrations with magnetically trapped atoms in the quadrupole potential we began the production of ultracold atomic clouds through hyperfine evaporative cooling in the Ioffe trap.

## 2.8 Quantum degeneracy and three-body collisions

As we evaporatively cool down to lower and lower temperatures we eventually arrive into the quantum degenerate regime. Here collisions between atoms play an important role in determining the collective behavior of the atomic ensemble. Furthermore, the atomic density in this regime is significantly higher than at room temperature allowing the possibility of three atoms approaching and colliding with each other to become a measurable effect.

In this section we first introduce the properties of the atomic cloud at ultracold temperatures, in order to take into account that these properties are qualitatively different from any so far documented in this chapter. In particular the high densities achieved via further cooling raises the importance of a loss mechanism which we have hereto been able to ignore. We explore the three-body collision rate in a pure rubidium condensate and from this and the previous knowledge acquired provide an outlook into what might possibly be expected in a cesium-doped rubidium condensate.

### 2.8.1 Bose-Einstein Condensation

At some point in the cooling process the de Broglie wavelength of the atoms starts to become comparable to the interparticle distance. For particles with integer spin, further cooling at constant particle density will take the sample pass a critical ratio, expressible as

$$n\Lambda_{dB}^3 = 2.612 \quad (2.30)$$

where  $n$  is the particle density, and

$$\Lambda_{dB}(T) = \sqrt{\frac{2\pi\hbar^2}{mk_B T}} \quad (2.31)$$

is the de Broglie wavelength.

At this point the ground state of the atoms becomes macroscopically occupied, an effect that is possible to grasp by considering the Bose-Einstein distribution

$$n_i = \frac{1}{\exp\left(\frac{\epsilon_i - \mu}{k_B T}\right) - 1} \quad (2.32)$$

where  $n_i$  is the average number of particles occupying a state  $i$  of energy  $\epsilon_i$  and  $\mu$  is the chemical potential. Inspection shows that as  $\mu \rightarrow \epsilon_0$ , the exponential term approaches unity for  $i = 0$ , or in other words the occupation of the ground state  $n_0$  diverges.

Bose-Einstein condensation occurs at a critical temperature  $T_c$  which is dependent on the confining potential. For our cylindrical symmetry harmonic trap,

$$T_c \approx \frac{0.94\hbar(N_{tot}\omega_\rho^2\omega_z)^{1/3}}{k_B} \quad (2.33)$$

where  $N_{tot}$  is the total atom number [69].

In the next chapter we will examine the mean-field approximation of a BEC, represented by the Gross-Pitaevski description, more closely, in particular in the creation of non-linear matter-wave effects. In the first instance we want here to understand enough of the properties of the condensate to understand the experimental data. For this the Thomas-Fermi approximation of mean-field theory will suffice.

### The Thomas-Fermi approximation

A useful approximate description of the condensate is to neglect the kinetic energy term in the Gross-Pitaevski or non-linear Schrödinger equation, the time-independent version of which can be written as

$$\left(-\frac{\hbar^2\nabla^2}{2m} + U_{ext}(\vec{r}) + U_0|\psi(\vec{r}, t)|^2\right)\psi(\vec{r}) = \mu\psi(\vec{r}) \quad (2.34)$$

where  $U_{ext}$  is the external trapping potential,  $\mu$  is the chemical potential,

$$U_0 = \frac{4\pi\hbar^2 a}{m}, \quad (2.35)$$

and  $a$  is the scattering length.

For the experimental parameters we consider here, it is often justifiable to assume that the condensate wave function is dominated by its interaction energy. Inserting into Eq. 2.34 the approximation  $U_0|\psi(\vec{r}, t)|^2 \gg \hbar^2\nabla^2/2m$ , we find

$$[U_{ext}(\vec{r}) + U_0|\psi(\vec{r})|^2]\psi(\vec{r}) = \mu\psi(\vec{r}). \quad (2.36)$$

This allows a density profile for the condensate to be deduced which is accurate over the body of the condensate but deviates at the edges,

$$n(\vec{r}) = \psi^2(\vec{r}) = \begin{cases} \frac{\mu - U_{ext}(\vec{r})}{U_0} & \text{for } \mu - U_{ext}(\vec{r}) > 0, \\ 0 & \text{otherwise.} \end{cases} \quad (2.37)$$

from which a parabolic fit function for the condensed fraction of the atomic cloud can be obtained.

In the next section (Sec. 2.8.2), the number of atoms remaining in the Bose-condensate as a function of storage time is used to determine the three-body collisional loss rate. Rubidium atoms trapped in an Ioffe potential were Bose-condensed by the application of microwave knife addressing the  $|F = 2, m_F = 2\rangle \rightarrow |F = 1, m_F = 1\rangle$  transition, producing condensates containing on average  $5 \times 10^4$  atoms.

Figure 2.16 shows the typical absorption image obtained, as well as a cut through the center of the cloud. Compared to the inverted parabola expected in the Thomas-Fermi limit, the profile exhibits bimodal characteristics, indicating that the atomic cloud is not a pure Bose-condensate at the experimental parameters used in these measurements. Instead a fraction of the atomic population remains a thermal gas, describable by a classical Boltzmann distribution. The complete fitting function for the partially condensed cloud would therefore be the sum of a Gaussian and a Thomas-Fermi parabolic function, describing respectively the thermal and condensate fractions (Fig. 2.16, bottom).

From the fitting parameters, the number of atoms in the condensate and thermal fractions,  $N$  and  $N_{th}$ , can be obtained through the relations

$$N = (2\pi/5)n_0 \frac{w_{TF,\rho} w_{TF,z}}{\sigma} \quad (2.38)$$

and

$$N_{th} = 1.89n_{th} \frac{w_{th,\rho} w_{th,z}}{\sigma} \quad (2.39)$$

where  $n_0$  is the measured peak optical density due to the condensate component,  $w_{TF,\rho}$  and  $w_{TF,z}$  are the Thomas-Fermi radii of the condensed fraction in the directions  $(\rho, z)$ ,  $n_{th}$  is the measured peak optical density due to the thermal component, and  $w_{th,\rho}$  and  $w_{th,z}$  are the  $1/e^2$  radii of the thermal fraction. The absorption cross section is denoted by  $\sigma$ .

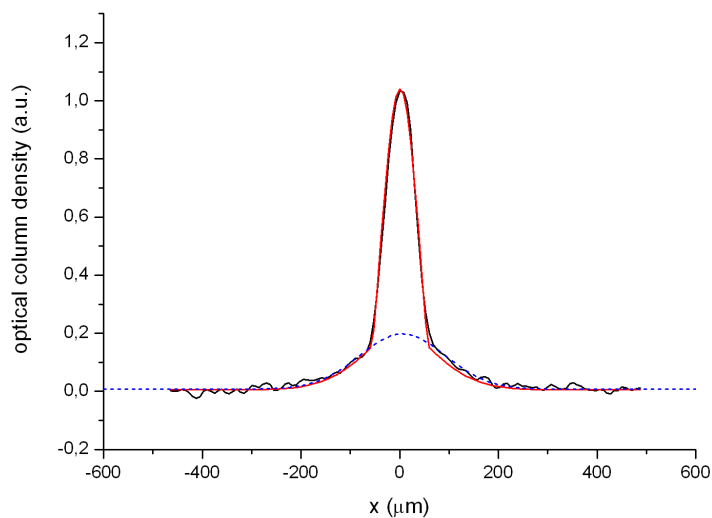
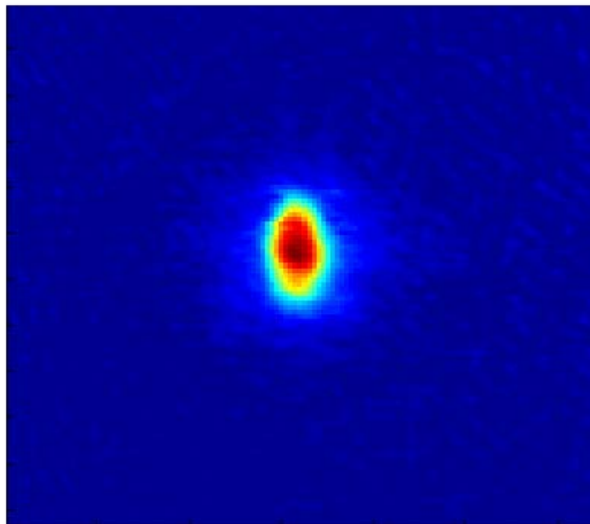


**Figure 2.16:** Absorption image of a partially Bose-condensed atomic cloud (top), at 25 ms of time-of-flight expansion, and a cut through the center of the imaged cloud (bottom). The experimental data (black) is fitted with the sum of a Gaussian and a Thomas-Fermi density distribution function (red), allowing the number of atoms in the condensed and thermal components to be determined through Equations 2.38 and 2.39, respectively. The fitted Gaussian distribution denoting the underlying thermal population is denoted by a dotted line (blue).

Applying this analysis to the atomic cloud in Fig. 2.16, we find that the condensate fraction makes up 55% of the total atom number; the other 45% are from thermal atoms. Averaging over all such measurements of initial atom number, we obtain a mean value of  $N/N_{tot} = 0.65$ .

### 2.8.2 Trap loss through three-body recombination

In three-body recombination, two atoms form a bound state whose binding energy is removed by a third atom. Experimentally this usually results in the loss of all three atoms from the trap.

Theoretically, it has been found that the three-body loss rate constant  $L_3$  can be parameterized in terms of the two-body scattering length  $a$ , and that in many cases,  $L_3 \sim a^4$ . Why this should be so can in the first instance be understood in terms of a qualitative argument from Fedichev *et al.* [70], which is valid when  $a$  is large and positive. However as this condition is not well-fulfilled for the rubidium atom, we will subsequently introduce a numerical model from Esry *et al.*, which is valid for all values of  $a$ .

The two-body scattering length can be written in terms of the binding energy of the diatomic molecule as

$$a = \hbar/\sqrt{m\epsilon_0} \quad (2.40)$$

where  $m$  is the atom mass and  $\epsilon_0$  is the binding energy.

In an elastic three-body interaction the binding energy of two atoms is carried away by the third atom, therefore  $\epsilon_0 \sim \hbar^2 k_f^2/m$ , where  $k_f$  is the final momentum of the third atom relative to the center-of-mass of the molecule. Substituting Eq. 2.40 into this expression gives  $k_f \sim 1/a$ .

As a first approximation, we can assume that the probability for a three-body collision is found by combining the probability of (i) a pair collision, and (ii), a third atom being found inside of sphere of radius  $l \sim a$  around the colliding pair, which we can describe with the weighting factor  $w \sim nl^3$ , where  $n$  is the gas density.

Then the number of recombination events per unit time and per unit volume can be estimated as  $n^2\sigma vw$ , where  $\sigma = 8\pi a^2$  is the two-body collisional cross section, and  $v \sim \hbar k_f/m$  is the relative velocity of the third atom to the other two, where we have assumed that the interaction potential created by the weakly bound pair is much greater than the initial kinetic energies of all three atoms. Putting all this together gives  $L_3 \propto 8\pi\hbar a^4/m$ . A more rigorous derivation yielded the expression [70]:

$$L_3 \simeq 11.4 \frac{\hbar}{m} a^4, \quad (2.41)$$

Subsequent experimental determination of the three-body loss rate of various species have in some cases agreed with the prediction given by Eq. 2.41 [71], but it has also at times been found to be too small [72, 73].

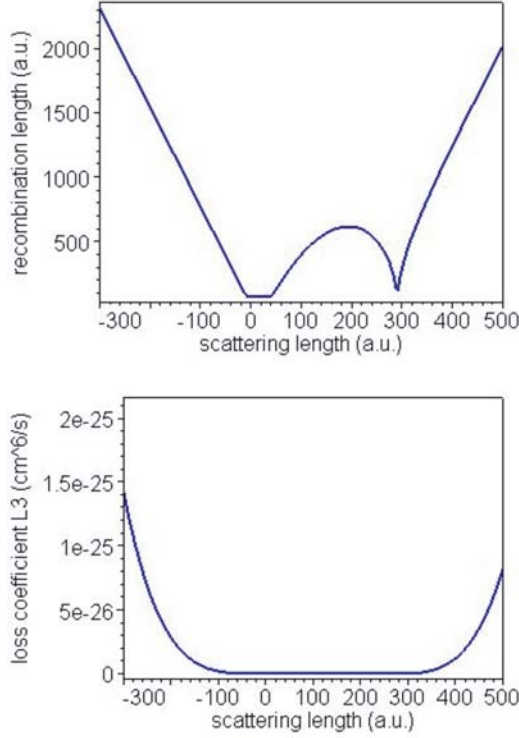


**Figure 2.17:** The theoretically predicted recombination length  $\mathcal{R}_3$  at zero temperature as a function of the two-body scattering length  $a$ , for the constant  $r_0 = 18.8$  a.u. (top). The corresponding predicted loss coefficient  $L_3$  as a function of scattering length (bottom). The two curves are related to one another by Eq. 2.42.

For the rubidium atom in the stretched state, the best agreement between experiment [73] and theory has come from the model of Esry *et al.* [74], who proposed a universal curve which predicts  $L_3$  for all values of  $a$ .

Through examining the results of a large number of numerical calculations for different atomic species, Esry *et al.* derived an analytical expression for the loss rate which is species-independent, based on a parameter  $\mathcal{R}_3$ , which can be directly related to  $L_3$ , but does not depend on most atomic properties except for the scattering length:

$$\mathcal{R}_3 = \left( \frac{2\mu}{\hbar} L_3 \right)^{1/4}, \quad (2.42)$$

where  $\mu = \sqrt{m_1 m_2 m_3 / (m_1 + m_2 + m_3)}$  is the reduced mass.

The universal relationship they obtained between  $\mathcal{R}_3$  and  $a$  is a relatively simple piecewise function given by:

$$\mathcal{R}_3 \simeq \max \begin{cases} 5.0(a - \frac{3}{2}r_0)[2 \sin^2(\ln \frac{3a}{2r_0})]^{1/4}, & \text{for } a > 0, \\ -7.7a, & \text{for } a < 0, \\ 4r_0. \end{cases} \quad (2.43)$$

where  $r_0$  is a free parameter between 1-20 a.u..

Figure 2.17 is a plot of  $\mathcal{R}_3$  and  $L_3$  as a function of  $a$ . The best-fit value for  $r_0$  is determined by comparing the analytical description above with the results of full-scale numerical calculations; for rubidium, this gives  $r_0 = 18.8$  a.u.. Using this model, we find that for the rubidium scattering length of  $100a_0$  [115], Eq. 2.43 gives a prediction of  $L_3 = 2.10 \times 10^{-29}$  cm<sup>6</sup>/s and  $L_3 = 1.26 \times 10^{-28}$  cm<sup>6</sup>/s for rubidium atoms in the  $F = 2, m_F = 2$  state in a condensate and a thermal cloud, respectively. The existence of a factor of 6 between the two loss rates is explained in the next section.

Experimentally this universal dependence of the three-body loss rate on scattering length has ramifications for the use of Feshbach resonances, since at the large values of  $a$  near such a resonance the three-body losses increases as  $a^4$ . In addition for the case of bosonic mixtures we note that D'Incao and Esry have recently derived universal scaling laws for two identical and one non-identical boson, i.e. a three-body collision of the form  $B + B + B'$ , and found that the behavior of  $L_3$  is similarly dominated by  $a^4$  [78].

This strongly suggests that the three-body loss rate involving rubidium and cesium atoms in our experiment will be significant at higher densities, particularly given the large positive Rb-Cs scattering length recently estimated by Anderlini *et al.* [75]. By fitting the results of a re-thermalization experiment to four sets of theoretical predictions from Jamieson *et al.* [76], Anderlini *et al.* came to a most probable value of  $a = 595a_0$ , which is almost a factor of 6 greater than the Rb-Rb scattering length.

### Three-body collisions and coherence

The subject of coherence in matter-waves can be made familiar by borrowing concepts from the behavior of photons, which are bosons of spin-1 and zero rest mass. By taking such a quantum optics viewpoint, we find that the measurement of the rate of three-body collisions in an atomic cloud of bosons can be interpreted as equivalent to measuring its degree of third-order coherence.

First we note that for both laser beams and Bose-condensates, the presence of first-order coherence can be deduced by the appearance of interference fringes when parts of the bosonic system is separated and recombined with itself. This is because by definition, first-order coherence implies that knowing the phase of the light- or matter-wave at one point in space and time allows the phase at any other point to be determined.

Furthermore, beams of photons also exhibit higher-order coherence in the form of intensity correlations. As the matter-wave equivalent of intensity in a laser beam is density, we expect the density and hence collisional probability of a thermal gas and condensate to differ, just as the photon statistics of an incoherent source and a laser beam exhibits bunching and anti-bunching behavior respectively. For two-boson correlations, for example, the correlation function  $g^{(2)}(0)$  for thermal photons or atoms is a factor of  $2!$  greater than for photons from a coherent source or condensed atoms.

This being the case, Kagan *et al.* suggested ten years before the experimental realization of BEC that one signature of the phase transition would be a decrease in the three-body loss rate by a factor of 6 [77]. It was pointed out that as a result of the third order coherence of the condensate, the probability of finding three condensed bosons close together is suppressed with respect to a thermal cloud by a factor of  $g_{th}^{(3)}(0)/g_c^{(3)}(0) = 3!$ , which would be experimentally observable as a corresponding decrease in the measured value of  $L_3$ .

### Experimental investigations

To obtain an estimate for  $L_3$ , condensates of rubidium were produced through hyperfine evaporative cooling, and the number of atoms remaining after storage times of up to  $t = 2$  s were determined by fitting absorption image cross-sections for the condensate and thermal fractions, as described in Sec. 2.8.1.

As noted previously, this analysis shows that at  $t = 0$  s the condensate fraction makes up about 65% of the total number of atoms, a feature of the data which we can use to obtain qualitative evidence of collision suppression and third-order coherence in a BEC. Fig. 2.18 shows the number of atoms remaining after a time  $t$  in the condensed and non-condensed fractions; each point is an average of 5-12 measurements. Fitting both atom fractions with an exponential decay, we obtain time constants of  $\tau_{3,c} = 9.2 \pm 1.3$  s and  $\tau_{3,nc} = 3.83 \pm 0.84$  s for the condensate and thermal cloud, respectively. This gives a statistically significant factor of 2.5 in the ratio of the three-body collision rates, but not 6, as would be expected from bosonic statistics. We note here that a rigorous experimental approach to determining the ratio of the three-body collision rates should ideally be carried out with a cloud of pure thermal atoms and a cloud of almost pure condensate atoms, such as reported in Ref. [71]. Then it was found that it is possible to extract the factor of 6 within the experimental uncertainty. In a partially condensed cloud, however, interactions between the two fractions gives rise to more complicated behavior, as will be discussed in greater detail below.

Treating now only the temporal evolution of the number of atoms in the condensed fraction in Fig. 2.18, we will make an estimate of  $L_3$ , the three-body loss coefficient for the condensate. At high densities, the effect

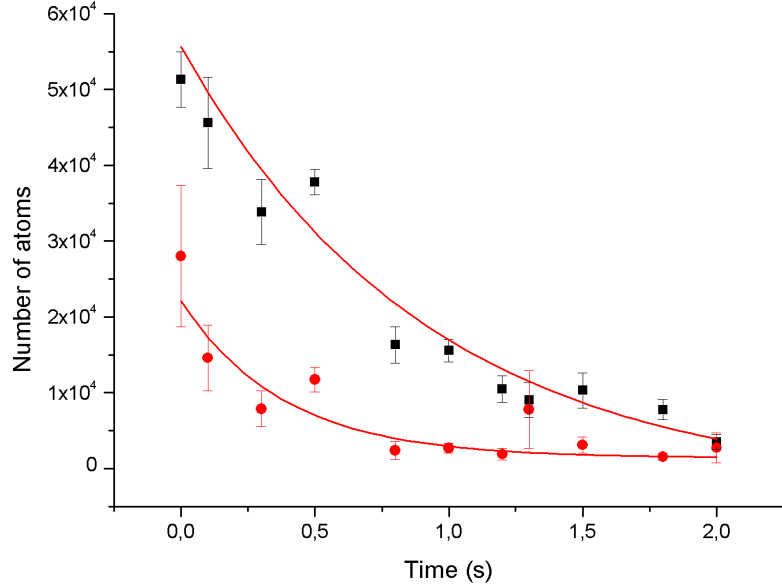


**Figure 2.18:** The number of atoms remaining in the condensate (squares) and non-condensate fraction (circles) as a function of time. The exponential fits yield decay time constants of  $\tau_{3,c} = 9.2 \pm 1.3$  s and  $\tau_{3,nc} = 3.83 \pm 0.84$  s respectively. The roughly factor of 2.5 difference can be attributed to the third-order coherence statistics of the condensate.

of three-body losses can be seen as a deviation of the number of atoms  $N(t)$  as a function of storage time  $t$  from pure exponential decay due to density-independent background collisions [71].

The time constant for background collisions  $\tau_1$  is typically on the scale of 100-200 s, which is an order of magnitude greater than the duration of the present measurement. Therefore as a first approximation, we will neglect the losses due to background collisions in the following analysis. In addition, it has been predicted theoretically and demonstrated experimentally that two-body losses can also be neglected [71, 72].

Then the decay can be described by

$$\frac{dN}{dt} = -L_3 N \langle n^2 \rangle \quad (2.44)$$

where  $L_3$  is the three-body loss rate constant, and the mean squared density  $\langle n^2 \rangle$  is given by

$$\langle n^2 \rangle = \frac{8n_0^2}{21}. \quad (2.45)$$

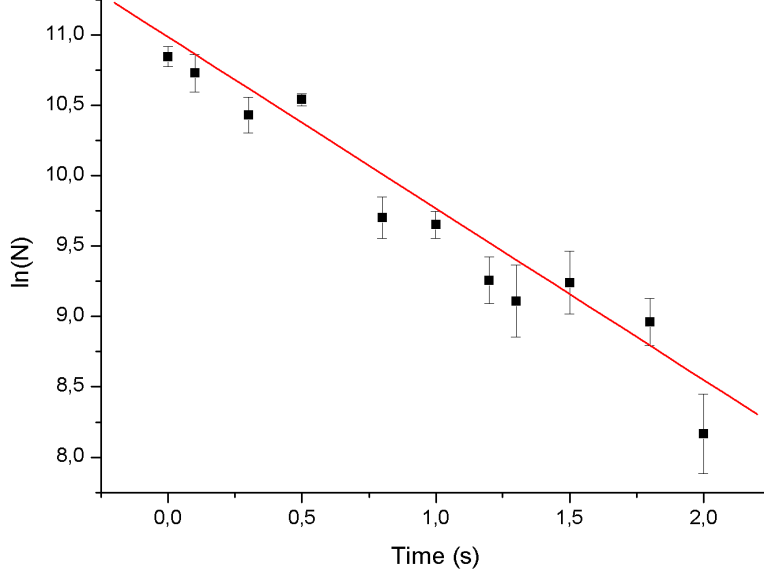


**Figure 2.19:** The natural log of the number of condensate atoms as a function of time. At this short time scale we expect the loss rate to be dominated by the effect of density-dependent collisions.

Here  $n_0$  is the peak density of the condensate. Taking the Thomas-Fermi approximation,  $n_0$  can be written as

$$n_0 = 0.118 \left( \frac{Nm^3\bar{\omega}^3}{\hbar^3 a^{3/2}} \right)^{2/5} \quad (2.46)$$

where  $N$  is the number of atoms in the condensate, and  $\bar{\omega} = (\omega_\rho^2 \omega_z)^{1/3}$  is the geometric mean of the harmonic trap frequencies. This measurement was performed with a new magnetic coil system, with harmonic trap frequencies  $\omega_\rho = 2\pi \cdot (189.5 \pm 1.9)$  Hz and  $\omega_z = 2\pi \cdot (9.9 \pm 0.1)$  Hz respectively.

Results are shown in figure 2.19 as a plot of the natural log of the atom number against time. We note that the linear slope confirms the validity of our assumption that contributions from background gas and two-body collisions may be neglected for a measurement on this time scale. From the gradient of the straight line fit a value of  $L_3 = (2.5 \pm 0.6) \times 10^{-28}$  cm/s is obtained.

Comparison with the universal model described by Eq. 2.43 indicates that our measured value is within a factor of 1.5 of the theoretical prediction for non-condensate atoms, but an order of magnitude greater than the prediction for condensate atoms. With repeated measurements, and the op-

portunity to identify and implement the necessary technical improvements, this difference can most likely be resolved. At this point, however, this remains our sole measurement of the Rb three-body loss rate.

Finally, the simple model based on Eq. 2.44 which we have adopted can be made more accurate by taking into account the effect of the non-condensed fraction, which in our case comprises 20% of the peak density. Atoms in this non-condensed fraction can contribute to the loss rate of condensed atoms through collisions. Therefore, Eq. 2.44 should be re-written as [73]

$$\frac{1}{N} \frac{dN}{dt} = -L_3 \left[ \langle n^2 \rangle + 6 \langle nn_{th} \rangle + 6 \langle n_{th}^2 \rangle \right] \quad (2.47)$$

where  $f(N, T) = \langle n^2 \rangle + 6 \langle nn_{th} \rangle + 6 \langle n_{th}^2 \rangle$  is a function of both atom number and temperature, and contains terms which describe respectively the contribution of three, two, or one condensate atom to the three-body collision.

In summary, we have began an investigation into three-body collisions in our experimental system. Treating in the first instance rubidium in the quantum degenerate regime, we have obtained a first estimate of the three-body loss rate for this species on its own. Furthermore, as a species-selective evaporative technique was employed throughout, the experimental approach and analysis developed in this measurement can be extended to a magnetically trapped mixture of rubidium and cesium atoms, the production of which was described in Sec. 2.6. This would allow three-body collisions between rubidium and cesium to be investigated, for which the rate of trap loss is predicted to be 1000 times larger.

### 2.8.3 Perspectives for future experiments

Experiments on three-body collisions between neutral atoms have become a topic of great interest recently due to the results of several new investigations into three-body effects [79, 80].

In the context of investigating the boundary between single- and many-particle physics, several applications of three-body collisional effects can be proposed.

Firstly, three-body collisional losses may be used to measure the decay of higher-order coherence in a rubidium condensate due to the presence of dopant cesium atoms. Using a mean-field approach, it has been theoretically predicted [81] that when a single impurity is doped into a condensate, it feels and at the same time creates an effective potential around itself. The strength of this coupling is determined by the atom-impurity scattering length. When the coupling is weak, the impurity can be treated as a perturbation to the ground-state wavefunction of the BEC. However there also exists a strong coupling regime for negative scattering lengths where the

attractive interaction between the impurity and the condensate: (i) localizes the impurity such that it is bound to the atom cloud, and (ii), strongly modifies the condensate density and in some cases is sufficient to cause condensate instability and implosion.

Therefore we can speculate that the formation of a density ‘bump’ due to a strongly bound impurity atom is equivalent to creating a local fluctuation in the quantum field of the condensate, which is typically suppressed relative to the incidence of thermal fluctuations, as we have just experimentally demonstrated. The subsequent degradation of higher-order coherence should be observable as an increase in the loss rate of condensate atoms, in this case rubidium, as a function of dopant atom number, with the maximum loss rate being a factor of 6 greater than the loss rate in the initial condensate.

One might also note that random implantation of strongly localized impurities will effectively create a disordered potential. It has been proposed that adding disorder to a superfluid is a way to make a phase transition to a Bose-glass, a state that can be roughly visualized as an amorphous phase somewhere between a superfluid and a Mott-insulator. Aspects of phase evolution in such randomly perturbed condensates were recently investigated in an experiment with an optical speckle potential [82]. A physically equivalent experiment with impurity atoms will be one of the few techniques which would allow the higher-order coherence of such a partially disordered system to be investigated, as directly imaging the density fluctuations will require an imaging technique with very high spatial and temporal resolution.

## 2.9 Conclusion

In this chapter I have described the development of a mixed species ultracold experiment from its beginnings as a single-species Bose-Einstein condensation apparatus. The experimental work began with the installation of laser systems at 852 nm which allow laser cooling and trapping techniques for cesium atoms to be employed. Simultaneous collection of cesium and rubidium in spatially overlapped magneto-optical traps followed, from which we observe the interaction of the two species through light-mediated collisions.

However the inter-species collisional effects which we observe in the MOT is complicated by the presence of near resonant radiation. To investigate the interactions in a more ideal environment, we transferred both atomic clouds simultaneously into a quadrupole magnetic trap. Here we implemented a coarse method of species-selective temperature control. Through manipulation of optical molasses for both species, we were able to imprint a temperature gradient between the two clouds in the magnetic trap. Subsequent re-thermalization can be attributed to  $s$ - and  $p$ -wave scattering. At the same time, the method has several intrinsic drawbacks, including a limited temperature range, and asymmetric heating.

A more sophisticated method of temperature control became a necessity. I described the design and performance of a microwave system at 6.83 GHz, which will allow us to evaporatively cool the rubidium atomic cloud down into the ultracold regime, without inducing losses in cesium atom number. Species-selective evaporative cooling also facilitates the implementation of sympathetic cooling techniques and interspecies re-thermalization experiments, and will be used for the experimental determination of the Rb-Cs scattering length.

Finally, an investigation into three-body recombination was initiated, through the measurement and analysis of three-body losses in a rubidium condensate. As the measurement was performed with the use of species-selective evaporative cooling, an experimental basis for future investigations of inter-species three-body collisions between rubidium and cesium has been developed which, together with the determination of the scattering length, should allow novel investigations into Rb-Cs few-body phenomena.



## Chapter 3

# Bright soliton trains: creation and propagation

### 3.1 Non-linear effects in Bose-Einstein condensates

In the previous chapter we saw that the two-body interaction between atoms, which in the regime dominated by  $s$ -wave collisions is characterized by the scattering length  $a$ , has a great impact on the efficiency of evaporative cooling, the re-thermalization rate of mixtures, and the three-body loss rate.

In the work that follows we demonstrate that in a quantum gas, these interparticle interactions change the shape and size of the condensate, as well as produce non-linear effects, such as matter-wave solitons. To describe these interactions, it is convenient to replace the atom-atom scattering point of view which we have largely used so far with a mean-field treatment of atomic interactions, as follows.

#### 3.1.1 The mean-field description of condensate behavior

We have already introduced the mean-field approach to describing a Bose-Einstein condensate in Chapter 2, an approach that is mathematically expressed by the Gross-Pitaevski equation. In the following chapter we will be investigating the dynamical properties of the condensate, and thus require the time-dependent form of the equation, which can be written as

$$i\hbar \frac{\partial \Psi(\vec{r}, t)}{\partial t} = \left( -\frac{\hbar^2}{2m} \nabla^2 + V(\vec{r}, t) + NU_0 |\Psi(\vec{r}, t)|^2 \right) \Psi(\vec{r}, t) \quad (3.1)$$

where

$$U_0 = \frac{4\pi\hbar^2 a}{m} \quad (3.2)$$

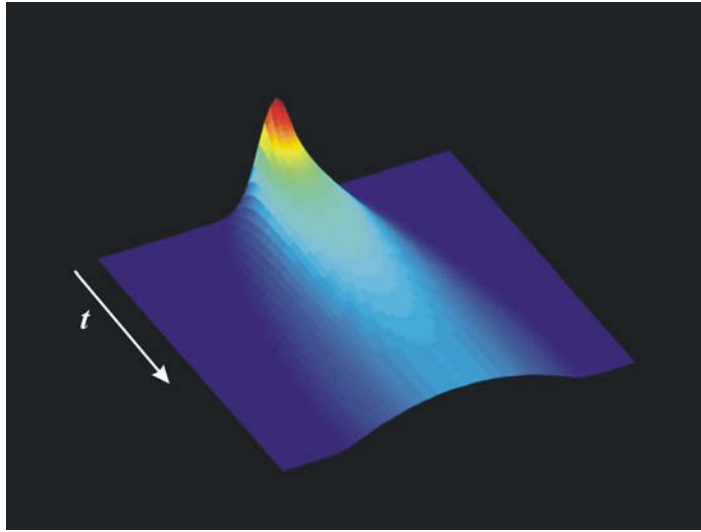


**Figure 3.1:** Expansion or self-defocussing of a BEC as a result of an increasingly positive scattering length.

While the mean-field approach is not valid for all situations (see, for example, [83]), it is nonetheless a widely applicable description which allows the expansion and collapse of the condensate to be controlled with one parameter, the scattering length  $a$ , as we shall shortly demonstrate.

### Numerical evolution of the Gross-Pitaevskii equation

The effect of  $a > 0$  can be seen by solving the Gross-Pitaevskii equation (GPE) numerically, increasing the value of  $a$  as a function of time  $t$ . Physically, a positive scattering length implies the existence of a repulsive interaction potential between atoms. We find that for  $a > 0$ , the condensate expands as the magnitude of  $a$  grows larger and the mean-field energy resulting from the mutual repulsion of the atoms increases. In traditional non-linear optics this behavior would be termed self-defocussing (figure 3.1). For  $a < 0$ , the opposite occurs. The condensate contracts, exhibiting self-focussing behavior (figure 3.2). Eventually, for  $a < a_{critical}$ , it becomes unstable and collapses, resulting in ‘Bose-nova’ implosions.

One can ask where these numerical examples correspond to any physical reality; the answer is yes. The  $s$ -wave scattering length between atoms in a condensate can be experimentally tuned via Feshbach resonances, resulting in condensate expansions and collapses, just as we have demonstrated here. In addition, the effect of the kinetic energy term in Eq. 3.1 can also be similarly illustrated. First  $a$  is ramped down, from  $a > 20$  to  $a = 0$ , at which point the atoms neither attract nor repel each other, and the mean-field energy is zero. Then we release the condensate from the trap, i.e.,

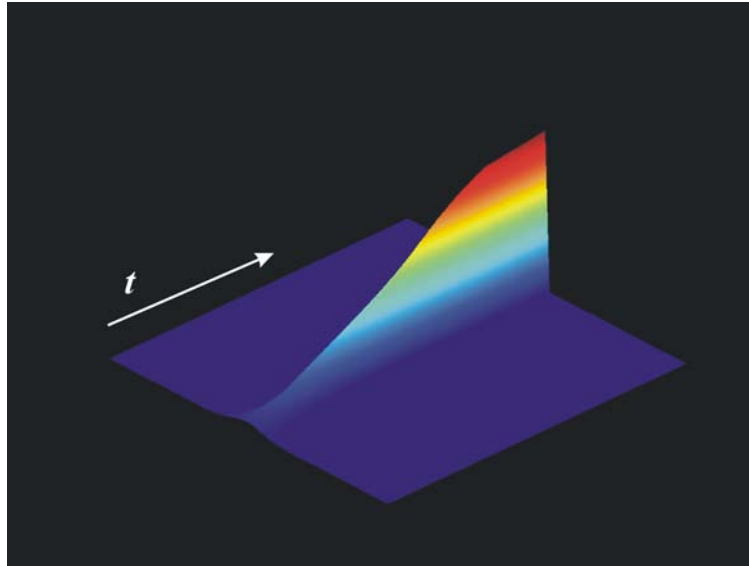


**Figure 3.2:** Collapse or self-focussing of a BEC as the result of an increasingly negative scattering length.

we make  $U_{ext}(\vec{r})$  also zero. The resulting expansion is now due solely to the kinetic energy of the trapped atoms. This expansion is exactly what happens during a time-of-flight measurement of a thermal cloud (figure 3.3).

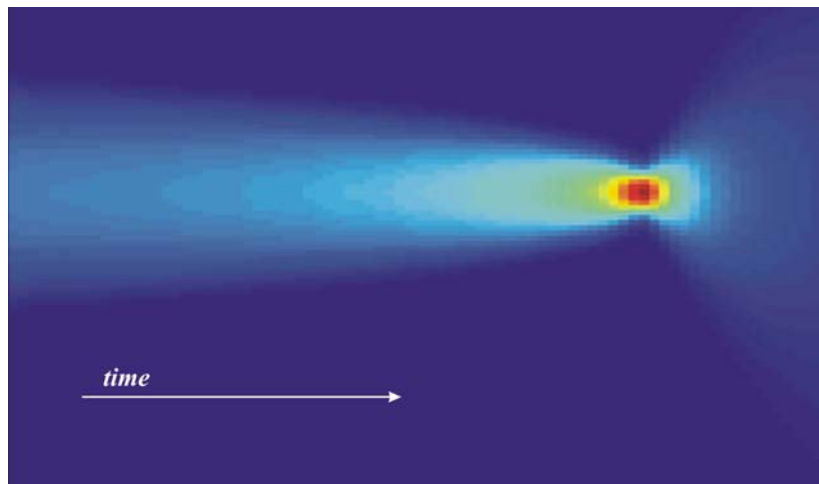


**Figure 3.3:** Contraction of an initially repulsive BEC as  $a \rightarrow 0$ , followed by release from the trapping potential and expansion due to stored kinetic energy. Temporal direction runs from left to right.

The question that remains is what happens, when the kinetic energy of the atoms, which as we have seen, causes an expansion, is exactly counter-balanced by the contraction or collapse due to a negative scattering length?

Then we obtain clouds of atoms which, when released from the trap, neither collapses, nor expands. These so-called solitons are the subject of the following article [84].

## 3.2 Non-linear atom optics with bright matter wave soliton trains

### 3.2.1 Abstract

Bright soliton train creation and evolution in a Bose-Einstein condensate is simulated numerically using the experimental conditions of Strecker *et al.* [Nature, **417**, 150 (2002)] as a starting point. We identify the controlling factors that dictate soliton number, phase-imprinting, and stability. Reliable production of multiple phase-engineered condensed matter pulses can have practical applications to future non-linear atom optics experiments, which we illustrate with an example of co-linear scattering between repulsive solitons.

### 3.2.2 Introduction

Recent experiments [1, 85] show that a Bose-Einstein condensate (BEC) of atoms with an attractive interaction can produce coherent matter wave pulses that propagate without dispersion. In such pulses, or ‘bright’ solitons, the kinetic energy which causes an untrapped condensate to expand is exactly counter-balanced by the inward pull of the mutually attractive atoms, an interaction that under other conditions may result in condensate instability and collapse. In this paper we numerically simulate the results of one such experiment (Strecker *et al.* [1]) to (i), demonstrate that a mean-field approach is capable of describing an attractive condensate in an area of non-linear behavior such as soliton creation, and (ii), investigate the soliton interactions by extending the experimental parameters.

The first solitons in a BEC were observed as propagating dark notches in repulsive condensates [86, 87]. In these experiments phase-imprinting by non-uniform illumination of the condensate engineered a phase step in the BEC. By establishing a ‘light block’ in the condensate, dark soliton trains have also been generated [88]. Of equal interest is the creation of bright solitons, which has been the subject of several theoretical studies [89, 90, 91, 92]. Bright solitons require an attractive interaction i.e. a negative scattering length, which only allows condensation under a very restricted range of conditions. However, success in the manipulation of the condensate scattering length through Feshbach resonances [93] has since made experimental investigations feasible, and this development has generated a great deal of recent experimental and theoretical activity [1, 85, 94, 95].

In the experiment we study, the released BEC formed a train of multiple solitons which oscillated collectively in a weak harmonic potential for many cycles, each soliton kept apart from its neighbor by the alternating phase structure of the ensemble [1]. This result suggests the possibility of designing a series of self-focussing, phase-engineered coherent matter pulses as the basis of future experiments in non-linear atom optics.

Bose-Einstein condensates can be well-described by the Gross-Pitaevskii (non-linear Schrödinger) equation (GPE), which treats the condensate as a single atomic wavefunction subjected to the mean field attraction or repulsion of the atoms. Previous investigations of the GPE have predicted that stable solitons may be found experimentally when the number of atoms per soliton is small and the condensate is quasi-one dimensional (1D) [89, 90]. In this regime the condensate healing length  $\xi = (4\pi na)^{-1/2}$  is larger than the transverse radius of the confining potential, where  $n$  is the condensate density and  $a$  is the s-wave scattering length [96]. In addition, stationary solutions of the GPE have suggested that trains of solitons may be observed in condensates which have undergone a non-adiabatic excitation [89]. One significant contribution of the recent experimental results is their support of the assumption that the GPE is equally applicable to condensates of both positive and negative scattering length.

Experimentally, as described in [1], a quasi-1D condensate was formed in a box-like potential with significantly tighter confinement in the transverse than the axial dimension. Manipulation of a Feshbach resonance rapidly tuned the scattering length of the atoms from positive to negative, resulting in a condensate which became attractive at, or shortly after, its release. Most of the unconfined atoms were ejected in a burst, leaving behind a small proportion of remnant atoms as solitons. These were allowed to evolve as they propagated along the axial potential of a far red-detuned laser field for a short time before being imaged.

The dynamic nature of the experimental initial conditions suggests that the first step to understanding the mechanism of soliton train formation and phase-imprinting is best facilitated by a time-dependent model. We present the results of a dynamic simulation of soliton train creation, based on the numerical solution of the time-dependent GPE. By adhering closely to the experimental conditions [1] we are able to reproduce the factors which determine the stability, number, and phase relationships of the solitons.

An understanding of the manipulation and control of these fundamental characteristics will assist the design of future experiments. As an example, we present a numerical simulation of a co-linear scattering experiment.

### 3.2.3 Simulating a quasi-1D condensate

We begin with the non-linear Schrödinger equation (NLSE),

$$i\hbar \frac{\partial \Psi(\mathbf{r}, t)}{\partial t} = \left( -\frac{\hbar^2}{2m} \nabla^2 + V(\mathbf{r}, t) + NU_0 |\Psi(\mathbf{r}, t)|^2 \right) \Psi(\mathbf{r}, t). \quad (3.3)$$

This is a mean-field description of an evolving nonlinear macroscopic quantum state that describes the behavior of  $N$  condensate atoms when the temperature is close to zero by taking  $U_0 = 4\pi\hbar^2 a/m$ , where  $m$  is the atomic mass [97]. We will assume that  $V$  is a cylindrically symmetric potential, with transverse and axial dimensions given by  $(r, z)$  respectively.

Since the condensates in experiments [1, 85] are in the quasi-1D regime, several simplifications can be made that reduce the dimensionality of Eq. (3.3). As described in [90], a condensate under much greater transverse than axial confinement with trap frequencies such that  $\omega_r/\omega_z \gg 1$  can be approximated as a separable wavefunction of the form,

$$\Psi(r, z, t) = \phi(r)\psi(z, t), \quad (3.4)$$

where within the energy regime of the low-order modes of  $\psi(z, t)$ , the most probable state for the tightly trapped component  $\phi(r)$  is the ground-state.

As  $V = \frac{1}{2}m\omega^2 z^2$  the system has natural units (harmonic oscillator units, h.o.u.) of characteristic length and time based on the size of the non-interacting ground-state wavefunction and the period of harmonic oscillation. Replacing  $(z, t)$  with  $\xi = (\hbar/2m\omega)^{-\frac{1}{2}}z$  and  $\tau = \omega t$  in the 1D version of Eq. [3.3] results in a dimensionless form of the NLSE [97],

$$i \frac{\partial \psi(\xi, \tau)}{\partial \tau} = \left( -\frac{\partial^2}{\partial \xi^2} + \frac{1}{4}\xi^2 + C|\psi(\xi, \tau)|^2 \right) \psi(\xi, \tau), \quad (3.5)$$

where, in order to normalize the wavefunction, the non-linear coefficient  $C = 4\pi Na(\hbar/2m\omega)^{-\frac{1}{2}}$ .

Finally, following the treatment of Saito *et al.* [98], Eq. (3.5) can be extended to include atomic losses due to inelastic collisions,

$$\begin{aligned} i \frac{\partial \psi(\xi, \tau)}{\partial \tau} = & \left( -\frac{\partial^2}{\partial \xi^2} + \frac{1}{4}\xi^2 + C|\psi(\xi, \tau)|^2 \right. \\ & \left. -i \left( L_2 \frac{|\psi(\xi, \tau)|^2}{2} + L_3 \frac{|\psi(\xi, \tau)|^4}{6} \right) \right) \psi(\xi, \tau), \end{aligned} \quad (3.6)$$

where  $L_2$  and  $L_3$  are the two-body and three-body recombination loss-rate coefficients, respectively.

### 3.2.4 Numerical results and analysis

Reliable methods of soliton creation and phase-imprinting are required if bright matter wave soliton trains are to be a useful source of coherent wave-packets. We first present an analysis of these processes, based on the experimental work performed by Strecker *et al.*. We then show that within the existing experimental parameters it is possible to create scattering between matter wave solitons.

Eq. (3.5) was numerically integrated using a fourth order Runge-Kutta method. To obtain the numerical equivalent of the initial repulsive condensate in [1], we started with the analytical non-interacting ground-state solution and adiabatically ramped to a large and positive  $C$ . The ramp is then rapidly reversed to  $C < 0$ , a parallel to the experimental manipulation of a Feshbach resonance. Concurrently in a time interval  $\Delta\tau \approx 1$  h.o.u. before the end of the reverse ramp the original harmonic trap is replaced by a much weaker one displaced by  $\xi \approx 20$  h.o.u. with respect to the first. This is equivalent to releasing the condensate from the side of a gentle potential well. Thus the initially stationary condensate will acquire some non-zero velocity  $v$ .

The resulting condensate density Fig. 3.4 shows a train of three wave-packets which exhibit soliton-like behavior. These are found to oscillate stably for many periods with neither observable dispersion nor particle exchange. Non-interacting particles simultaneously released from different points of a harmonic oscillator will overtake each other every half-period. In contrast, as in [1], our simulated particle trajectories do not intersect, indicating that the solitons are kept apart by a repulsive force.

Mutual repulsion between two solitons arises from their opposing phase [99]. In a stationary train of equal-sized repulsive pulses this leads to a series of  $\pi$  phase steps between neighboring solitons [89]. The condensate in [1] may acquire such a phase structure if the phase gradient is determined by velocity such that  $d\phi/dz = mv/\hbar$ . Our spatial phase profiles show that finite phase steps can be expected whenever the solitons are repulsive and non-overlapping. Lack of effective phase-imprinting, such as when the reverse ramp is insufficiently rapid, leads to solitons with arbitrary phase relationships, as is evident from their random relative motion.

In agreement with [1] we have found that  $N_s$  increases linearly with  $\Delta\tau$ , enabling us to vary the number of solitons created (Fig. 3.4, inset). One possible explanation is that a total phase difference of  $\phi = N_s\pi$  is required to produce  $N_s$  solitons of alternating phase, and therefore  $N_s \propto v$ . This was observed experimentally, where  $v$  was controlled through manipulation of the time interval  $\Delta\tau$  between the release of the condensate and the end of the decreasing ramp, such that  $v \propto \Delta\tau$  [1]. In the simulation we start from  $N_s = 1$  for  $\Delta\tau = 0$ . However, in the experiment  $N_s = 4$  for  $\Delta\tau = 0$ . We note that the predicted single solitons were not observed, perhaps because

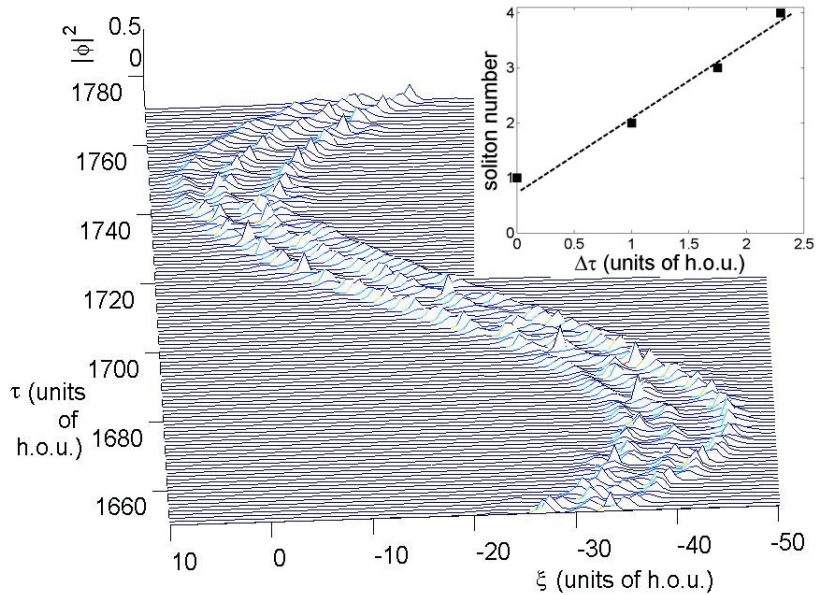


**Figure 3.4:** Evolution of a train of three repulsive solitons as they propagate in a weak harmonic potential. The plot is of  $|\phi(\xi, \tau)|^2$  the condensate density distribution, *vs.* normalized length and time. At  $\tau = 0$  (units of h.o.u.) the non-linear constant here was ramped from  $C = 200$  to  $C = -22$  over a period of  $\tau = 5$ , and the condensate was released at  $\Delta\tau = 1.75$  into a harmonic potential  $V/600$  where  $V$  is the initial trapping potential. Inset shows a plot of soliton number *vs.* release time (h.o.u.), with conditions as for the main figure.

irregularities in the experimental potential prevent excitation of solely the lowest order modes of the soliton train.

Soliton stability was largely determined by the final value for  $C \propto a$ . As is well known [97], when  $a > 0$  the condensate will expand. If  $a < 0$ , continued increase of the magnitude of  $a$  or  $N$  will cause the condensate to contract to the extent that it can no longer be treated as quasi-1D. For our particular parameters this occurs at  $C_{critical} \approx -23$  [100]. In between lies a regime of stable soliton solutions, within which we find that maximizing  $N_s$  requires the magnitude of  $C$  to be large and close to  $C_{critical}$ . It has been shown that the stability criterion restricts the size of any one soliton to  $\approx 6000$  atoms (taking  $a = -3a_0$ ) [90]. Therefore, for a given phase gradient, a greater atom number can only be supported by the creation of more solitons.

Experimentally, the number of particles in the released condensate greatly exceeds the number that can be stably contained in solitons [1]. In fact most of the released atoms are lost in a burst, and the solitons are

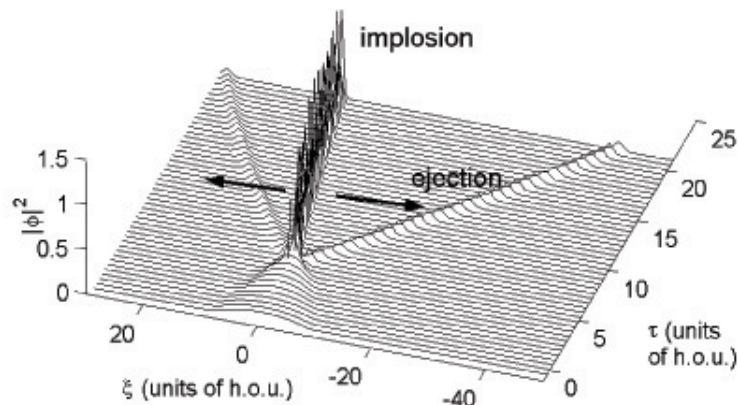


**Figure 3.5:** Implosion and ejection of atoms from the release of a strongly attractive condensate into a weak harmonic potential. The plot is of  $|\phi(\xi, \tau)|^2$  the condensate density distribution, *vs.*  $\xi, \tau$  (units of h.o.u.). At  $\tau = 0$  the non-linear constant here was ramped from  $C = 200$  to  $C = -25$  over a period of  $\tau = 5$ , and the condensate was released at  $\Delta\tau = 1.5$  into a harmonic potential  $V/500$ , where  $V$  is the initial trapping potential.

formed from the small number of atoms in the remnant fraction. To investigate the effect of a burst event on the validity of our conclusions, we employed Eq. (3.6) to take into account the higher peak densities experienced during the negative ramp as the condensate collapses, and performed simulations with negative values of  $C$  just outside the stability regime of the lossless equation. Depending on the extent of the non-linearity we observed both implosions (Fig. 3.5) and soliton-like pulses with this model.

Having studied the process of soliton formation, we then addressed the issue of soliton interactions. Collisions between solitons will occur if particles are given enough kinetic energy to overcome the short range repulsive force, which scales exponentially with pulse separation [99]. Therefore by placing a series of co-linearly propagating repulsive solitons in a steep potential well, it should be possible to extend experiment [1] into a BEC soliton scattering experiment.

Fig. 3.6 shows a pair of pulses in an external potential chosen so that the repulsive interaction is weak compared to the particle momentum. From symmetry, the motion of completely non-interacting pulses will bring them into coincidence at the center of a harmonic potential. If the particles are repulsive we may expect the point of collision to occur later in the oscillation, as is indeed observed here. During the collision, the pulses are barely distinguishable, and the discrete phase steps between pulses are temporar-

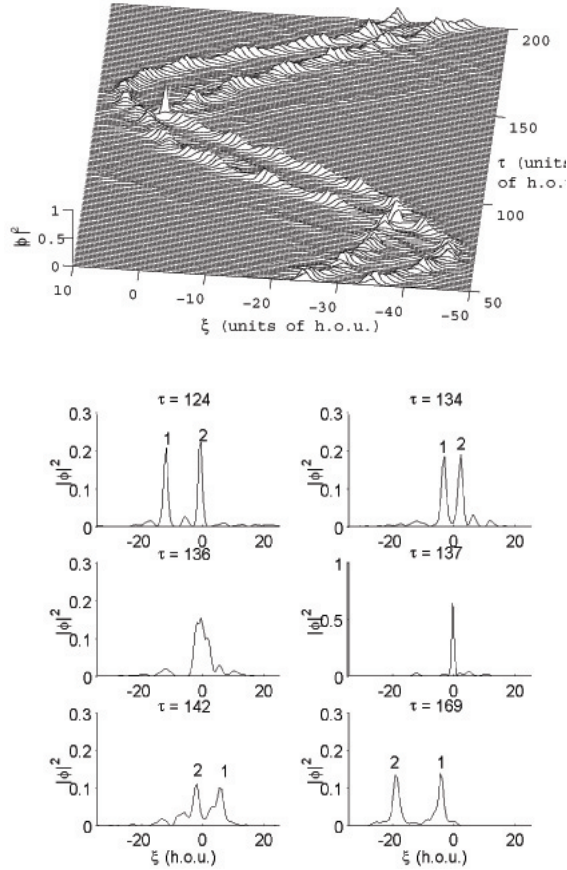


**Figure 3.6:** Co-linear scattering of two repulsive solitons of approximately equal size in a harmonic potential, in which the particle momentum is more dominant than the repulsive interaction. Fig. (3a) is a plot of  $|\phi(\xi, \tau)|^2$  vs.  $\xi, \tau$  (units of h.o.u.). Fig. (3b) shows  $|\phi(\xi, \tau)|^2$  vs.  $\xi$  for different values of  $\tau$  in a collision sequence. Note the change in scale for the fourth subplot. Soliton [1] overtakes and passes through soliton [2] every half a period, at the extreme ends of the potential. At  $\tau = 0$  the non-linear constant here was ramped from  $C = 200$  to  $C = -10$  over a period of  $\tau = 5$ , and the condensate was released at  $\Delta\tau = 1.5$  displaced  $\xi = -20$  from the center as for fig. 3.4, into a harmonic potential of the form  $V/500$  where  $V$  is the initial trapping potential.

ily lost. After the scattering event each pulse regains its identity with no obvious particle exchange, as is evident from the lack of growth of any one soliton at the expense of another after many cycles. Following each collision the solitons eventually become sufficiently well-separated for their opposing phase relationships to again become apparent. Each collision causes a

spatial displacement of the solitons similar to scattering of elastic particles. Thus the results are akin to those found for the scattering of optical 1D solitons and 3D ‘light bullets’ in a 1D potential [99, 101]. Further analysis of soliton interaction should be possible through an analytical model such as presented in reference [102].

### 3.2.5 Conclusion

As for their optical counterparts, bright matter wave solitons may be useful as non-linear atom optical wavepackets. In this paper we have attempted to demonstrate that further manipulation of bright solitons with existing technology can potentially uncover a rich variety of interesting non-linear matter wave phenomena.

We have reproduced the soliton trains observed in [1] and also shown that experiment [1] is capable, with minimum modification, of demonstrating the scattering of co-linearly propagating solitons, allowing measurement of the repulsive force between them. Spatial coherence may also be demonstrated if interference fringes are observed during the collision [103]. This has implications for the use of soliton trains as an atom laser.

In addition, pulses of different particle number will have different sized non-linearities and hence different interaction potentials. Finally, creation of mutually attractive solitons for which  $\phi = 0$  will allow the first studies of matter wave soliton capture and fusion.

### 3.2.6 Acknowledgments

We gratefully acknowledge Yu. S. Kivshar and E. A. Ostrovskaya for helpful comments on the manuscript.

## 3.3 Factors determining soliton number

One discussion which has continued after the publication of Ref. [1] concerns the true identity of the physical process which determines soliton number. In the experiment, the number of solitons formed  $N_s$  was observed to scale with the time interval  $\Delta\tau$  between when the condensate was released out of tight confinement into the shallow harmonic potential, and the point at which  $a$  becomes positive.

As the oscillation period of the harmonic potential is large, varying  $\Delta\tau$  is equivalent to releasing the initial condensate at different displacements from the center of the trap. As a result, initially the number of solitons created was tentatively attributed to depend on how fast the condensate was moving when  $a$  changes sign [1]. It was postulated that the motion of the condensate creates a phase gradient across it,  $d\phi/dz = mv/\hbar$ , which subsequently leads to the separation of sections of the condensate into individual solitons with

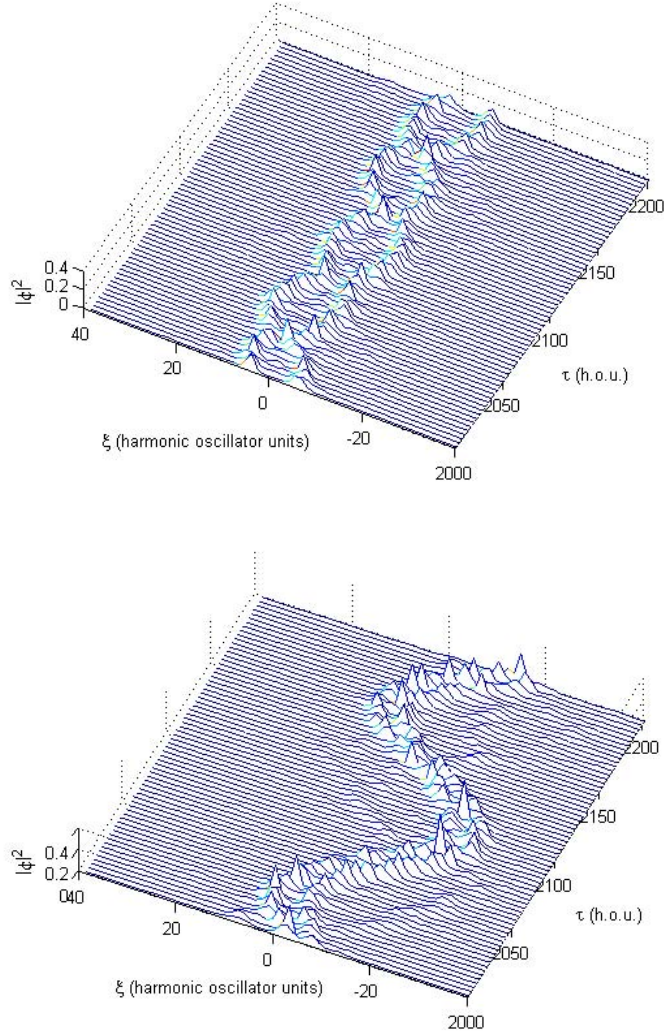


**Figure 3.7:** Investigation of the dependence of soliton number on the initial velocity of the released Bose-condensate. The plots are of the condensate density distribution  $|\phi(\xi, \tau)|^2$ , vs. normalized length  $\xi$  and time  $\tau$ . At  $\tau = 0$  (h.o.u.) the non-linear constant was ramped from  $C = 200$  to  $C = -10$  over a period of  $\tau = 5$ , and the condensate was released at  $\Delta\tau = 1.5$  into a harmonic potential  $V/500$  where  $V$  is the initial trapping potential. In the first plot the condensate was released with no initial offset from the center of the trap, in the second plot from an offset of  $\xi = 10$  h.o.u.. Comparison of the results shows that in both cases two solitons were created, and that they differ only in the amplitude of their oscillation in the shallow harmonic potential.

$\pi$ -phase steps between them. An earlier release time will lead to a larger phase gradient, and more solitons, such that  $N_s = \phi/\pi$ .

It was soon noted, however, that releasing the condensate at different potential depths would only vary the center-of-mass motion of the entire ensemble. It cannot cause any relative motion within the condensate itself which could produce a phase gradient and thus influence soliton formation. Since in our simulations we observed the same linear relationship between  $N_s$  and  $\Delta\tau$  (Fig. 3.4 (inset)), this argument can be demonstrated numerically. Fig. 3.7 shows the results of two simulations which were identical in all respects except for where in the trap the condensate was released. It can be seen that, for a given time difference  $\Delta\tau$ ,  $N_s = 2$  regardless of whether the condensate was kept at the bottom of the trap and had no center-of-mass motion, or if it was released from one side and gains some velocity  $v$ .

It is now postulated that what actually happened in the original experiment was that, by increasing the time between the release of the condensate out of confinement and the switching on of attractive interactions, the condensate is allowed to expand to greater axial sizes, which allow a larger number of solitons to be supported. This was tested by a follow-up experiment from Strecker *et al.* [104].

This outcome left one remaining question – if the alternating phase structure was not created through the relation  $d\phi/dz = mv/\hbar$ , how is it created? An explanation based on quantum-mechanical phase fluctuations has been proposed by Al Khawaja *et al.* [95]. Alternatively, it has been suggested that solitons are created with arbitrary phases and evolve through collisions and collapses into a stable configuration [104, 105].



## Chapter 4

# Conclusion and Outlook

### 4.1 UV-free He\* lithography

In the first part of this thesis, I presented an experimental scheme for UV-free lithography with metastable helium atoms. Based on the short de Broglie wavelength of atoms and the numerous techniques available for their manipulation, neutral atom lithography remains a viable potential route to sub-micron structuring of semi-conductor surfaces. Metastable helium, with its high internal energy, is one of the model systems in resist-based atom lithography. The experiment I developed allows He\* exposures to be performed in a better controlled environment than previously possible, and the interaction between the metastable atom and the self-assembling monolayer to be investigated with fewer secondary effects.

#### 4.1.1 Exposures with magnetically focussed atoms

Following the experimental developments reported in Chapter 1, further magnetic focussing and UV-free lithography exposures with metastable He atoms have been performed based on this scheme ([40], [106]).

The images in the left column of Fig. 4.1 show optimized focussing with the hexapole lens. In the absence of the lens, the signal from the He\* atoms is diffuse and relatively weak, compared to the clear focussing of atoms around the needle when the lens is inserted. Furthermore, the dependence of the average longitudinal velocity on source pressure was observed to cause an observable shift in the position of the focus. On the right-hand side of Fig. 4.1, a comparison is made between focussing obtained at high source pressures, and hence high longitudinal velocities (Sec. 1.5.4), and that at low source pressures and velocities.

Finally, lithography experiments were performed in the UV-free region behind the shadow of the needle, at a discharge voltage of 1200 V and a flux of  $\sim 4 \times 10^{11}$  atoms/cm<sup>2</sup>/s, which required an exposure time of 30 min. Scanning electron microscopy images at increasing magnifications

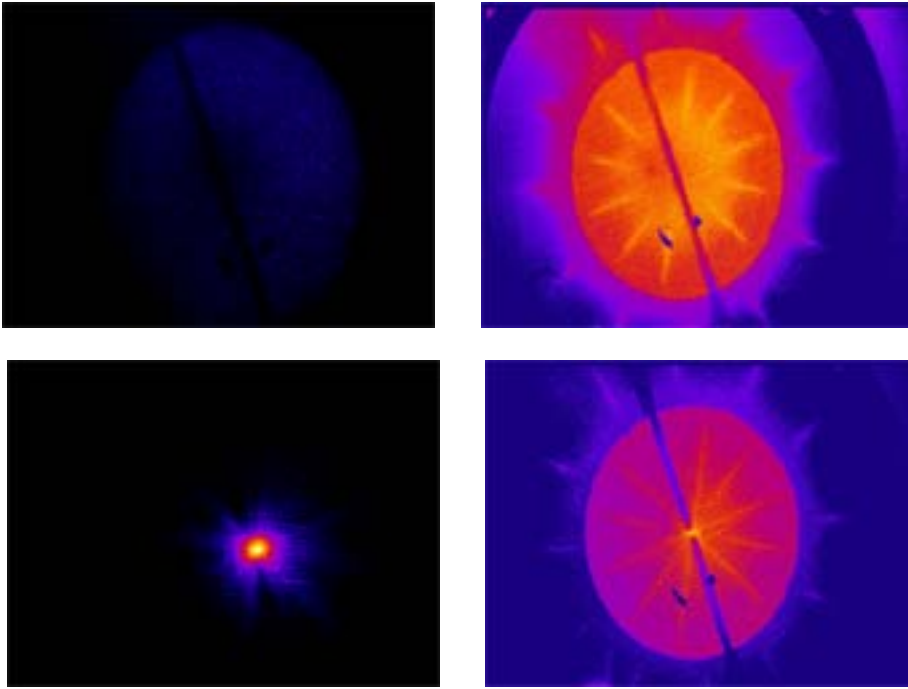


**Figure 4.1:** Magnetic focussing of metastable helium atoms around a needle. MCP images in the left column show the atomic beam without (top) and with (bottom) a hexapole magnetic lens. Images in the right column demonstrate the velocity dependence of magnetic focussing. The sharpness of the beam focus varies dramatically in response to changes in the gas pressure in the metastable helium source. The top image was obtained at a high gas pressure, corresponding to high atom velocity. The bottom image shows focussing at low gas pressure and velocity.

of the resulting exposed substrate is shown in Fig. 4.2, where a mask with holes of diameter  $200 \mu\text{m}$  had been used to produce the pattern transferred. The region exposed to metastable helium atoms focussed by the hexapole lens can be seen as a spot in the center of in the unexposed stripe across the substrate, which corresponds to the shadow of the needle. Within this central spot, the exposure is from magnetically focussed  $\text{He}^*$  only and is UV-photon free.

## 4.2 Ultracold collisional studies with Rb and Cs mixtures

In the second part of the thesis, I have presented the preparation of a magnetically trapped, binary bosonic mixture, and steps in the investigation of two- and three-body collisions between  $^{87}\text{Rb}$  and  $^{133}\text{Cs}$  in the cold and ultracold, quantum degenerate regime. Ultracold mixtures offer the possi-

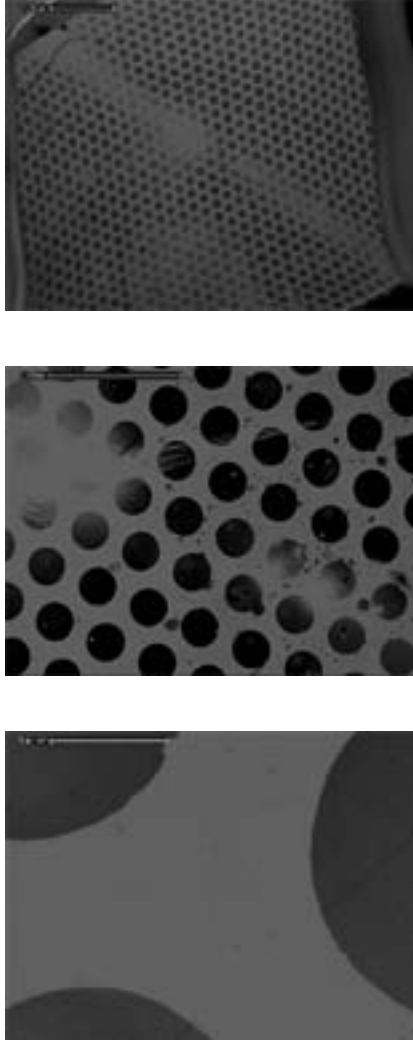


**Figure 4.2:** UV-free lithography with metastable He. SEM-images at increasing magnifications of a gold-coated silicon substrate exposed to metastable He atoms at the focus of the hexapole lens (Fig. 4.1). The light stripe across the center of the top image represent regions in the shadow of the needle. In the middle of this area is a well-exposed region corresponding to exposure by the focussed atoms. In addition there is some exposure outside this region due to imperfect focusing by the lens. The second and third image shows the region exposed to the focussed atoms at greater magnification. Samples were exposed for 30 min at a flux of  $\sim 4 \times 10^{11}$  atoms/cm<sup>2</sup>/s. Gold regions are light, silicon regions dark. The holes in the mask have a diameter of 200  $\mu\text{m}$ .

bility of studying novel many-body behavior and the deterministic creation of cold heteronuclear molecules, which have been implicated, for example, in schemes for quantum computation [107]. I have shown that we have achieved simultaneous transfer of an atomic mixture of rubidium and cesium to a magnetic trapping potential, and can control the temperature of rubidium in a species-selective way, facilitating the application of sympathetic cooling methods as well as re-thermalization measurements which could lead to the determination of important interaction parameters such as the Rb-Cs  $s$ -wave scattering length.

#### 4.2.1 Determination of $a_{RbCs}$ and Feshbach resonances

Currently measurements are underway to determine the  $s$ -wave scattering length between rubidium and cesium. As we have seen, this parameter plays a pivotal role in many processes at ultracold temperatures, in both thermal clouds and Bose-condensates. Its accurate determination will allow interesting questions to be answered, such as the whether it is possible to sympathetically cool Cs down to quantum degeneracy with ultracold Rb, as well as the estimation of important parameters, such as the Rb-Cs three-body loss rate  $L_{3,RbCs}$ .

Further to this, the next experimental goal is to transfer the atomic mixture to an optical dipole trap, created with a far-detuned laser. In optical traps atoms do not have to be spin-polarized, allowing large external magnetic fields to be applied for experiments with Feshbach resonances. A Feshbach resonance is a scattering resonance in which free pairs of atoms are tuned via the Zeeman effect into a vibrational state resonance of a diatomic molecule. The presence of a Feshbach resonance can be experimentally observed as an enhanced loss due to inelastic collisional processes such as molecule formation.

Therefore if a Feshbach resonance for the Rb-Cs system is found, it would allow  $a_{RbCs}$  to be experimentally varied as a function of the applied magnetic field. As we have seen in Chapter 2, the scattering length controls the rate of elastic collision, and thus, evaporative and sympathetic cooling, as well as being the determining parameter in the rate of three-body recombination. Although it is in general considered difficult to theoretically predict the location of Feshbach resonances in the Rb-Cs system, examination of other mixed alkali systems give good reasons to believe that a high probability exists of finding a Rb-Cs resonance within an experimentally achievable range of applied magnetic field strengths. With the newly installed magnetic coil system, magnetic offset fields of up to 1000 G can be created for such experimental attempts.

Ultimately, the ability to controllably manipulate the scattering length will allow pairs of Rb and Cs atoms to be brought together to form molecules, in a reversible process that, unlike conventional chemical processes, does not

involve excess energy other than the binding energy.

In addition, Feshbach resonances will allow the investigation of some of the most currently intriguing aspects of three-body physics. Recent experiments [79, 80] have demonstrated enhancement of three-body recombination at a Feshbach resonance, an effect attributed to the influence of Efimov physics on these neutral atom interactions. As we have seen, for  $a < 0$  the universal analytical model of Esry *et al.* (Eq. 2.43) predicts a smooth increase in the number of recombination events with increasingly negative  $a$ . However, numerical calculations performed simultaneously have shown features of a resonance in this region at which three-body recombination rates are strongly enhanced [74]. By measuring the three body loss rate in the vicinity of a Feshbach resonance, such a resonance feature have now been observed experimentally with a Cs condensate, and attributed to the binding of three atoms in an Efimov trimer state, a quantum state which is predicted to form a universal set as a function of the two-body interaction strength [108, 80].

All of the above points to a plethora of rich and interesting physics which can be explored with our ultracold mixture experiment through the controllable manipulation of the Rb-Cs scattering length.

### 4.3 Matter-wave soliton trains

Finally, I presented a numerical study of non-linear behavior in a Bose-Einstein condensate, initiated by a rapid change in the sign of the scattering length. Experiments such as these represent investigations into condensate behavior at the important crossover region from positive to negative values of  $a$ , a crossover that is traversed in many important processes, such as the formation of molecular Bose-condensates and the onset of superfluidity in degenerate Fermi gases. Solitonic solutions represent a way in which a condensate can remain stable during such rapid and dramatic transitions. This is perhaps one of the reasons why matter-wave soliton trains continue to be an area of theoretical and experimental investigation — very recently, for example, soliton trains were produced for the first time in a three-dimensional potential [109].



# Appendix A

## Atomic data

The following tables summarize some important properties of the atomic species discussed in this thesis. The values for the rubidium and the cesium scattering length,  $a_{Rb}$  and  $a_{Cs}$ , are currently the most accurate determinations available.

Mass	$m_{He}$	$6.65 \cdot 10^{-27}$ kg
Metastable level		$2^3S_1$
Excitation energy		19.82 eV
Ionization energy		24.580 eV
Lifetime		7900 s

**Table A.1:** Selected physical properties of the metastable  $^4\text{He}$  atom, extracted from Ref. [14].

Mass	$m_{Rb}$	$1.44 \cdot 10^{-25}$ kg
$^2S_{1/2}$ ground state HFS	$\omega_{hfs}$	$2\pi \cdot 6.834682611$ GHz
Wavelength (D2-transition)	$\lambda$	780.03 nm
Natural linewidth (D2-transition)	$\Gamma$	$2\pi \cdot 6.07$ MHz
Saturation intensity (D2-transition) $ F = 2, m_F = 2\rangle \rightarrow  F' = 3, m_{F'} = 3\rangle$	$I_0$	17 W/m <sup>2</sup>
Two-body scattering length	$a_{Rb}$	$(98.98 \pm 0.04) \cdot a_0$

**Table A.2:** Selected physical properties of the  $^{87}\text{Rb}$  atom. All numerical values are extracted from Ref. [113], except for the scattering length, which is from Ref. [115]. ( $a_0 = 0.0529177$  nm)

Mass	$m_{Cs}$	$2.21 \cdot 10^{-25}$ kg
$^2S_{1/2}$ ground state HFS	$\omega_{hfs}$	$2\pi \cdot 9.192631770$ GHz (exact)
Wavelength (D2-transition)	$\lambda$	852.11 nm
Natural linewidth (D2-transition)	$\Gamma$	$2\pi \cdot 5.22$ MHz
Saturation intensity (D2-transition) $ F = 4, m_F = 4\rangle \rightarrow  F' = 5, m_{F'} = 5\rangle$	$I_0$	11 W/m <sup>2</sup>
Two-body scattering length	$a_{Cs}$	$(2400 \pm 100) \cdot a_0$

**Table A.3:** Selected physical properties of the  $^{133}\text{Cs}$  atom. All numerical values are extracted from Ref. [114], except for the scattering length, which is from Ref. [116]. ( $a_0 = 0.0529177$  nm)

## Appendix B

# Cesium optical system

In this Appendix I present further details of the optical systems we have added to the main BEC experiment for the simultaneous cooling and trapping of cesium.

Figure B.1 is a schematic diagram of the optical setup for the cooling, reference, and imaging laser systems at 852 nm. For the cooling laser system, the output of a diode laser is split into two beams, the majority of which is coupled into a single-mode polarization-preserving fiber which runs to the main experiment depicted in Fig. B.3. The remaining light is used for frequency stabilization, which is composed of three sub-systems: DAVLL, saturation spectroscopy, and heterodyne referencing.

The DAVLL scheme employs a magnetic field to split the  $m_F$  levels of the Doppler-broadened resonance of the atom. The difference in the absorption rates of these Zeeman components in a right- and left-handed circularly polarized light field is then used to create an dispersive lock signal [57]. In addition, in order to determine and adjust the laser frequency with respect to the cooling transition, saturation spectroscopy [110] and the heterodyne beating of light from the cooling laser with an independent reference laser have been implemented. For the latter, the resultant difference signal from the fast photodiode is monitored with a spectrum analyzer (Model R4131C, manufactured by Advantest).

Adjacent to the cooling laser is the optical setup for the reference and imaging laser systems. Laser light for frequency referencing and imaging are both taken from the same diode laser (here denoted as the ‘Master laser’), which is locked onto the  $F = 4 \rightarrow F' = 4/5$  crossover. As this laser is located in an adjacent laboratory, a single-mode fiber guides the light to the experimental setup, from which it is split into two beams. One is superposed with the cooling laser to create the above-mentioned heterodyne signal for determining the detuning of the cooling laser from the  $F = 4 \rightarrow F' = 5$  transition. The other beam is passed through an acoustic-optical modulator (AOM), where it is up-shifted by 125 MHz so as to be on resonance with

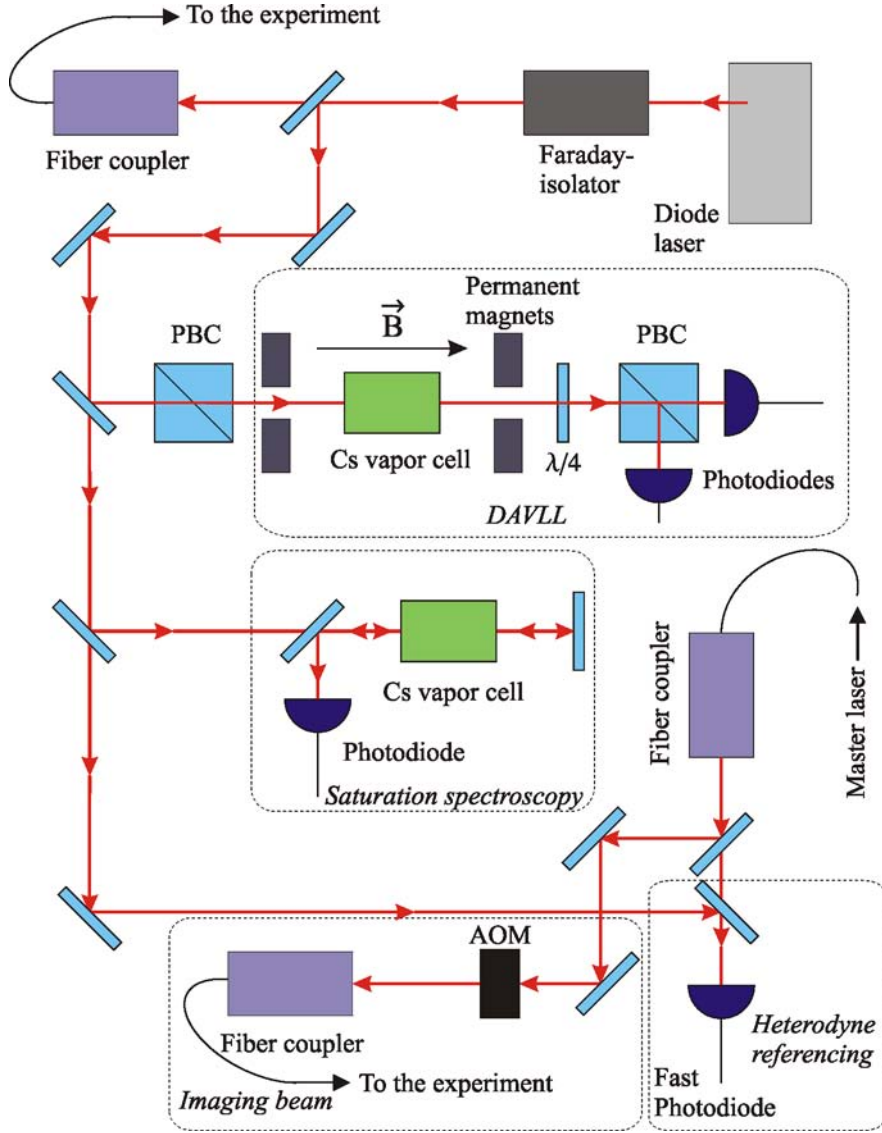


**Figure B.1:** Schematic diagram of the optical setup for the cooling, reference, and imaging laser systems. The output of the diode laser for cooling is split into two beams, the majority of which is coupled into an optical fiber which runs to the main experiment depicted in Fig. B.3. The remaining light is used for frequency stabilization, which is composed of three sub-systems: DAVLL, saturation spectroscopy, and heterodyne referencing, for which further details can be found in the text. An optical fiber brings in light from the reference laser, which is split into two beams, for heterodyne referencing and imaging. (PBC = polarizing beamsplitter cube)

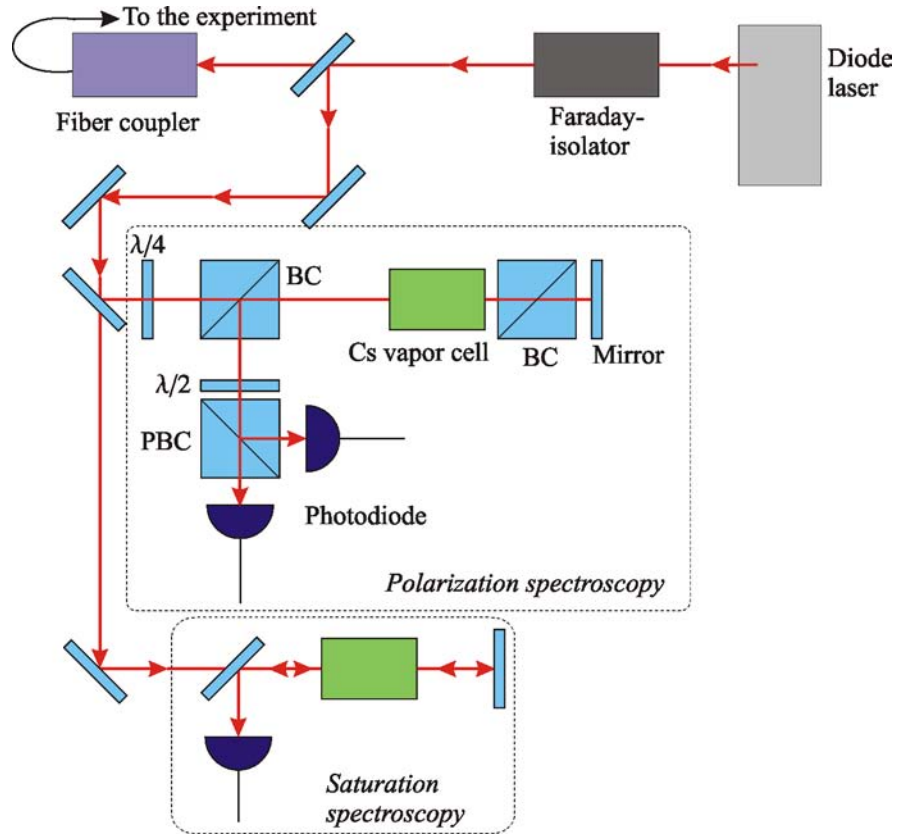


**Figure B.2:** Schematic diagram of the optical setup for the repumper laser system. The majority of light from the repumper diode laser is guided to the main experiment by an optical fiber. A small proportion is used for polarization and saturation spectroscopy, which allows the laser to be locked, and the frequency to be independently monitored. (PBC = polarizing beamsplitter cube, BC = beamsplitter cube)

the  $F = 4 \rightarrow F' = 5$  transition, which is also used for absorption imaging. The AOM allows the imaging beam to be switched on a time scale of a hundred nanoseconds. The beam is then guided to the main experiment by a polarization-preserving, single-mode fiber.

The optical setup of the repumping laser system is depicted in figure B.2. Here again, most of the output of a diode laser is guided to the main experiment by an optical fiber. The rest is divided between a polarization spectroscopy [111, 112] and a saturation spectroscopy setup.

The outgoing optical fibers from figures B.1 and B.2 brings cooling and repumping light at 852 nm to the main experimental setup in the vicinity of the UHV glass cell and magnetic coil system, depicted in Fig. B.3. Here the cooler and repumper are combined at a polarizing beamsplitter cube,

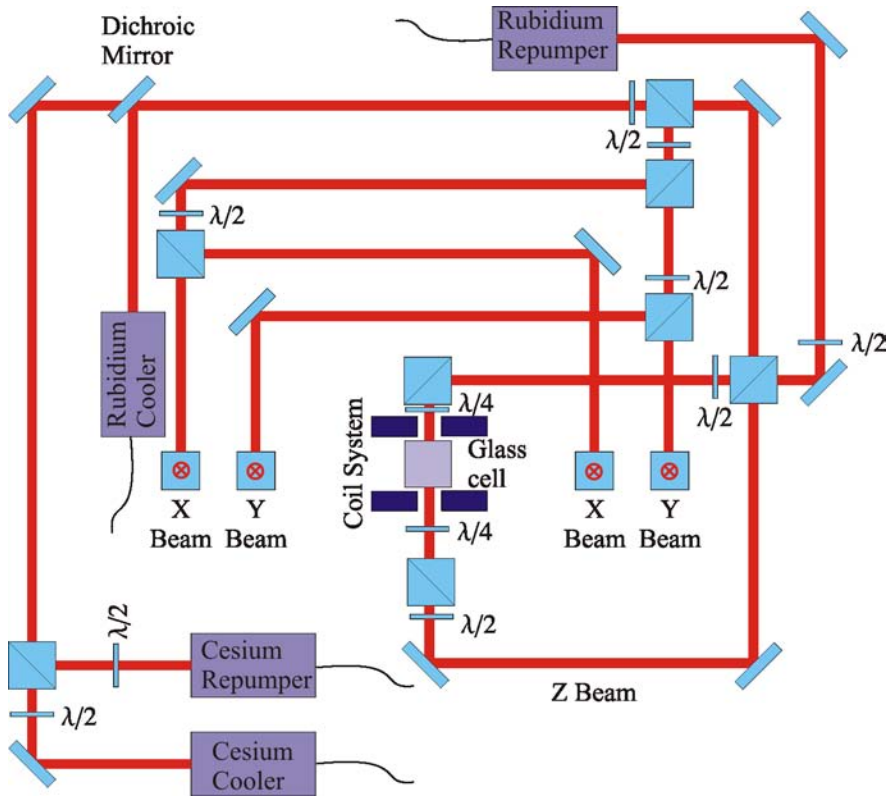


**Figure B.3:** Schematic diagram of the main experimental setup around the UHV-MOT. Cooling and repumping light at 852 nm are combined and superposed with the cooling light at 780 nm at a dichroic mirror. Laser beams at both frequencies are then split into six sub-beams, two for each dimension of the MOT. The  $x$ - and  $y$ -beams enter the glass cell at an angle of  $45^\circ$  from the vertical. (All beamsplitter cubes are polarizing.)

and then inserted into the existing optical system for 780 nm via a dichroic mirror. From that point onwards, the optics for the cooling and trapping of cesium and rubidium are identical. Through the use of  $\lambda/2$ -waveplates followed by a polarizing beamsplitter cube, light is divided into six beams, two in each direction for the  $x$ -,  $y$ -, and  $z$ -dimensions of the MOT respectively.

## Appendix C

# Further experiments with microwave-field dressed potentials

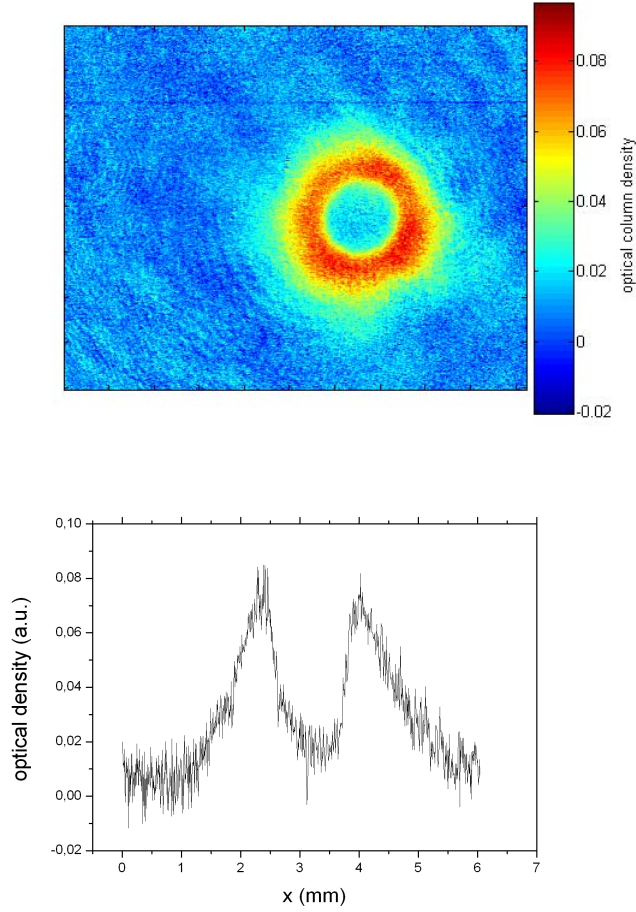
Depending on the direction of the frequency ramp, modifying the trapping potential with microwave fields can produce intriguing features in the spatial and/or momentum distribution of the atomic cloud.

Figure C.1 shows the absorption image and optical density profile taken of a cloud containing  $5.6 \times 10^6$  atoms in the quadrupole magnetic trap after a microwave field has been ramped from 6.83→6.85 GHz over 10 s. After 2 ms time-of-flight, the diameter of the hole in the center of the cloud is  $\sim 1$  mm.

We have inquired into the effect of the polarization of the microwave field on the atomic cloud by rotating the rectangular waveguide antenna by  $90^\circ$ , and observed identical results. This was a point of investigation because the atom-field coupling depends on the orientation of the atom magnetic moment relative to the polarization of the microwave radiation. Therefore changing the polarization might change the orientation of the ring relative to the imaging plane. However we found that this did not occur.

In addition, we have performed a series of relaxation measurements, where, at the end of the upwards frequency ramp, the microwave field was switched off and the atomic cloud stored for a time interval  $\Delta t = 0 - 5$  s. We found that the dip in the optical density profile can be discerned for at least 1 s after the radiation field is no longer present.

Currently two proposed interpretations are being considered. One is that the ring-shaped optical density distribution can be attributed to an atomic cloud held in a microwave field-induced adiabatic potential. By sweeping the microwave field frequency from below resonance to the detuning  $\Delta$ , i.e., in the reverse direction to evaporative cooling, atoms initially in the  $|F = 2, m_F = 2\rangle$  state will be adiabatically transferred to a dressed potential



**Figure C.1:** Absorption image of an atomic cloud after an applied microwave field is swept through resonance to a positive detuning of  $\Delta/2\pi = 15$  MHz (top). An optical density profile taken from a slice through the cloud (bottom), exhibits a dramatic density minimum at the center.

depicted in Figure C.2, where  $\Delta/2\pi = 15$  MHz. The probability that they will follow adiabatically is described by the Landau-Zener effect and can be written as

$$P_{adiabatic} = 1 - e^{-2\pi\Gamma}, \quad (\text{C.1})$$

where  $\Gamma = (1/4)(\Omega^2/d\omega/dt)$ , and  $d\omega/dt$  is the rate of change of the bare-state separation. Taking a Rabi frequency of  $\Omega = 60$  kHz and a sweep time of 5 MHz/s, we find that, for an atomic population of temperature  $200 \mu\text{K}$ ,  $P_{adiabatic} \rightarrow 1$ . An alternative explanation which is also being considered is that as the microwave knife sweeps upwards in frequency, it selects in some way for atoms whose motion has high angular momentum, resulting in a

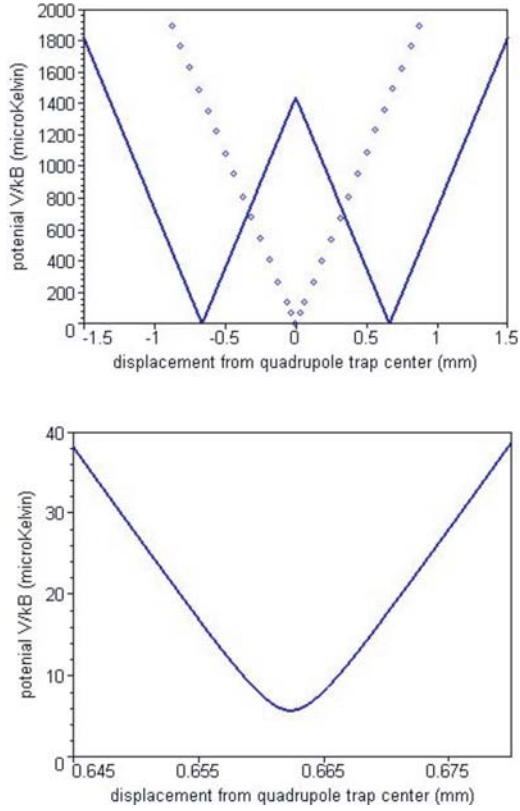


**Figure C.2:** Dressed state potential along the  $z$ -axis for  $\Omega = 60$  kHz and  $\Delta/2\pi = 15$  MHz. The first plot shows the dressed potential (solid line), and the bare potential (dots). In the second plot we have zoomed in on one of the potential minima.

depletion of atoms orbiting near the center of the cloud.

Therefore the exact mechanism which causes the ring of atoms is still under investigation. More generally speaking, strong microwave fields are increasingly being used to modify static magnetic potentials for situations where an arbitrary non-harmonic potential is required, such as in recent experiments with two-dimensional Bose-condensates [117] and on atom chips [118, 119]. Also, in the context of atomic mixtures, we note that a 6.83 GHz microwave-field induced adiabatic potential would exist for rubidium atoms but not for cesium, and would therefore be a species-selective potential.



# Bibliography

- [1] Strecker, K.E., G.B. Partridge, A.B. Truscott, and R.G. Hulet, *Nature* **417**, 150 (2002).
- [2] Timp, G., R.E. Behringer, D.M. Tennant, J.E. Cunningham, M. Prentiss, and K.K. Berggren, *Phys. Rev. Lett.* **69**, 1636 (1992).
- [3] Meschede, D. and H. Metcalf, *J. Phys. D: Appl. Phys.* **36**, R17 (2003).
- [4] Baldwin, K.G.H., *Contemp. Phys.* **46**, 105 (2005).
- [5] Robert, A., O. Sirjean, A. Browaeys, J. Poupard, S. Nowak, D. Boiron, C.I. Westbrook, and A. Aspect, *Science* **292**, 461 (2001).
- [6] Pereira Dos Santos, F., F.J. Léonard, J. Wang, C. J. Barrelet, F. Perales, E. Rasel, C.S. Unnikrishnan, M. Leduc, and C. Cohen-Tannoudji, *Phys. Rev. Lett.* **86**, 3459 (2001).
- [7] Tychkov, A.S., T. Jelte, J.M. McNamara, P.J.J. Tol, N. Herschbach, W. Hogervorst, and W. Vassen, *cond-mat/0510006* (2005).
- [8] Baldwin, K.G.H., private communication (2006).
- [9] Dall, R.G., M.D. Hoogerland, K.G.H. Baldwin, and S.J. Buckman, *J. Opt. B* **1**, 396 (1999).
- [10] Uhlmann, L.J., R.G. Dall, A.G. Truscott, M.D. Hoogerland, K.G.H. Baldwin, and S.J. Buckman, *Phys. Rev. Lett.* **94**, 173201 (2005).
- [11] Morinaga, M., M. Yasuda, T. Kishimoto, F. Shimizu, J. Fujita, and S. Matsui, *Phys. Rev. Lett.* **77**, 802 (1996).
- [12] A. Derevianko, and W.R. Johanson, *Phys. Rev. A* **69**, 1288 (1997).
- [13] G.W.F. Drake, *Phys. Rev. A* **3**, 908 (1971).
- [14] Metcalf, H.J., P. van der Straten, *Laser Cooling and Trapping*, Springer-Verlag, Berlin (1999).
- [15] Lu, W., PhD thesis, Australian National University, (1999).

- [16] Sih, N., BSc thesis, Australian National University, (2000).
- [17] Lu, W., K.G.H. Baldwin, M.D. Hoogerland, S.J. Buckman, T.J. Senden, T.E. Sheridan, and R.W. Boswell, *J. Vac. Sci. Technol. B* **16**, 3846 (1998).
- [18] Lu, W., M.D. Hoogerland, D. Milic, K.G.H. Baldwin, and S.J. Buckman, *Rev. Sci. Instr.* **72**, 2558 (2001).
- [19] Woestenenk, G.R., J.W. Thomsen, M. Rijnbach, P. van der Straten, and A. Niehaus, *Rev. Sci. Instrum.* **72**, 3842 (2001).
- [20] Swansson, J.A., K.G.H. Baldwin, M.D. Hoogerland, A.G. Truscott, and S.J. Buckman, *Appl. Phys. B* **79**, 485 (2004).
- [21] Fahey, D.W., W.F. Parks, and L.D. Schearer, *J. Phys. E* **13**, 381 (1980).
- [22] Ohno, K., T. Takami, K. Mitsuke, and T. Ishida, *J. Chem. Phys.* **94**, 2675 (1991).
- [23] Rooijackers, W., W. Hogervorst, and W. Vassen, *Opt. Commun.* **123**, 321 (1996).
- [24] Vansteenkiste, N., C. Gerz, R. Kaiser, L. Hollberg, C. Salomon, and A. Aspect, *J. Phys. II* **1**, 1407 (1991).
- [25] Carnal, O., M. Sigel, T. Sleator, H. Takuma, and J. Mlynek, *Phys. Rev. Lett.* **67**, 3231 (1991).
- [26] See Ref. [25].
- [27] Doery, M., M. Widmer, J. Bellanca, E. Vredenbrecht, T. Bergeman, and H. Metcalf, *Phys. Rev. Lett.* **72**, 2546 (1994).
- [28] DeKieviet, M., M. Dürr, S. Epp, F. Lang, and M. Theis, *Rev. Sci. Instrum.* **75**, 345 (2004).
- [29] Berggren, K.K., A. Bard, J.L. Wilbur, J.D. Gillaspay, A.G. Helg, J.J. McClelland, S.L. Rolston, W.D. Phillips, M. Prentiss, and G.M. Whitesides, *Science* **269**, 1255 (1995).
- [30] Bard, A., K.K. Berggren, J.L. Wilbur, J.D. Gillaspay, S.L. Rolston, J.J. McClelland, W.D. Phillips, M. Prentiss, and G.M. Whitesides, *J. Vac. Sci. Technol. B* **15**, 1805 (1997).
- [31] Ref. [67] in Thywissen, J.H., K.S. Johnson, R. Younkin, N.H. Dekker, K.K. Berggren, A.P. Chu, M. Prentiss, and S.A. Lee, *J. Vac. Sci. Technol. B* **15**, 2093 (1997).

- [32] Huang, J., D.A. Dahlgren, and J.C. Hemminger, *Langmuir* **10**, 626 (1994).
- [33] Lewis, M., M. Tarlov, and K. Carron, *J. Am. Chem. Soc.* **117**, 9574 (1995).
- [34] Brewer, N.J., R.E. Rawsterne, S. Kothar, and G.J. Leggett, *J. Am. Chem. Soc.* **123**, 4089 (2001).
- [35] Close, J.D., K.G.H. Baldwin, K. Hoffman, and N. Quaas, *Appl. Phys. B* **70**, 651 (2000).
- [36] Johnson, K.S., M. Drndic, J.H. Thywissen, G. Zabow, R.M. Westervelt, and M. Prentiss, *Phys. Rev. Lett.* **81**, 1137 (1998).
- [37] Dunning, F.B., R.D. Rundel, and R.F. Stebbings, *Rev. Sci. Instr.* **46**, 699 (1975).
- [38] Hotop, H., *Exp. Methods Phys. Sci.* **29B**, 191 (1996).
- [39] Ramsey, N.F., *Molecular Beams*, Oxford Science Publications, Oxford (1956).
- [40] Chaustowski, R.R., BSc thesis, Australian National University, (2003).
- [41] Kaenders, W.G., F. Lison, A. Richter, R. Wynands, and D. Meschede, *Nature* **375**, 214 (1995).
- [42] Kaenders, W.G., F. Lison, I. Müller, A. Richter, R. Wynands, and D. Meschede, *Phys. Rev. A* **54**, 5067 (1996).
- [43] Halbach, K., *Int. J. Mod. Phys. B* **4**, 1201 (1990).
- [44] Kaenders, W.G., Doctoral thesis, University of Hannover, (1994).
- [45] McClelland, J.J., M.R. Scheinfein, *J. Opt. Soc. Am. B* **8**, 1974 (1991).
- [46] McClelland, J.J., *J. Opt. Soc. Am. B* **12**, 1761 (1995).
- [47] Haubrich, D., H. Schadwinkel, F. Strauch, B. Ueberholz, R. Wynands, and D. Meschede, *Europhys. Lett* **34**, 663 (1996).
- [48] Frese, D., B. Ueberholz, S. Kuhr, W. Alt, D. Schrader, V. Gomer, and D. Meschede, *Phys. Rev. Lett.* **85**, 3777 (2000).
- [49] Kuhr, S., W. Alt, D. Schrader, M. Müller, V. Gomer, and D. Meschede, *Science* **293**, 278 (2001).
- [50] Alt, W., D. Schrader, S. Kuhr, M. Müller, V. Gomer, and D. Meschede *Phys. Rev. A* **67**, 033403 (2003).

- [51] Kuhr, S., W. Alt, D. Schrader, I. Dotsenko, Y. Miroshnychenko, W. Rosenfeld, M. Khudaverdyan, V. Gomer, A. Rauschenbeutel, and D. Meschede, *Phys. Rev. Lett.* **91**, 213002 (2003).
- [52] Schrader, D., I. Dotsenko, M. Khudaverdyan, Y. Miroshnychenko, A. Rauschenbeutel, and D. Meschede, *Phys. Rev. Lett.* **93**, 150501 (2004).
- [53] Dotsenko, I., W. Alt, M. Khudaverdyan, S. Kuhr, D. Meschede, Y. Miroshnychenko, D. Schrader, and A. Rauschenbeutel, *Phys. Rev. Lett.* **95**, 033002 (2005).
- [54] Khudaverdyan, M., W. Alt, I. Dotsenko, L. Frster, S. Kuhr, D. Meschede, Y. Miroshnychenko, D. Schrader, and A. Rauschenbeutel, *Phys. Rev. A* **71**, 031404 (2005).
- [55] Frese, D., Doctoral thesis, University of Bonn, (2005).
- [56] Grachtrup, C., Diploma thesis, University of Bonn, (2005).
- [57] Corwin, K.L., Z.-T. Lu, C.F. Hand, R.J. Epstein, and C.E. Wieman, *Appl. Opt.* **37**, 3295 (1998).
- [58] Esslinger, T., I. Bloch, and T.W. Hänsch, *Phys. Rev. A* **58**, R2664 (1998).
- [59] Klempt, C., T. van Zoest, T. Henninger, O. Topic, E. Rasel, W. Ertmer, and J. Arlt, *Phys. Rev. A* **73**, 013410 (2006).
- [60] Ringler, M., Diploma thesis, University of Bonn, (2003).
- [61] Telles, G.D., W. Garcia, L.G. Marcassa, V.S. Bagnato, D. Ciampini, M. Fazzi, J.H. Miller, D. Wilkowski, and E. Arimondo, *Phys. Rev. A* **63**, 033406 (2001).
- [62] Holmes, M.E., M. Tschernock, P.A. Quinto-Su, and N.P. Bigelow, *Phys. Rev. A* **69**, 063408 (2004).
- [63] Delannoy, G., S.G. Murdoch, V. Boyer, V. Josse, P. Bouyer, and A. Aspect, *Phys. Rev. A* **63**, 051602 (2001).
- [64] Two species quantum degenerate Bose gas experiment in the group of Simon Cornish, Durham University, <http://massey.dur.ac.uk/research/2spec/2spec.html>.
- [65] DeMarco, B., and D.S. Jin, *Phys. Rev. A* **58**, R4267 (1998).
- [66] Marinescu, M., and H.R. Sadeghpour, *Phys. Rev. A* **59**, 390 (1999).
- [67] Fellows, C.E., R.F. Gutteres, A.P.C. Campos, J. Vergès, and C. Amiot, *Journal of Molecular Spectroscopy* **197**, 19 (1999).

- [68] Schrader, D., Doctoral thesis, University of Bonn, (2004).
- [69] Weidemüller, M., and C. Zimmerman (eds.), *Interactions in Ultracold Gases*, Wiley-VCH, Weinheim (2003).
- [70] Fedichev, P.O., M.W. Reynolds, and G.V. Shlyapnikov, *Phys. Rev. Lett.* **77**, 2921 (1996).
- [71] Burt, E.A., R.W. Ghrist, C.J. Myatt, M.J. Holland, E.A. Cornell, and C.E. Wieman, *Phys. Rev. Lett.* **79**, 337 (1997).
- [72] Stamper-Kurn, D.M., M.R. Andrews, A.P. Chikkatur, S. Inouye, H.-J. Miesner, J. Stenger, and W. Ketterle, *Phys. Rev. Lett.* **80**, 2027 (1998).
- [73] Söding, J., D. Guéry-Odelin, P. Desbiolles, F. Chevy, H. Inamori, and J. Dalibard, *Appl. Phys. B* **69**, 257 (1999).
- [74] Esry, B.D., C.H. Greene, and J.P. Burke, Jr., *Phys. Rev. Lett.* **83**, 1751 (1999).
- [75] Anderlini, M., E. Courtade, M. Cristiani, D. Cossart, D. Ciampini, C. Sias, O. Morsch, and E. Arimondo, *Phys. Rev. A* **71**, 061401 (2005).
- [76] Jamieson, M.J., H. Sarbazi-Azad, H. Ouerdane, G.-H. Jeung, Y.S. Lee, and W.C. Lee, *J. Phys. B* **36**, 1085 (2003).
- [77] Kagan, Y., B.V. Svistunov, and G.V. Shlyapnikov, *JETP Lett.* **42**, 209 (1985).
- [78] D’Incao, J.P., and B.D. Esry, *Phys. Rev. Lett.* **94**, 213201 (2005).
- [79] Smirne, G., R.M. Godun, D. Cassettari, V. Boyer, C.J. Foot, T. Volz, N. Syassen, S. Dürr, G. Rempe, M.D. Lee, K. Góral, and T. Köhler, *cond-mat/0604183* (2006).
- [80] Kraemer, T., M. Mark, P. Waldburger, J.G. Danzl, C. Chin, B. Engeser, A.D. Lange, K. Pilch, A. Jaakkola, H.-C. Nägerl and R. Grimm, *Nature* **440**, 315 (2006).
- [81] Kalas, R.M., and D. Blume, *cond-mat/0512031* (2005).
- [82] Lye, J.E., L. Fallani, M. Modugno, D.S. Wiersma, C. Fort, and M. Inguscio, *Phys. Rev. Lett.* **95**, 070401 (2005).
- [83] Greiner, M., O. Mandel, T.W. Hänsch, and I. Bloch, *Nature* **419**, 51 (2003).
- [84] Leung, V.Y.F., A.G. Truscott, and K.G.H. Baldwin, *Phys. Rev. A* **66**, 061602 (2002).

- [85] Khaykovich, L., F. Schreck, G. Ferrari, T. Bourdel, J. Cubizolles, L. D. Carr, Y. Castin, and C. Salomon, *Science* **296**, 1290 (2002).
- [86] Burger, S., K. Bongs, S. Dettmer, W. Ertmer, K. Sengstock, A. Sanpera1, G. V. Shlyapnikov, and M. Lewenstein, *Phys. Rev. Lett.* **83**, 5198 (1999).
- [87] Denschlag, J., J.E. Simsarian, D.L. Feder, C.W. Clark, L.A. Collins, J. Cubizolles, L. Deng, E.W. Hagley, K. Helmerson, W.P. Reinhardt, S.L. Rolston, B.I. Schneider, W.D. Phillips, *Science* **287**, 97 (2000).
- [88] Dutton, Z., M. Budde, C. Slowe, and L.V. Hau, *Science* **293**, 663 (2001).
- [89] Carr, L.D., C.W. Clark, and W.P. Reinhardt, *Phys. Rev. A* **62**, 063610 and 063611 (2000).
- [90] Pérez-García, V.M., H. Michinel, and H. Herrero, *Phys. Rev. A* **57**, 3837 (1998).
- [91] Michinel, H., V.M. Pérez-García, and R. de la Fuente, *Phys. Rev. A* **60**, 1513 (1999).
- [92] Carr, L.D., M.A. Leung, and W.P. Reinhardt, *J. Phys. B* **33**, 3983 (2000).
- [93] Donley, E.A., N.R. Claussen, S.L. Cornish, J.L. Roberts, E.A. Cornell, and C.E. Wieman, *Nature* **412**, 295 (2001).
- [94] Carr, L.D., Y. Castin, e-print cond-mat/0205624.
- [95] Al Khawaja, U. H.T.C. Stoof, R.G. Hulet, K.E. Strecker, and G.B. Partridge, *Phys. Rev. Lett.* **89**, 200404 (2002).
- [96] Görlitz, A., J.M. Vogels, A.E. Leanhardt, C. Raman, T.L. Gustavson, J.R. Abo-Shaeer, A.P. Chikkatur, S. Gupta, S. Inouye, T. Rosenband, and W. Ketterle, *Phys. Rev. Lett.* **87**, 130402 (2001).
- [97] Ruprecht, P.A., M. J. Holland, K. Burnett, and M. Edwards, *Phys. Rev. A* **51**, 4704(1995).
- [98] Saito, H. and M. Ueda, *Phys. Rev. Lett.* **86**, 1406 (2001).
- [99] Gordon, J.P., *Opt. Lett.* **8**, 596 (1983).
- [100] For a lithium condensate with  $a = -3a_0$  in a cigar-shaped trap with  $v = 70Hz$ , this corresponds to  $N \approx 70000$ , where  $a_0$  is the Bohr radius.
- [101] Edmundson, D.E., and R. H. Enns, *Phys. Rev. A* **51**, 2491 (1995).

- [102] Elyutin, P.V., A.V. Buryak, V.V. Gubernov<sup>1</sup>, R.A. Sammut, and I.N. Towers, *Phys. Rev. E* **64**, 016607 (2001).
- [103] Andrews, M.R., C.G. Townsend, H.-J. Miesner, D.S. Durfee, D.M. Kurn, and W. Ketterle, *Science* **275**, 637 (1997).
- [104] Strecker, K.E., G.B. Partridge, A.G. Truscott, and R.G. Hulet, *New Journal of Phys.* **5**, 73 (2003).
- [105] Carr, L.D., and J. Brand, *Phys. Rev. Lett.* **92**, 040401 (2004).
- [106] Chaustowski, R.R., V.Y.F. Leung, and K.G.H. Baldwin, submitted to *Applied Physics B* (2006).
- [107] DeMille, D., *Phys. Rev. Lett.* **88**, 067901 (2002).
- [108] Esry, B.D., and C.H. Greene, *Nature* **440**, 289 (2006).
- [109] Cornish, S.L., S.T. Thompson and C.E. Wieman, *cond-mat/0601664* (2006).
- [110] Smith, P.W. and T. Hänsch, *Phys. Rev. Lett.* **26**, 740 (1971).
- [111] Wieman, C., and T.W. Hänsch, *Phys. Rev. Lett.* **36**, 1170 (1976).
- [112] Pearman, C.P., C.S. Adams, S.G. Cox, P.F. Griffin, D.A. Smith, and I.G. Hughes, *J. Phys. B* **35**, 5141 (2002).
- [113] Steck, D.A., *Rubidium 87 D Line Data*, <http://steck.us/alkalidata/> (October 2003).
- [114] Steck, D.A., *Cesium D Line Data*, <http://steck.us/alkalidata/> (October 2003).
- [115] van Kempen, E.G.M., S.J.J.M.F. Kokkelmans, D.J. Heinzen, and B.J. Verhaar, *Phys. Rev. Lett.* **88**, 093201 (2002).
- [116] Leo, P.J., C.J. Williams, and P.S. Julienne, *Phys. Rev. Lett.* **85**, 2721 (2000).
- [117] Colombe, Y., E. Knyazchyan, O. Morizot, B. Mercier, V. Lorent, and H. Perrin, *Europhys. Lett.* **67**, 593 (2004).
- [118] Lesanovsky, I., T. Schumm, S. Hofferberth, L.M. Andersson, P. Krüger, and J. Schmiedmayer, *physics/0510076* (2005).
- [119] Courteille, Ph. W., B. Deh, J. Fortágh, A. Günther, S. Kraft, C. Marzok, S. Slama, and C. Zimmerman, *J. Phys. B* **39**, 1055 (2006).



# Acknowledgments

It is my pleasure to gratefully acknowledge the contributions of a large number of people from widely separated locations to my doctoral education.

Many thanks to my chief supervisors in Australia and Germany, Dr. Ken Baldwin and Prof. Dieter Meschede. As a result of their flexibility and open-mindedness, I have benefitted from an unusually high degree of mobility in my graduate schooling and have seen more of the world and worked with a more varied group of people and projects than would have otherwise been possible. In addition I would like to particularly thank Prof. Meschede for his decision to allow me to change tracks and enter his group's BEC experiment in the middle of my PhD. This has afforded me many new research opportunities, for which I remain grateful.

My first working experience with neutral atoms was gained in the Atom Manipulation experiment at the ANU, for which I would like to thank my early supervisor Dr. Maarten Hoogerland, and colleagues Dr. Max Colla, Dr. Robert Dall, Naomi Sih, James Swansson, and Dr. Linda Uhlmann. In my last year in Canberra we were joined by Dr. Andrew Truscott, with whom I worked closely on the numerical simulation of soliton trains – thank you very much for the opportunity to take part in a project which has remained of great interest to me, long after the last round of number-crunching.

For their kind hospitality during my first nine months in Germany, thank you to the members of the Indium experiment, made up at that time of our postdoc Dr. Ulrich Rasbach, and colleagues Dr. Ruby dela Torre and Dr. Jiayu Wang. It was also here that I first encountered the experimental talents of Dr. Dietmar Haubrich, which not only helped us in this lab, but also later at the BEC experiment. This and the extended discussions with (nearly) perennial visitor Prof. Hal Metcalf were both memorable parts of my Indium experience for which I would like to thank all involved.

Thank you to Dr. Arno Rauschenbeutel, our postdoc at the BEC experiment, for his ideas, criticisms, and discussions, which have had a tendency to improve the rigor of my approach every time I talk to him. Many thanks to my BEC colleagues Dr. Daniel Frese and Michael Haas, both of whom have worked long and hard for this experiment, for their advice, help, and discussions, from which I have learnt much. Special thanks also to Daniel for sharing the valuable knowledge he has acquired as an original member of the BEC-team.

A lot of the experimental studies presented in Chapter 2 was based on work I performed with Christian Grachtrup, who joined us for his Diplom, and who worked long hours with me despite serious family difficulties. I would like to thank him for the great effort he took to be there, even though it was not always easy, and for many fruitful discussions. The next genera-

tion BEC Team, Shincy John and Claudia Weber, have been a pleasure to have as colleagues. Thanks and best of luck for the future.

For our work on the microwave system, I would like to acknowledge the technical assistance of Michael Rôzmann. Many thanks to the administrative staff Alice Duncanson, Ilona Jaschke, Fien Latumahina, and Annelise Miglo, who kept it all running so smoothly, day after day, and the members of the mechanical and electronic workshops, both in Australia and Germany, many of whom I regularly relied on for their expertise. I would also like to thank the wider community of group members and other colleagues at AMPL and the IAP, each of which created a distinctive working atmosphere that was a pleasure to be part of.

Sincere thanks to the people who reviewed my thesis, in whole or in part, and whose efforts have in many cases put my thinking back on track: Ken Baldwin, Daniel Frese, Christian Grachtrup, Michael Haas, Dieter Meschede, and Arno Rauschenbeutel.

At this point I would like to thank my father, Dr. Kenneth Leung, for his generous and unfailingly gracious support. And finally, I would like to thank my mother, Annie Chui, for her belief in me, wherever in the world I am, and whatever incomprehensible things I happen to be doing there. There have been numerous times when I found it gratifying to know that this part of my life, thankfully, never changed.